SEARCH FOR THE ISOVECTOR GIANT MONOPOLE RESONANCE VIA THE
^{28}SI(^{10}BE,^{10}B+γ) REACTION AT 100 MEV/U

By

Michael J. Scott

A DISSERTATION

Submitted to
Michigan State University
in partial fulfillment of the requirements
for the degree of

Physics - Doctor of Philosophy

2015

ABSTRACT

SEARCH FOR THE ISOVECTOR GIANT MONOPOLE RESONANCE VIA THE ^{28}SI(^{10}BE,^{10}B+γ) REACTION AT 100 MEV/U

By

Michael J. Scott

The isovector giant monopole resonance (IVGMR) is a fundamental mode of collective oscillation in which the neutron and proton fluids in a nucleus radially expand and contract in an out-of-phase manner. Observation of the IVGMR has been difficult. The non-spin-transfer IVGMR resonance is obscured by its spin-transfer counterpart, the isovector spin giant monopole resonance (IVSGMR). The problem is the lack of a suitable probe for measurement of non-spin-transfer, isovector events. By way of the (^{10}Be,^{10}B+γ) charge-exchange reaction, selectivity for the excitation of the IVGMR can be gained. Isolation of $\Delta S = 0$, $\Delta T = 1$ reactions is achieved through excitation of the superallowed Fermi transition ^{10}Be(0^+,g.s.)$\rightarrow^{10}$B(0_1^+, 1.74 MeV,$\Delta T = 1$), which is detected by observation of the 1022 keV gamma ray from the deexctation of the isobaric analogue state in ^{10}B to the ^{10}B(1_1^+, 0.718 MeV) state. The applicability of this probe in separation of $\Delta S = 0$, $\Delta T = 1$ reactions is observed with data taken on a ^{12}C target through selectivity in observation of the ^{12}C(0^+,g.s.)$\rightarrow^{12}$B(1^+,g.s.) transition, which is $\Delta S = 1$ by definition. IVGMR strength in ^{28}Al is identified using the the ^{28}Si(^{10}Be,^{10}B+γ) reaction at E(^{10}Be)=1000 MeV. Isovector monopole strength is observed up to E$_x$(^{28}Al)=30 MeV. The observed non-energy weighted sum rule strength for peaks at 9 and 21 MeV is determined to be $66 \pm 36\%$ and $59 \pm 32\%$, respectively. Exctracted IVGMR and isovector giant dipole resonance distributions are also compared with results from calculations in the charge-exchange relativistic time blocking approximation.

To Lulu - Reaching your dream begins with a single step. The path may be long, but your diligence will serve you.

ACKNOWLEDGMENTS

I would like to begin by thanking Remco Zegers for all of his help in my graduate studdies at Michigan State University. Without your guidance, I could not have come this far. Thank you for answering all of my questions... more than once.

I would like to personally thank the members of the committe for their guidance through my academic career at Michigan State University: Alex Brown, Ed Brown, Sean Liddick, and Artemis Syprou.

I would like to thank the staff and operators of the National Superconducting Cyclotron laboratory for their expertise in running the lab. With their assistance we were able to run a successful experiment.

I have enjoyed the company of my fellow graduate students and freinds in the lab. Sometimes one needs a good laugh to take their mind off of a difficult problem.

To my daughter Lulu. Thank you for being an inspiration. I wanted to go to school to better myself, so in turn I could be better for you. Daddy loves you.

To my wife Kristie. I appreciate all that you do for our family, and the support that you give me. Without you I know I could not put in the hours that are necessary to complete my tasks. In fact, as I am writing this, it is after midnight and I can hear you grinding my coffee for me for the morning. Yes, I know it is late... Yes, I know I need to get up in the morning... Okay, I'll go to bed now. I love you dearly.

TABLE OF CONTENTS

LIST OF TABLES

LIST OF FIGURES

Chapter 1

Introduction

In nuclear charge exchange reactions, a probe inelastically scatters from a target nucleus while exchanging a neutron for a proton, or vice-versa, leaving the residual target nucleus in an excited state. The interaction of the probe with the target can cause resonant oscillations that involve a large fraction of the nucleons, referred to as giant resonances. The strength of a giant resonance depends on the size of the system and the number of particles able to participate, and is limited by a sum rule. For a resonance to be considered a giant resonance (GR), the observed strength of resonance should exhaust about 50% or more of the associated sum rule.

First evidence of GRs was obtained by Bothe and Gentner [2] in the 1930's through observation of strong resonant structure in nuclei via photoabsorption of 17 MeV photons produced by bombarding protons onto a ^{7}Li target. In 1944, Migdal gave the first theoretical description of the electric dipole resonances [3]. In the subsequent years, theoretical descriptions of GRs progressed (see Section 3) and systematic studies of the isovector giant dipole resonance (IVGDR) were underway ([4] and references therein). About 30 years after the first observation of the IVGDR, observation of the isoscalar giant quadrupole resonance (ISGQR) [5, 6] was realized, showing GRs were not solely isovector in nature. Since then, effort has been put forth to identify many other GR modes. A detailed history can be found in Reference [1].

Intuitively, GRs can be described as shape oscillations of the nuclear fluid in a hydrody-
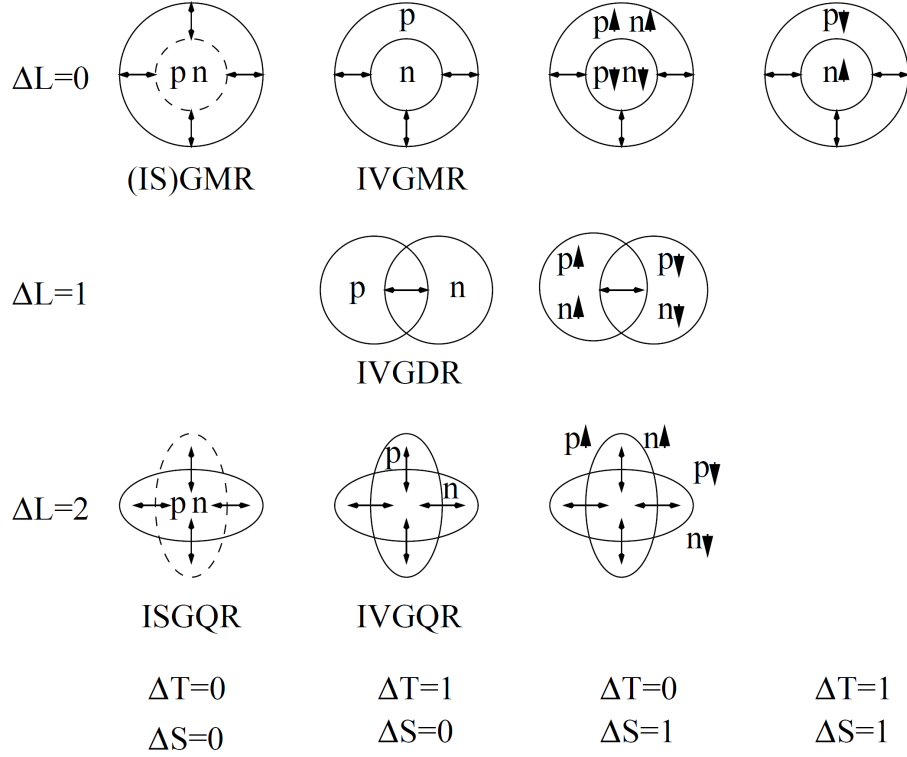
Figure 1.1 Schematic representation of various collective modes. Multipoles shown correspond to $\Delta L = 0$ (monopole), $\Delta L = 1$ (dipole), and $\Delta L = 2$ (quadrupole). Figure taken from [1].

namical model, as depicted in Figure 1.1. In this picture, the multipolarity of the excitation (described by the number of units of angular momentum transferred; ΔL) gives rise to the shape/density deformation of the nucleus. The simplest mode of excitation, the isoscalar giant monopole resonance (ISGMR), is described by radial oscillations of the nucleus with proton and neutron densities oscillating in phase, referred to as a breathing mode. The spin degrees of freedom may also be excited by a unit transfer of spin angular momentum ($\Delta S = 1$). Similar to the ISGMR, the isoscalar spin giant monopole resonance (ISSGMR) oscillated in a radial, breathing mode, but the transfer of spin causes the spin up(down) protons and neutrons to oscillate out-of-phase with the spin down(up) protons and neutrons. Lastly, isospin degrees of freedom can be excited through a unit transfer of isospin

($\Delta T = 1$), where an excitation of this nature is referred to as isovector (IV). The simplest isovector mode is the isovector giant monopole resonance (IVGMR), where again the nucleus is described by radial, "breathing" oscillations, but the proton and neutron densities oscillate out-of-phase. By combining different unit transfers of orbital angular momentum (L), spin (S), and isospin (T), the more complex GRs depicted in Figure 1.1 are described. A more detailed overview of GRs can be found in Chapter 3.

The goal of this study is to measure the IVGMR. Similar to the ISGMR, the IVGMR is a breathing mode, but proton and neutron densities oscillate out-of-phase. It can provide valuable information on nuclear structure and Coulomb effects relating to, for example, isospin-symmetry breaking from the Coulomb force [7]. Detailed information about the IVGMR similar to what is known for the ISGMR [8, 9], will add to our understanding of the nuclear equation of state and other macroscopic properties of nuclei and nuclear matter, such as the incompressibility.

The IVGMR has been difficult to study in detail in experiments. Principally, the issue has been that the various GR modes appear either directly on top of each other in excitation energy, or near enough to each other to obscure the resonance of interest. The solution is to find a suitable method to selectively probe for IVGMR strength.

To dissentangle each GR from others, each unit of quantum number transfer (T, L, S) needs to be determined. To separate isoscalar GRs from isovector GRs, CE reactions serve a useful role, where the probing reaction is of the nature ($\pi^{\pm}, \pi^0$) or (A(N,Z),A(N$\pm$1,Z$\mp$1)). The multipolarity of the reaction can be separated by the shape of the angular distribution (differential cross-section versus scattering angle) in what is called a multipole decomposition analysis. Lastly, isolation of non-spin-flip excitations from spin-flip has often utilized structural effects of the reaction mechanism to determine the spin nature of the resonance,

and for isovector GR reactions, a suitable probe system has been difficult to identify.

The most convincing results for the IVGMR has come from π-charge-exchange reactions [10, 11]. This method utilized the spinless nature of the π-mesons such that spin-flip transitions were not excited. Though a portion of the spectra identified in these reactions was attributed to the IVGMR, due to the treatment of the large non-resonant background, upon which the relatively small IVGMR sits, the results are somewhat tenuous (see Section 2.1).

To unambiguously identify the IVGMR in this study, we have used the $(^{10}\text{Be},^{10}\text{B}+\gamma(1.022$ MeV)) probe system. The novelty of this probe lies in the superallowed Fermi ($\Delta S = 0$) transition $^{10}\text{Be}(0^+,\text{g.s.}) \rightarrow ^{10}\text{B}(0^+,1.74 \text{ MeV})$ which does not suffer from a large amount of feeding from higher energy excitations in ^{10}B. By measuring the emmitted 1.022 MeV gamma-ray from the de-excitation of the 1.74 MeV state in coincident with the ^{10}B ejectile, isovector-non-spin-flip excitations can cleanly be isolated (see Sections 2.1 and 4.3.1). From the data obtained in the coincidence measurement, a multipole decomposition analysis can be performed to isolate a $\Delta T = 1$, $\Delta S = 0$, $\Delta L = 0$ spectrum for the observation of the IVGMR.

Chapter 2

Experimental Considerations for the Isovector Non-Spin-Flip Monopole Resonance

In this chapter, the technical details of the identification of the IVGMR in ^{28}Al via the ^{28}Si(^{10}Be,^{10}B+γ(1.022 MeV)) reactions are discussed. Of the many GR modes, this study is focused on developing a tool for measuring the IVGMR. The IVGMR is an excitation over two major oscillator shells (labeled $2\hbar\omega$, where $\hbar\omega$ describes the energy of the excitation) associated with the operator charge exchange (CE) $r^2\tau$ (where τ medaites the CE excitation) and is mediated by neutron-particle, proton-hole excitations (for $\Delta T_Z = +1$ CE reactions) over two major oscillator shells [12], as illustrated in Figure 2.1. It resides in the continuum region of the nucleus and has a large width ($\Gamma \sim 10$ MeV). Since the IVGMR is an out-of-phase oscillation of proton and neutron densities, a deeper understanding of the isovector nature of effective nuclear forces can be obtained for spherical nuclei [13]. However, there is a dearth of experimental data on the IVGMR, despite its potentially close relation to asymmetric nuclear matter and isospin mixing in nuclei.

The use of heavy ions in charge exchange reactions has allowed many studies of the isovector response in nuclei. With advances in rare isotope beams at intermediate energies,
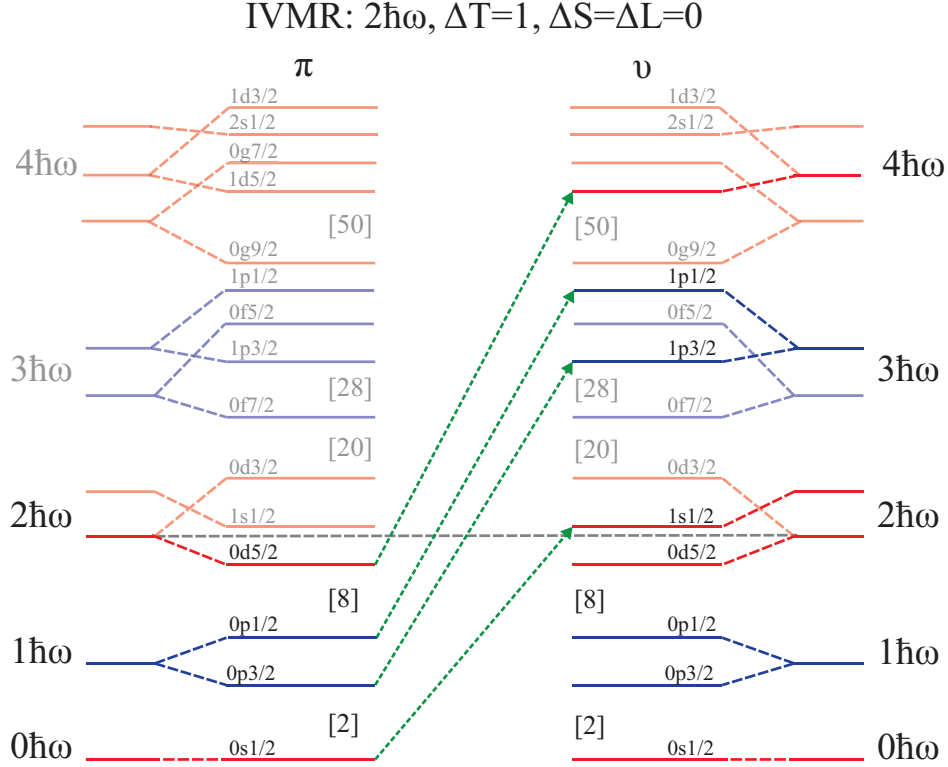
Figure 2.1 Illustrations of particle-hole contributions to the IVGMR in the ^{28}Si$\to$ ^{28}Al system. The horizontal gray dashed line represents the Fermi level, up to which the particles fill the ground state. The IVGMR is a coherent superposition of the excitations highlighted with green arrows.

a large array of probes are available of different spin and isospin, allowing increased selectivity in reaction channel. In this study, we propose to use the $(^{10}$Be,^{10}B$+\gamma)$ heavy-ion charge exchange probe to isolate $(\Delta S = 0, \Delta T = 1)$ reactions for observation of the IVGMR.

2.1 Probing for the IVGMR

Multiple attempts have been made to measure the IVGMR, with an array of probes. A first experiment aimed at identifying isovector resonances was performed on a series of targets using pion CE probes [10]. The $(\pi^{\pm}, \pi^{0})$ reaction is a good candidate probe for IVGMR studies because of its selectivity of $(\Delta S = 0, \Delta T = 1)$ transitions. Since the π^{0} decays to
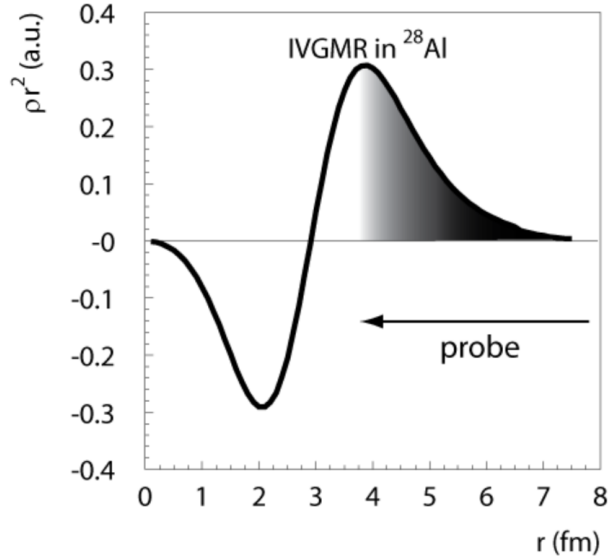
Figure 2.2 Transition density multiplied by r^2 for excitation of the IVGMR in ^{28}Al from ^{28}Si. Probing the IVGMR is preferably done using a probe that is strongly absorbed at the surface (as schematically indicated by the shaded area), to avoid the cancellation of the transition strengths due to the exterior and interior components of the transition density.

two gamma-rays, the measurement of the reaction is a coincidence observation between the two gammas of $\approx$100 MeV. Spectra taken on ^{40}Ca is shown in Figure 2.3. The spectra are decomposed into the IVGMR, IVGDR, and a semi-phenomenological background by fitting Gaussians as the peaks and a convolution of a Lorentzian and Exponential decay as the background. However, the coincident measurement of the gamma-rays led to large experimental uncertainties. Also, a weak structure identified as the IVGMR appeared on top of a large background, making interpretation of the result tenuous.

Further studies were performed using nuclear CE probes, such as $(^{13}$C,^{13}N) [14, 15] and $(^{7}$Li,^{7}Be+γ) [16]. The most promising results for the IVGMR using nuclear probes have come from heavy-ion charge exchange probes, rather than light probes such as the (p,n) probe. This is because the light probe will penetrate the nuclear volume rather than strongly absorb at the nuclear surface. As the volume of the nucleus is probed, cancellation of the strength will occur due to a node in the transition density of the reaction near the
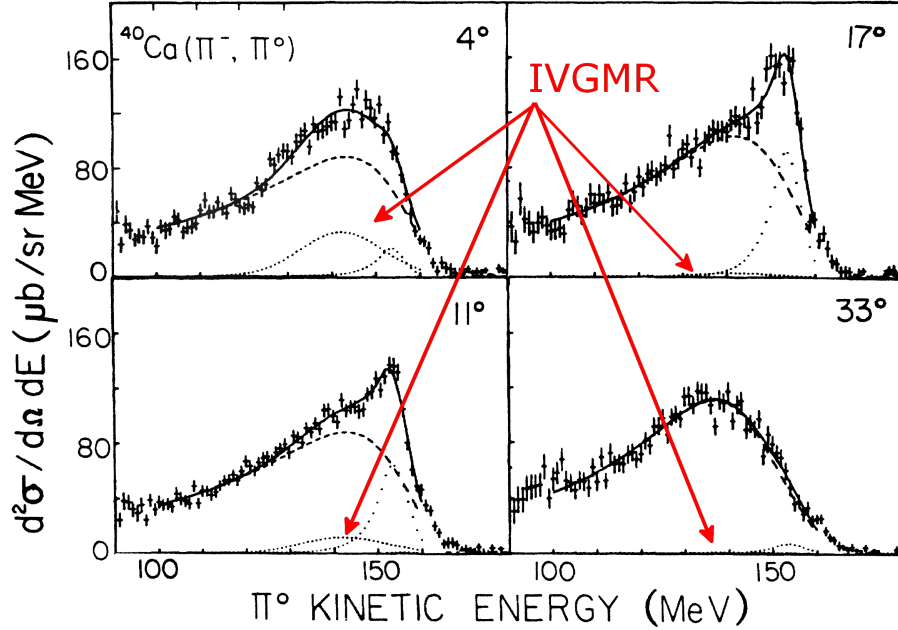
Figure 2.3 Previous experiment for ^{40}Ca using the pion charge exchange reaction [10]. The peak representing the IVGMR is indicated. To the right of the IVGMR is a peak representing the IVGDR. The IVGMR is covered by the background component, drawn with dashed lines. The three curves were fit to the data for extraction of the IVGMR.

nuclear surface, stemming from mass conservation and spherical symmetry of motion [17]. In the case of the $(^{13}C,^{13}N)$ probe, a resonance was observed in agreement with the (π^-,π^0) data on the IVGMR, but no multipole assignment could be made from the observed shape and strength. The $(^7Li,^7Be+\gamma)$ probe was used since coincidence measurements of the ^7Be ejectile with an emitted gamma from the ejectile could be used to isolate transitions in the target system, allowing subtraction of the isovector spin giant monopole resonance (IVSGMR: $\Delta L = 0, \Delta S = 1, \Delta T = 1$) from the IVGMR. Unfortunately, large uncertainties in the $\Delta S = 1$ subtraction and multistep contributions at low beam energy did not allow for an assignment of multipolarity to the measured spectrum.

To reliably extract experimental information about the IVGMR, three conditions must be met:

1) The probe must provide a clean $\Delta S = 0$, $\Delta T = 1$ filter. This is critical for ensuring that the IVGMR ($\Delta L = 0, \Delta S = 0, \Delta T = 1$, mediated by the operator $r^2\tau$) signal is not contaminated by the excitation of its spin-flip partner, the $2\hbar\omega$ IVSGMR ($\Delta L = 0, \Delta S = 1, \Delta T = 1$, mediated by the operator $r^2\sigma\tau$) or the $0\hbar\omega$ Gamow-Teller (GT) ($\Delta L = 0, \Delta S = 1, \Delta T = 1$, mediated by the operator $\sigma\tau$) excitation, and which otherwise cannot be separated from the IVGMR.

2) A clean single-step CE mechanism must be ensured to allow for the accurate theoretical description of the differential cross-sections, necessary for identification of the multipolarity of spectrum strength. To ensure single-step CE reactions are safely dominant, Reference [18] shows that this is true for incident energies of $\sim$100 MeV/u and above. Below that, multistep processes (sequential nucleon-pickup, nucleon-stripping, or vice-versa) can contribute, complicating the interpretation of the data.

3) The probe must be strongly absorbed at the nuclear surface. Due to the operator mediating the excitation of the IVGMR ($r^2\tau$), there is a node in the transition density near the nuclear surface (see Figure 2.2). Probes penetrating the interior of the target nucleus include cancellation of the transition strength. Thus a surface absorbed probe is ideal [19].

The (^{10}C,^{10}B+γ) probe was recently implemented to satisfy these conditions to measure the IVGMR [20]. The heavy-ion charge exchange probe was impinged upon a reaction target with a beam energy of 200 MeV/u, satisfying conditions 2) ans 3). A super-allowed Fermi transition in the probe system [^{10}C(0^+,g.s.)$\rightarrow$^{10}B($0^+{}_1$,1.740 MeV), mediated by the operator τ], decays completely by gamma emission of a 1022 keV gamma-ray, and serves as a coincident tag between the emitted gamma and the ^{10}B ejectile for $\Delta S = 0$, $\Delta T = 1$
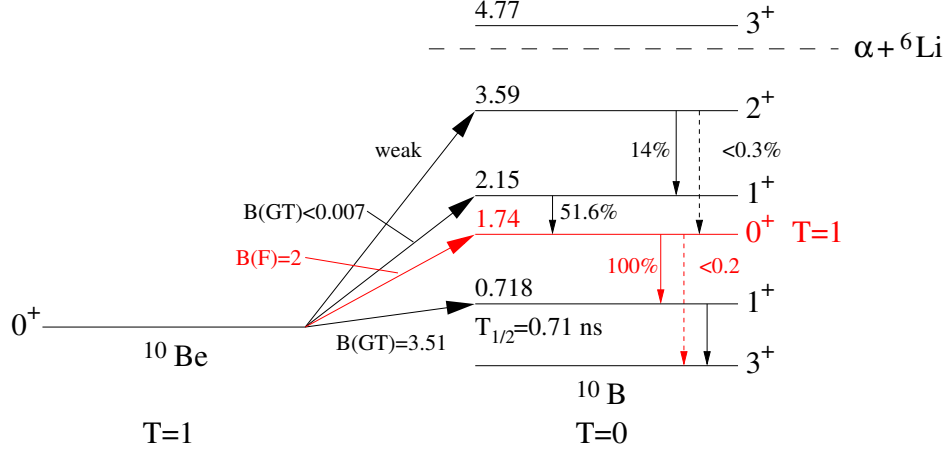
Figure 2.4 The level scheme of ^{10}B of relevance for the (^{10}Be,^{10}B+γ) reaction to isolate $\Delta S = 0$ transitions. The ^{10}Be($0^+, T = 1, g.s.$) $\rightarrow$^{10}B($0^+, T = 1, 1.74$ MeV) transition is accompanied by a 1.022 MeV gamma-ray from deexcitation to the 0.718 MeV 1^+ state.

reaction to satisfy condition 1). With data taken on a ^{90}Zr and ^{7}Li target, spectra were obtained for isovector, non-spin-transfer reactions, which were decomposed by multipolarity. However, measurement of the IVGMR was not achieved in this study due to low statistics and low gamma-ray energy resolution of the data set.

2.2 The (^{10}Be,^{10}B+γ) Probe for Isovector Non-Spin-Flip Excitations

Given the shown efficacy of the (^{10}C,^{10}B+γ) probe [20], the (^{10}Be,^{10}B+γ) probe was used in this study. The (^{10}Be,^{10}B+γ) probe works much like its counterpart, the (^{10}C,^{10}B+γ) probe, but in the $\Delta T_z = 1$ direction. Since isolation of the IVGMR requires a $\Delta S = 0$, $\Delta T = 1$ probe, CE reactions connecting isobaric analogue states (IAS) via a super allowed Fermi transition in the projectile, with negligible feeding from higher lying spin-transfer reactions, are ideal.

Of the light nuclei which are potential probes, the CE reaction to the ^{10}B(IAS) is ideal.
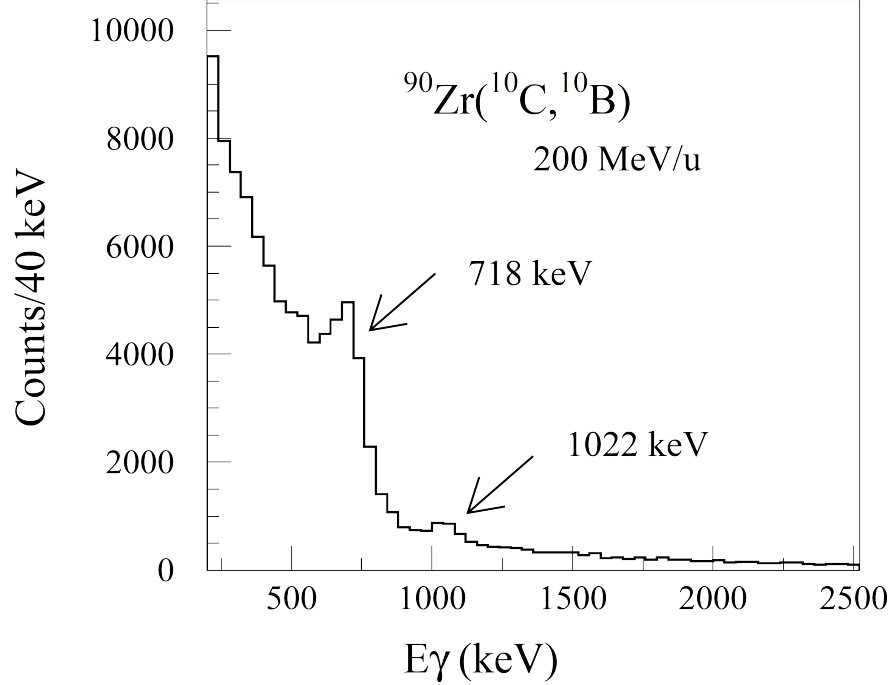
Figure 2.5 Gamma-ray spectrum with Doppler correction in the ^{90}Zr(^{10}C,^{10}B) reaction [20].

This is because reactions to the ^{10}B(IAS) have small to negligible contributions from highly excited GT states that could contaminate the non-spin-flip signal, as opposed to other reactions considered, such as (^{14}O,^{14}N(IAS)) and (^{18}N,^{18}F(IAS) [20]. Figure 2.4 shows the (^{10}Be,^{10}B) probe system, with the IAS transition to the 1.74 MeV level in ^{10}B highlighted in red. At the experimental beam energy (100 MeV/u), isovector spin-transfer reactions are more strongly excited than isovector non-spin-transfer reactions ([21], see Section 4.3.1). The first excited state in ^{10}B is the 0.718 MeV 1$^+$ level with a strong GT transition strength of $B(GT) = 3.51$ [22].

For the probe to provide a clean $\Delta S = 0$, $\Delta T = 1$ signal, feeding from higher-lying states must be minimal. Below the α decay threshold of 4.66 MeV in ^{10}B, two states exist above the 1.74 MeV state. The state 414 keV above the 1.74 MeV state can be populated by GT transitions from the ground state of ^{10}Be. However, the transition strength is known to be

11

Intensity of ^{10}Be beam	3.9×10^6	
Target Thickness	35.35 mg/cm^2 (92% ^{28}Si)	
γ-ray Efficiency (1.022 MeV)	9.1%	
Cross-Section	5 μb ($\theta_{c.o.m.} < 1°$)	10 μb ($\theta_{c.o.m.} < 5°$)
Event Rate per day for IVGMR	160 day^{-1}	280 day^{-1}

Table 2.1 Event rates and inputs to calculation. Calculations were performed for cross-sections up to 1° and 5° scattering angle in the center-of-mass. See text for calculation.

small ($B(GT) < 0.007$ [23]) and does not completely decay to the 1.74 MeV state. The 3.59 MeV state is weakly populated, and decays to the 1.74 MeV state with a branching of $< 0.03\%$. As such, contamination of the isovector non-spin-transfer signal is expected to be small. Figure 2.5 shows the Doppler-corrected spectrum measured in Reference [20] for the $(^{10}\text{C},^{10}\text{B}+\gamma)$ probe, and does not show signs of contamination.

To experimentally isolate $\Delta S = 0$, $\Delta T = 1$ reactions using the $(^{10}\text{Be},^{10}\text{B}+\gamma)$ reaction, the ^{10}Be projectile reacts with a target nucleus, leaving the reacted projectile (ejectile) ^{10}B* in an excited state, which upon decay by gamma emission serves as a tag for the reaction. The gamma energy of interest is 1022 keV, which comes from ^{10}B being populated in the 1.74 MeV state and decaying to the 0.718 MeV state. The coincidence observation of the 1022 MeV gamma with ^{10}B serves as the isovector non-spin-transfer tag. This measurement then indicates a $0^+ \rightarrow 0^+$ isovector non-spin-transfer reaction occurring in the target nucleus.

2.3 Target Selection and Considerations

2.3.1 ^{28}Si

For this experiment, we chose ^{28}Si as the reaction target. This is a relatively light nucleus for GR studies, but the reported attainable beam intensity for ^{10}Be required using a lighter

	Estimated contributions to excitation energy resolution (FWHM) in ^{28}Al (MeV)
Reconstructed Energy of ^{10}B particles	1.0
Energy Loss Difference Through Target	2.0
Recoil Due to γ-emission form ^{10}B	1.0
Overall	2.5

Table 2.2 Estimated excitation-energy resolution in ^{28}Al via the ^{28}Si(^{10}Be,^{10}B $+\gamma$(1022 MeV)) reaction. The reconstructed energy of the ^{10}B particles in the S800 spectrograph at NSCL [24, 25] includes a conservative estimate for the quality of dispersion matching. The contribution to the resolution due to recoil of ^{28}Al by decay-in-flight by gamma emission includes contributions from both the 1.022 MeV $(0^+{\rightarrow}1^+)$ and subsequent 0.718 MeV $(1^+{\rightarrow}3^+)$ transitions as indicated in Figure 2.4. The contribution from the energy loss difference through the target accounts for the fact that the energy losses of ^{10}Be and ^{10}B particles in the target differ and the reaction point in the target is unknown.

nucleus to achieve a suitable count rate.

Table 2.1 shows the expected count rate for the ^{28}Si target with the estimates used on beam intensity, gamma-efficiency, and cross-section for target selection. The beam intensity is the reported value form the Nation Superconducting Cyclotron Laboratory (NSCL) beam isotope list [26]. The beam rate on target was estimated as

$$I = 2.86 \times 10^4 \text{ pps/pnA from LISE++ [27]}$$

$$\times 3 \text{ (empirical scaling factor)}$$

$$\times 0.3 \text{ (estimated transmission to S800)}$$

$$\times 150 \text{ pnA (NSCL beam list) [26]}$$

$$= 3.9 \times 10^6 \text{ pps.} \tag{2.1}$$

The 35.35 mg/cm^2 ^{nat}Si (92.2% ^{28}Si) target was chosen for attaining acceptable count rates.

The gamma-ray efficiency was estimated for all 7 GRETINA detectors placed at 90° around

the target using the simulation from Reference [28]. The estimated cross-section was obtained

based on distorted wave Born approximation calculations (see Chapter 4). The event rate

per day was calculated as

$$Y = N(^{28}\text{Si}) \times BI(^{10}\text{Be}) \times \epsilon \times \sigma \qquad (2.2)$$

where $N(^{28}Si) = $ (target thickness, mg/cm^2) $\times$ (N_A, Avagadro's number)/$\rho(^{28}\text{Si})$, $\rho(^{28}\text{Si})$

is the density of ^{28}Si, $BI(^{10}\text{Be})$ is the beam intensity of ^{10}Be, ϵ is the gamma-detection

efficiency, and σ is the cross-section. The estimated yield is calculated up to $1°$ for the

forward peaking IVGMR, and up to the S800's acceptance limit of about $5°$.

Tables 2.1 and 2.2 show the choice of ^{28}Si is based upon obtaining a strong yield for the

IVGMR, given restrictions on beam intensity and target thickness. Since the beam intensity

cannot be significantly raised, we looked to the relatively light ^{28}Si nucleus for an optimal

cross-section. When addressing the thickness of the target, there are two competing factors:

yield and excitation energy resolution. A thicker target will increase yield, with a loss in

energy resolution, and vice versa. As shown in Figure 2.1, ^{28}Si is the heaviest stable nucleus

in which all proton orbits can participate in the IVGMR. Also, since the $0\hbar\omega$ IAS cannot be

excited, all $\Delta L = 0$, $\Delta S = 0$, $\Delta T = 1$ strength can be assigned to the $2\hbar\omega$ IVGMR.

2.3.2 ^{12}C

In this experiment, a ^{12}C target was also chosen as an excellent test case for the suitability of

the probe, due to the strong GT($\Delta L = 0$, $\Delta S = 1$, $\Delta T = 1$) transition ^{12}C(0^+,g.s.)$\rightarrow$^{12}B(0^+,g.s.).

Figure 2.7 is the measured spectrum of the ^{12}C(t,^{3}He)^{12}B charge-exchange reaction from

Reference [29], showing the peak of the ^{12}B ground state transition of interest. As can be
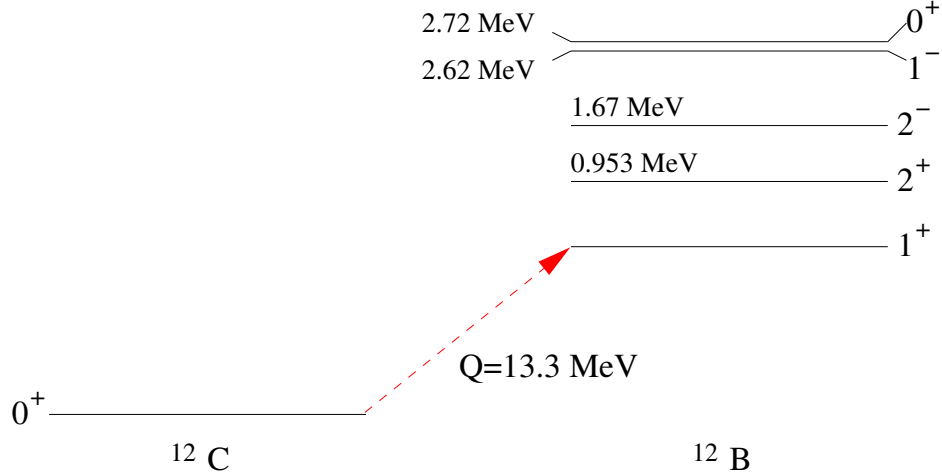
Figure 2.6 The level scheme of the ^{12}B of relevence to the $(^{10}$Be,^{10}B+γ) reaction. Highlighed by the red, dashed arrow is the ^{12}C(0^+,g.s.)$\rightarrow^{12}$B(1^+,g.s.) transition. States in ^{10}B up to 2.72 MeV are also listed.

seen in Figure 2.6 and 2.7, the transition of interest at 0 MeV is separated from the first excited state by 0.953 MeV, so it will appear relatively well separated from the excited states in ^{12}B other than some contamination from the $2^+{}_1$ state in ^{12}B, assuming the resolution estimated in Table 2.2.

The strongly excited ground state to ground state transition in ^{12}C$\rightarrow^{12}$B is $\Delta J^{\pi} = 1^+$, so by the rules of angular momentum transfer, contributing reactions will be $\Delta S = 1$, $\Delta L = 0$ and $\Delta S = 1$, $\Delta L = 2$ in nature. This means that a measurement of the ^{12}C(^{10}Be,^{10}B+γ)^{12}B reaction can show the efficacy of the probe by selectively isolating $\Delta S = 0$ or $\Delta S = 1$ reactions, and would be indicated by this strong ground state peak not being present.
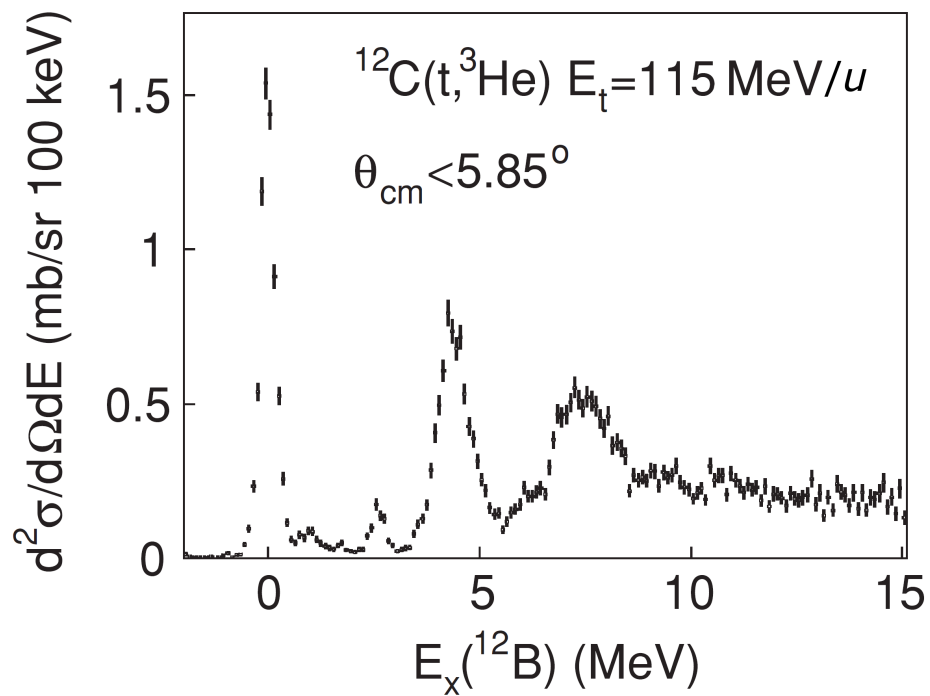
Figure 2.7 Excitation energy spectrum for the ^{12}C(t,^{3}He reaction at 115 MeV/u. Of interest for this study is the strong peak at 0 MeV in the ^{12}B spectrum from the ^{12}C(0^+,g.s.)(t,^{3}He)^{12}B(1^+,g.s.). Graphic adapted from [29]

Chapter 3

Theoretical Description of Giant Resonances

To adequately relate the measured IVGMR to useful structural information, robust theoretical models are necessary. Calculations proceed in either macroscopic or microscopic frameworks to describe giant resonances. In Section 3.1, a brief description of the macroscopic picture is given to highlight this illustrative picture of the GR phenomena. In Section 3.2, a short overview of the ingredients of the microscopic calculations are given to illustrate more clearly the strength limiting sum rule and the origin of the width of the resonance.

3.1   Macroscopic Picture

In the macroscopic picture, the nucleus is portrayed as a liquid drop of proton and neutron fluids where a GR is described as a small-amplitude collective oscillation about the nuclear equilibrium as illustrated in Figure 1.1. The macroscopic description of GRs provides an intuitive picture of GRs to relate to bulk properties of the nucleus. The shape vibrations are of small amplitude, and can be surface-vibrations, compressional vibrations, or a superposition of both modes. In the surface-vibrations, harmonic vibrations about a mean spherical shape are assumed. For the compressional vibrations, it is easiest to picture the surface nucleons as having a fixed position and the harmonic vibration is in the nuclear density. Full
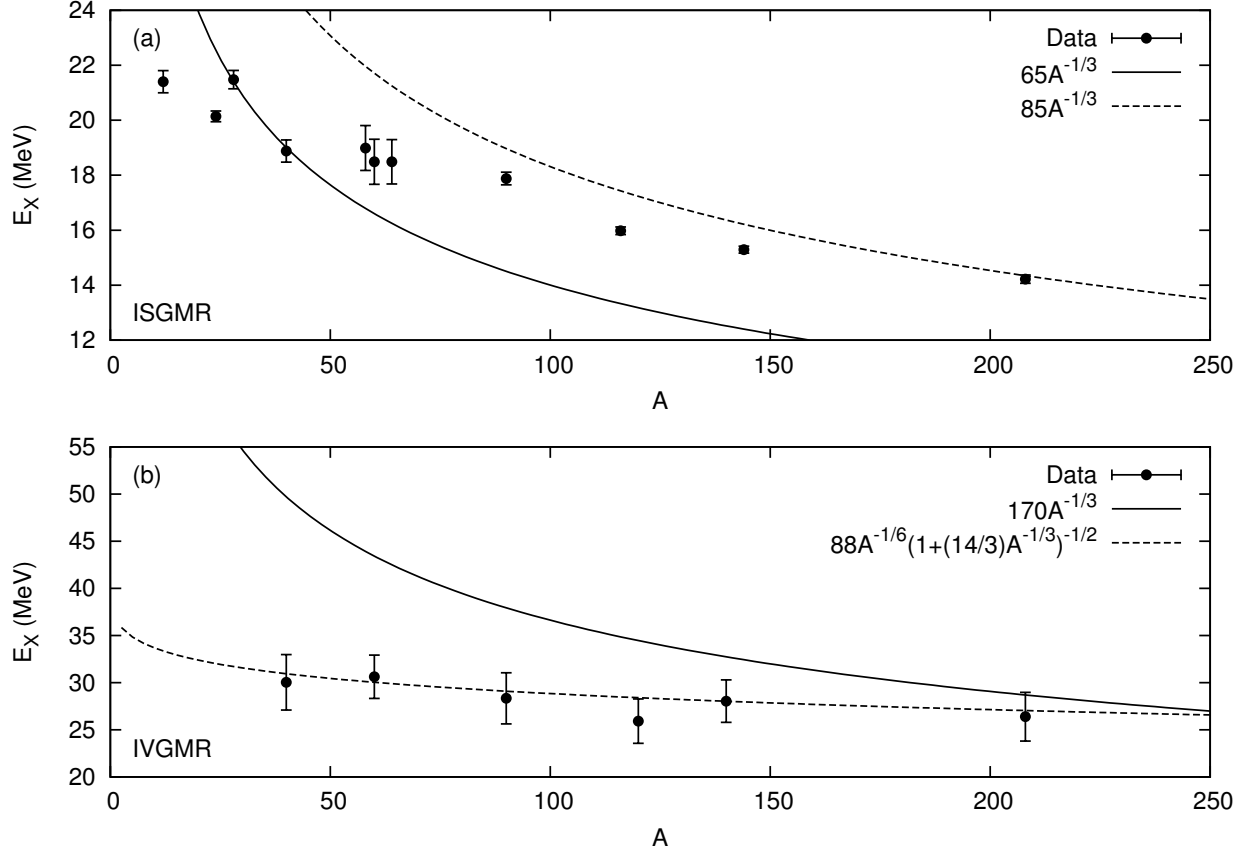
Figure 3.1 (a) Data obtained for the ISGMR via inelastic scattering of α particles at small angles from Reference [32]. The solid line represents the location of the ISGMR as a function of mass (A) from Reference [30], and the dashed line represents an improvement from to the estimate with better knowledge of the nuclear incomressibility term from References [8, 9]. (b) Data obtained for the IVGMR from pion scattering from References [10, 11]. The solid line represents an initial estimate from the hydrodynamical model, and the dashed line represents the improvements to the model when including surface effects [33].

theoretical descriptions of surface-vibrations and compressional vibrations for GRs can be found in References [30] and [31], respectively.

The simplest vibrational GR mode is the isoscalar giant monopole resonance (ISGMR) and has been well studied since 1977, yielding insights into bulk properties of the nucleus such as the incomressibility of nuclear matter (K_{NM}) since $K_{NM} \propto E_X^2(\text{IVGMR})$ [8, 9]. A first estimation of the location in excitation energy of the ISGMR was performed by Bohr and Mottelson for compressional modes of nuclei for small oscillations in density of the

18

nucleus around an equilibrium [30]. They determined the energy of an isoscalar resonance as a function of nuclear mass (A) to be

$$E_{nL} = \frac{\hbar k_{nL}}{1.2} \sqrt{\frac{K_{NM}}{9m}} A^{-1/3} \text{ MeV} \tag{3.1}$$

where k_{nL} are the eigenvalues of the motion for principle quantum number n and multipolarity L, K_{NM} is the incomressibility of nuclear matter, and m is the nucleon mass. At the time of derivation, K_{NM} was not known, and was estimated to be $K_{NM} = 135$ MeV [17]. This gave the solution for the ISGMR ($n = 1$, $L = 0$) to be

$$E_X^{ISGMR} = 65A^{-1/3} \text{ MeV}. \tag{3.2}$$

As experimental information became available, it was determined that $K_{NM} = 231 \pm 5$ MeV [8, 9]. This moves the predicted position of the ISGMR from Equation 3.2 to be defined as

$$E_X^{ISGMR} = 85A^{-1/3} \text{ MeV}. \tag{3.3}$$

Figure 3.1(a) compares data obtained for the ISGMR for a range of nuclear masses to the expected positions of the ISGMR predicted by Equations 3.2 and 3.3. By using the correct value for K_{NM}, Equation 3.3 is able to predict the position of ^{208}Pb, but misses every point below, missing the trend in the lowest masses. To describe even this simplest mode, one needs to include more than just compressional vibrations.

The hydrodynamical model that has been applied to the isovector counterpart of the ISGMR, the IVGMR, approaches nuclei as droplets of viscous compressible fluids with degrees of freedom for protons (Z), neutrons (N), spin-up, and spin-down. As in the ISGMR, these

components are allowed to oscillate at small amplitude around an equilibrium density, as shown in Figure 1.1. The solution, as discussed in References [31] and [34] and references therein, come from linearized Navier-Stokes equations. Solving for the IVGMR,

$$E_X^{IVGMR} = 170A^{-1/3} \text{ MeV.} \tag{3.4}$$

Figure 3.1(b) draws Equation 3.4 as the solid line along with data taken for the IVGMR from pion charge exchange experiments [10, 11]. As with the compressional mode calculation for the ISGMR, the model does not reproduce the shape of the resonance position as a function of nuclear mass. Further work by Bowman et al. [33] showed that not only are volume oscillations needed to describe GRs, but surface effects must be taken into account as well. The excitation energy of the IVGMR was found approximated to be

$$E_X^{IVGMR} = 88A^{-1/6} \left(1 + \frac{14}{3}A^{-1/3}\right)^{-1/2} \text{ MeV.} \tag{3.5}$$

In Figure 3.1(b), Equation 3.5 is drawn. By including into the model surface oscillations along with compressional modes, Equation 3.5 is found to represent the data.

3.2 Microscopic Picture

In the microscopic picture, a nuclear resonance is described as a coherent superposition of one-particle, one-hole (1p-1h) excitations and is limited in strength by the one-body operator's sum rule. A giant resonance typically exhausts most of the one-body operator's sum rule and begin appearing at least several MeV above the ground state. The details of the microscopic calculations have been summarized well in [1, 30, 35, 36, 17, 37].

The response of a nucleus to an arbitrary one-body operator (O) defines the associated strength function, and is built by connecting the ground state of a nucleus to the excited states as

$$S_O(E) = \sum_f |\langle \phi_f | O | \phi_0 \rangle|^2 \delta(E_f - E) \tag{3.6}$$

where $|\phi_0\rangle$ and $|\phi_f\rangle$ denote the ground (0) and final (f) states. The one-body operator describing GRs is of the form

$$O_{JM}^\mu = r^\lambda \left[\vec{\sigma} \otimes \vec{Y}_L \right]_M^J \tau_\mu \tag{3.7}$$

where $\vec{J} = \vec{L} + \vec{S}$, M is the projection of J, $\vec{\sigma}$ is the spin operator, $\vec{Y}_L$ is the spherical harmonic associated with L, τ_μ is the isovector operator in the direction μ, and $\lambda = 2n + L$ where n is the number of major oscillator shells the transition occurs over. For the IVGMR ($n = 1$, $L = 0$, $J = 0$), the operator reduces to

$$O^\mu = r^2 \tau_\mu. \tag{3.8}$$

To define the sum rules associated with the one-body operator (O), the moments of the strength function are taken to be:

$$
\begin{aligned}
m_k(O) &= \int_0^\infty (E - E_0)^k S_O(E) dE \tag{3.9} \\
&= \sum_f (E_f - E_0)^k |\langle \phi_f | O | \phi_0 \rangle|^2 \tag{3.10}
\end{aligned}
$$

with $k = 0, \pm 1, \pm 2, \ldots$ giving the infinite set of moments to describe the strength function [31], and where Equation 3.9 describes continuum states and Equation 3.10 describes discreet states. As described in Reference [31], the moments can be used to define parameters such as average excitation energy ($\langle E_X \rangle = m_1/m_0$) and variance ($\sigma = \sqrt{m_2 - (m_1)}/m_0$). The odd moments of the strength function can be written to allow a model-independent description of the strength, depending only on the operator, the Hamiltonian, and the ground-state wave function [36].

The first-order moment is used to describe GRs and is classified as the energy weighted sum rule (EWSR). The EWSR is of interest because the energy term in the strength function can relate back to intrinsic properties of the nucleus such as the mean excitation energy and can be determined model independently [1, 36]. Taking the first energy moment of the strength function in Equation 3.10 ($k = 1$), the sum rule can be written as [36, 38]

$$m_1(O) = \left\langle \phi_0 \left| \left[O^\dagger, [H, O] \right] \right| \phi_0 \right\rangle \tag{3.11}$$

where $m_1(O)$ is the EWSR, $|\phi_0\rangle$ is the ground state, O is the one-body operator acting on the system, and H is the Hamiltonian of the system.

The non-energy weighted sum rule (NEWSR) is the non-energy moment of Equations 3.9 and 3.10 ($k = 0$). The NEWSR is useful in observing strength exhaustion in charge exchange reactions, as it gives the complete integral of the strength function. In the charge exchange mode, the NEWSR can be written as [38]

$$m_0(O) = \left\langle \phi_0 \left| \left[O^\dagger, O \right] \right| \phi_0 \right\rangle \tag{3.12}$$

where $m_0(O)$ is the NEWSR, $|\phi_0\rangle$ is the ground state, and O is the one-body operator acting

on the system.

The typical starting point for solving Equation 3.6 is to invoke the independent particle model (IPM). In the IPM, the nucleons are assumed to move independently from each other in a mean field produced from interactions of all other particles in the nucleus. A single-particle Hartree-Fock (HF) Hamiltonian is constructed with the self-consistent HF field $(\sum_{i \neq j} v(\vec{r_{ij}}))$

$$H_{HF} = \sum_i \frac{p_i}{2m} + \frac{1}{2} \sum_{i \neq j} v(\vec{r_{ij}}). \tag{3.13}$$

The two-body force used here in the HF approach assumes the so-called residual interaction of multiparticle-multihole states of the nucleus are negligible. To complete analysis in the IPM, the HF ground state is used as a vacuum to set up a complete basis of many-particle wave functions, and the strength function is generated.

When the ground state is approximated reasonably well by a single Slater determinant of single particle orbitals, the random-phase approximation (RPA) gives a good description of the nuclear excitation energy spectrum. The RPA can be viewed as a perturbation on the HF picture in the IPM, where the residual interaction not treated in Equation 3.13 is diagonalized within the model space of 1p-1h excitations.

The starting point for deriving the equations describing the RPA is to use the equations-of-motion (EOM). The EOM method expresses excited states by a creation operator $(Q_f^\dagger)$ acting upon the the ground state

$$|f\rangle = Q_f^\dagger |0\rangle \tag{3.14}$$

where the ground state is defined such that

$$Q_f |0\rangle = 0 \text{ for all } f \qquad (3.15)$$

Here the index f labels the excited states of the system. In this formulation of the RPA with only 1p-1h excitations, taking the commutation relation between the creation operator and the Hamiltonian of the A-particle system and applying an arbitrary variation describes the creation operator as

$$Q_f^\dagger = \sum_{m,i} (X_{mi}^f a_m^\dagger a_i - Y_{mi}^f a_i^\dagger a_m). \qquad (3.16)$$

Here $a_m^\dagger (a_i)$ are creation (annihilation) operators. The absolute squares of X_{mi}^f and Y_{mi}^f give the probability of observing $a_m^\dagger a_i |0\rangle$ and $a_i^\dagger a_m |0\rangle$ as contributing to the excited state $|f\rangle$ [35].

To perform the calculation, a complete set of single-particle wave functions with known single-particle energies and a residual particle-hole interaction is needed. To obtain these components, one can start with a self-consistent HF calculation. In this case the method is denoted 'self-consistent RPA.' Furthermore, if the single-particle continuum is included explicitly, the method is denoted as 'continuum RPA' or CRPA[39].

It is with the inclusion of the continuum in the CRPA, or in further extended RPAs the coupling to more complex np-nh configurations, that one is able to begin to describe more completely the widths of GRs by allowing complex decay modes. As illustrated in Figure 3.2, besides having an inherent width (Γ_{inh}) of the resonance from the spreading in excitation energy due to distribution of the 1p-1h states, the width of a GR is described as

$$\Gamma_{tot} = \Gamma_{inh} + \Gamma^\uparrow + \Gamma^\downarrow \qquad (3.17)$$
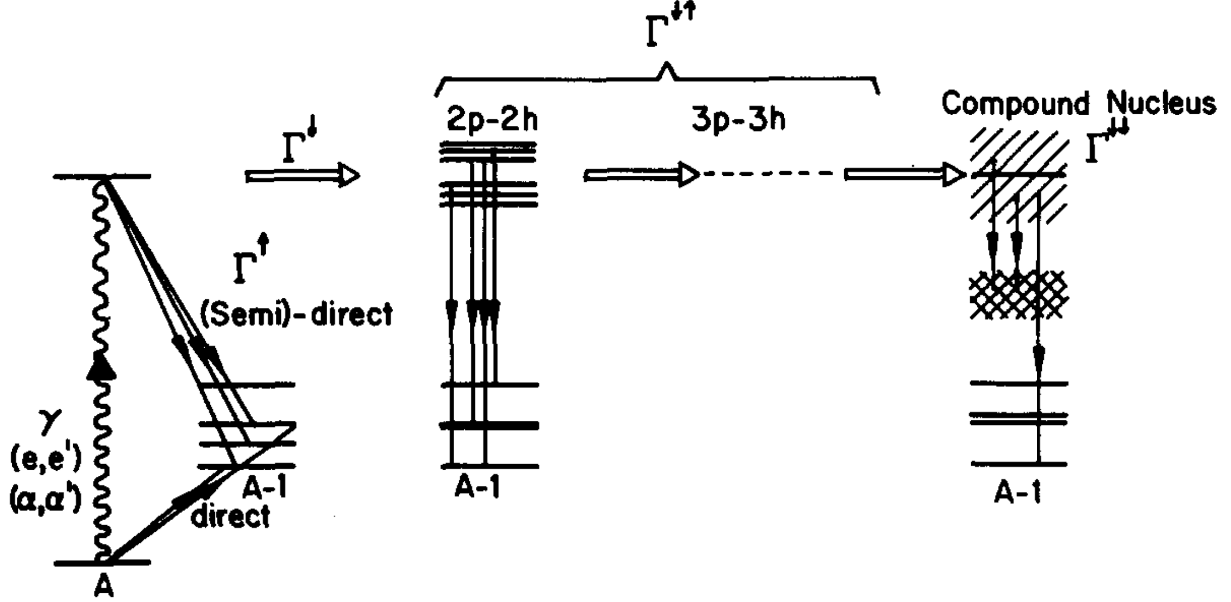
Figure 3.2 Schematic representation of the width of the collective 1p-1h state into a direct component $\Gamma^\uparrow$ and a spreading component $\Gamma^\downarrow$. The spreading component can be further broken into terms describing statistical decay of the equilibrium compound nucleus $\Gamma^{\downarrow\downarrow}$ and decay of the intermediate, pre-equilibrium states $\Gamma^{\uparrow\downarrow}$. Figure reproduced from [40].

where $\Gamma^\uparrow$ describes the direct (and semi-direct) decay mechanism and is called the escape width and $\Gamma^\downarrow$ describes the statistical decay mode and is called the spreading width. Γ_{inh} arises from the spreading in excitation energy of the initial collective 1p-1h strength function, and is large for light nuclei; where the correlated 1p-1h excitation couples with uncorrelated 1p-1h configurations, causing a fragmentation of the correlated wave function [41]. Here it becomes apparent that while macroscopic theories of GRs can begin to address Γ_{inh} and $\Gamma^\uparrow$ of GRs, exclusion of more complex configurations and particle emission into the continuum limits the ability of the theory to describe $\Gamma^\downarrow$ [31].

The escape width $\Gamma^\uparrow$ is a result of the coupling of the correlated 1p-1h state to the continuum, allowing semi-direct decay of the nucleus A into holes states in the (A-1) nucleus. As illustrated in Figure 3.2, the resonance may also compete with knock-out processes for the population of hole states in the (A-1) nucleus. Since a description of the coupling to the
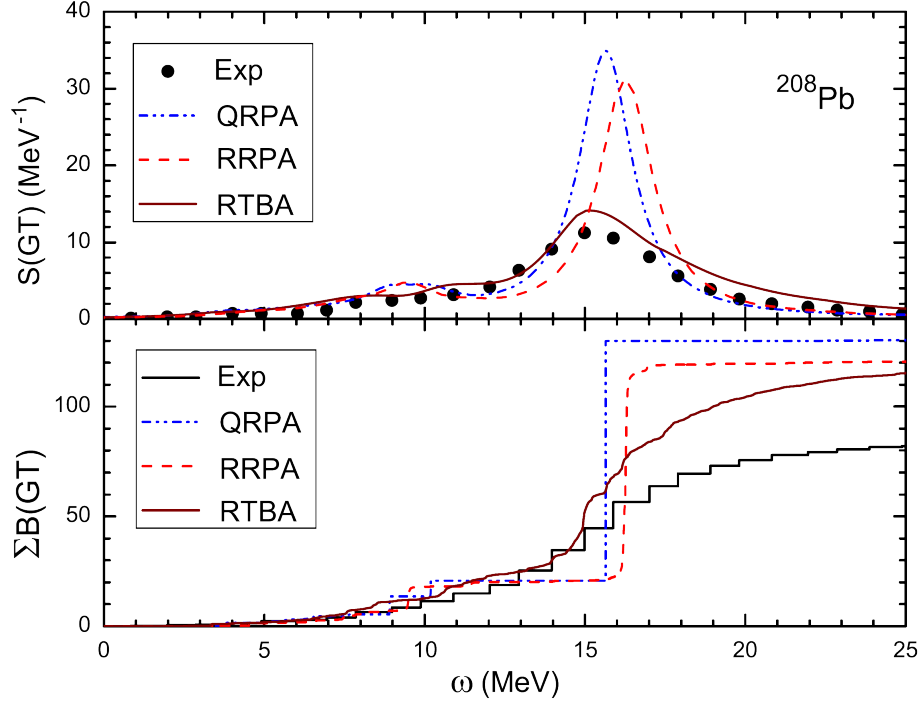
Figure 3.3 Theoretical and experimental GT strength distributions in ^{208}Pb (upper panel) and their cumulative sums (lower panel)[42]. The top panel illustrates the fragmentation of the strength allowed in the RTBA, rather than collecting strength into one major peak. Here ω represents the excitation energy of the ^{208}Pb.

continuum is necessary to adequately describe the escape width, the prediction of this width is model dependent.

The spreading width $\Gamma^\downarrow$ is well understood and can be broken down further into decay of a pre-equilibrium state $\Gamma^{\uparrow\downarrow}$ and an equilibrium state $\Gamma^{\downarrow\downarrow}$ such that the spreading width is

$$\Gamma^\downarrow = \Gamma^{\uparrow\downarrow} + \Gamma^{\downarrow\downarrow} \tag{3.18}$$

. The pre-equilibrium partial width $\Gamma^{\uparrow\downarrow}$ is a result of decay of the resonance at an intermediate state of coupling to more complex np-nh states, and the equilibrium partial width $\Gamma^{\downarrow\downarrow}$ is a result of decay of the compound nucleus.

While the CRPA begins to allow a description of the width of GRs, further developments
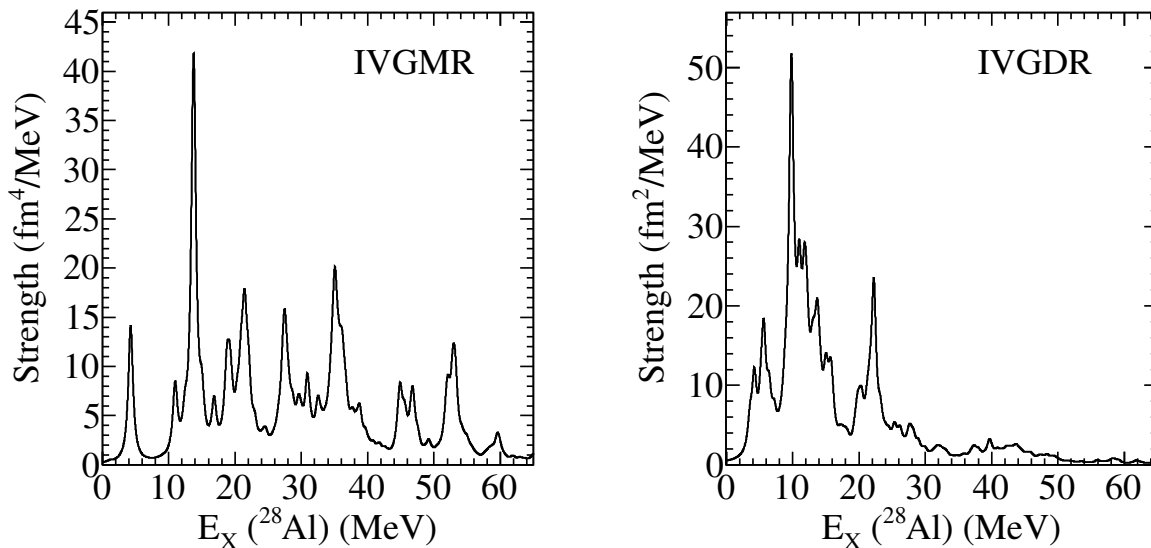
Figure 3.4 Results of the RTBA calculation for the IVGMR and the IVGDR by E. Litvinova [43, 42]. Strengths have been smeared with Lorentzians of 2 MeV in width.

are needed to describe the collective nature and fragmentation of the strength function in excitation energy. For instance, the quasi-particle RPA (QRPA) model was developed to accurately describe collective states. In the QRPA, the inclusion of quasiparticles reproduces ground state pairing correlations more accurately than with just particles; a full description of the QRPA technique can be found in References [44, 45, 46]. While the QRPA does well in describing collective states to give the centroid energies and total strength of the GRs [47], it fails to reproduce the total widths and fine structure [48] since these aspects of the GRs are strongly sensitive to more complex configurations that form $\Gamma^{\downarrow}$ (such as 2p-2h or 4-quasiparticle configurations).

In this study, the relativistic time-blocking approximation (RTBA) is used, a full discussion on the RTBA and its applicability can be found in [48, 43, 42]. The RTBA is similar to the RPAs, but is an extension of the time-dependent covariant DFT which includes particle-vibration coupling. The introduction of the particle-vibration coupling allows fragmentation

of the strength to more realistic distributions, where other RPAs have typically collected strength in large peaks as shown in Figure 3.3 where measured GT strength in ^{208}Pb is compared to QRPA, relativistic RPA (RRPA) [49], and RTBA calculations. The QRPA and RRPA results collect most of the strength into one peak near 16 MeV. The RTBA results are spread across the measured strengths, and reproduce well the distribution.

Calculations for the IVGMR and IVGDR for the ^{28}Si→^{28}Al charge-exchange reaction were performed in the RTBA [43, 42] with operators $O_{IVGMR} = r^2\tau$ and $O_{IVGDR} = rY_1\tau$ by E. Litvinova. Figure 3.4 shows the result of the calculation with a smearing of the point strengths with Lorentzians of width 2 MeV. For the IVGMR, the strength is highly fragmented. The largest peak appears at 14 MeV, with other peaks appearing from 4 to 60 MeV. The IVGDR has a peak collected at 10 MeV and remaining strength distributed to higher excitation energy. The total sum of the strength for the IVGMR and IVGDR calculated in the RTBA is 31.36 fm^4 and 14.67 fm^2, respectively.

Chapter 4

Theoretical Cross-Section Calculations and Applications

Isolation of the isovector monopole strength requires separation of transitions with no transfer of orbital or spin angular momentum ($\Delta L = 0$, $\Delta S = 0$) from all other charge exchange transitions. Separation of the $\Delta L = 0$ component from the measured differential cross-section is performed through a Multipole Decomposition Analysis (MDA) using theoretical angular distributions. A full description of the MDA can be found in chapter 7. This chapter will detail the method used to obtain theoretical differential cross-sections in the Distorted Wave Born Approximation (DWBA). The formalism for such calculations is well established, and excellent references can be found in [50, 51].

The DWBA calculations in this work are done using the package known as `FOLD` [52] which consists of three modules: `WSAW`, `FOLD`, and `DWHI`. `WSAW` calculates the single-particle wave functions in a Woods-Saxon potential for input into the module `FOLD`. `FOLD` produces form factors by double folding the effective nucleon-nucleon (`NN`) interaction over the transition densities for the projectile-ejectile and target-residual systems. The transition densities are obtained through shell model calculations in `NuShellX` [53, 54] when feasible, or through the normal modes formalism [55] using the code `NORMOD` [56]. Finally, cross-sections are obtained with the module `DWHI` by using an optical model potential to create distorted

waves and produce the transition matrix element.

4.1 The Differential Cross-Section

The differential cross-section of a reaction tells us the scattered flux of particles with respect to the incoming flux of particles as

$$\frac{d\sigma}{d\Omega} = \frac{\hat{j}_f(\theta, \phi)}{j_i}. \tag{4.1}$$

where $\hat{j}_f(\theta, \phi)$ is the current of scattered particles in the direction (θ, ϕ) and j_i is the incident flux. Asymptotically, the combined incident and scattered waves are of the form

$$\psi^{asym} = \psi^{beam} + \psi^{scat} \xrightarrow{r \to \infty} A \left[e^{ik_i z} + f(\theta, \phi) \frac{e^{ik_f R}}{R} \right] \tag{4.2}$$

where ψ^{asym} is the asymptotic form of the wave function, ψ^{beam} is the wave function for the beam, ψ^{scat} is the scattered wave, A is the amplitude for the waves in the direction of the beam ($e^{ik_i z}$) and the scattered wave ($e^{ik_f R}/R$), $f(\theta, \phi)$ is the amplitude of the outgoing spherical wave ($e^{ik_f R}/R$), and k is the wave vector for the initial (i) and final (f) state. Equation 4.2 can be combined with Equation 4.1 and the fact that $\vec{j} = \vec{v} |\psi|^2$ to produce

$$\frac{d\sigma}{d\Omega} = \frac{v_f}{v_i} |f(\theta, \phi)|^2 \tag{4.3}$$

30

where $f(\theta, \phi)$ is the amplitude of the outgoing spherical wave induced by a plane wave of unit amplitude, or scattering amplitude, and $v_{f,i}$ are the final and initial velocities, respectively. It can be shown (Ref. [50], Ch. 2) that

$$f(\theta, \phi) \;\; = -\frac{\mu_f}{2\pi\hbar} T_{fi} \tag{4.4}$$

$$T_{fi} \;\; = \langle f \left| T \right| i \rangle \tag{4.5}$$

where T_{fi} are the transition matrix elements connecting the initial and final states, also referred to as the t-matrix, μ_f is the reduced mass of the outgoing particle, and $|f, i\rangle$ are the final and initial wave functions, respectively.

In this formulation of the differential cross-section, the asymptotic behavior of the scattering wave functions must match the boundary conditions of an incoming plane wave and an outgoing spherical wave.

4.2 The Distorted Wave Born Approximation

In this analysis, the transition matrix is calculated by obtaining the transition matrix via truncation of the problem using the Born approximation and separation of the scattering potential into a component that distorts the incoming and outgoing waves and a component containing all residual interactions. These steps, delineated below, comprise what is known as the distorted wave Born approximation (DWBA).

To gain a deeper understanding of the transition matrix, the details of how it arises from the interaction of the incoming wave with the scatterer will be examined. Recalling that the

incoming wave is represented by a plane wave, the behavior of the system is not influenced by any potential resulting in the free Hamiltonian,

$$H_0 = \frac{p^2}{2\mu} \tag{4.6}$$

where p is the momentum and μ is the mass. The Schrödinger equation and radial equation are then

$$(E - H_0)\,|\psi_0\rangle = 0 \text{ and } \langle \vec{r}|\psi_0\rangle = \psi_0(\vec{r}) = e^{-i\vec{k}_i \cdot r}. \tag{4.7}$$

where E is the energy, $|\psi_0\rangle$ is the final wave function, r is the radial direction in spherical coordinates, and k is the wave vector. For the asymptotic form, the scattering potential must be local, i.e.

$$\lim_{r \to \infty} V(\vec{r}) = 0. \tag{4.8}$$

Including this potential, V, into Equation 4.7, letting $H = H_0 + V$,

$$(E - H_0 - V)\,|\psi\rangle = 0 \tag{4.9}$$

where $|\psi\rangle$ is the wave function interacting with V.

The wave function from Equation 4.9 is broken up into the free solution $|\psi_0\rangle$ and the scattered solution $|\psi_S\rangle$

$$|\psi\rangle = |\psi_0\rangle + |\psi_S\rangle. \tag{4.10}$$

32

To obtain the full asymptotic form of the wave function, the solution to the scattered wave is necessary; rearranging Equation 4.10

$$|\psi_S\rangle = |\psi_0\rangle - |\psi\rangle. \tag{4.11}$$

Expanding Equation 4.9 with Equation 4.10

$$(E - H_0)|\psi\rangle = (E - H_0)(|\psi_0\rangle + |\psi_S\rangle) = (E - H_0)|\psi_S\rangle \tag{4.12a}$$

$$= V|\psi\rangle. \tag{4.12b}$$

Relating Equations 4.12a and 4.12b

$$|\psi_S\rangle = (E - H_0)^{-1} V|\psi\rangle \tag{4.13a}$$

$$|\psi\rangle = |\psi_0\rangle + (E - H_0)^{-1} V|\psi\rangle. \tag{4.13b}$$

Equation 4.13b is known as the Lippman-Schwinger equation and can be shown to give rise to the Green's function (Ref. [51], section 3.8)

$$G_0^\pm = G_{H_0}^\pm(E) = \lim_{\epsilon \to 0}(E - H_0 \pm i\epsilon)^{-1} \tag{4.14a}$$

$$G_0^\pm(\vec{r}, \vec{r}') = \frac{1}{(2\pi)^3} \int \frac{\phi(\vec{k}', \vec{r})\phi^*(\vec{k}', \vec{r}')}{E - E' \pm i\epsilon} d\vec{k}' \tag{4.14b}$$

$$|\psi^\pm\rangle = |\psi_0\rangle + G_0^\pm V|\psi^\pm\rangle. \tag{4.14c}$$
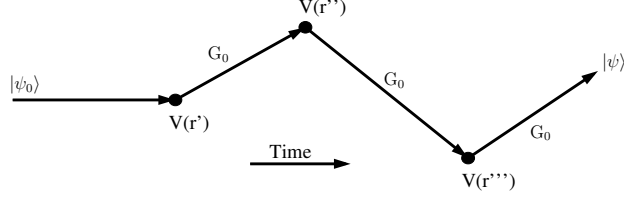
Figure 4.1 Illustration of the propagation of a projectile between scattering events.

where the $+$ and $-$ indicate the outgoing and incoming wave propagation respectively.

The nature of the Green's function can be interpreted as propagating the free projectile between scattering potentials within the scattering region as illustrated in Fig. 4.1. In this manner, each scattering event contributes successively to the final outgoing scattered wave such that the cumulative wave function can be written as

$$|\psi_{new}\rangle = |\psi_0\rangle + G_0^\pm V |\psi_{old}\rangle \tag{4.15a}$$

$$|\psi\rangle = \sum_{n=0}^{N}(G_0^\pm V)^n |\psi_0\rangle, \tag{4.15b}$$

where $|\psi\rangle$ is the outgoing wave, $|\psi_0\rangle$ is the incoming plane wave, and N is the number of interactions. Projecting this onto the space $\vec{r}$

$$
\begin{aligned}
\psi(\vec{r}) &= \left\langle \vec{r} \left| = \sum_{n=0}^{N}(G_0^\pm V)^n \right| \psi_0 \right\rangle \\
&= \psi_0(\vec{r}) + \langle \vec{r} | G_0^\pm V | \psi_0 \rangle + \langle \vec{r} | G_0^\pm V G_0^\pm V | \psi_0 \rangle + \cdots \\
&= \psi_0(\vec{r}) + \int d^3 r' \, G_0^\pm(\vec{r}, \vec{r}\,') V(\vec{r}\,') \psi_0(\vec{r}\,') \\
&\quad + \int \int d^3 r' d^3 r'' G_0^\pm(\vec{r}, \vec{r}\,') V(\vec{r}\,') G_0^\pm(\vec{r}\,', \vec{r}\,'') V(\vec{r}\,'') \psi_0(\vec{r}\,'') \\
&\quad + \cdots
\end{aligned}
\tag{4.16}
$$

34

where $G_0^{\pm} = \frac{e^{ik|\vec{r}-\vec{r}'|}}{|\vec{r}-\vec{r}'|}$.

To account for all events in the scattering region, all terms in Equation 4.15b are collected to define the transition matrix which describes the effect of the scattering region on the wave function.

$$|\psi\rangle = \sum_{n=0}^{N}(G_0^{\pm}V)^n |\psi_0\rangle = |\psi_0\rangle + |\psi_S\rangle \tag{4.17}$$

$$|\psi_S\rangle = G_0^{\pm}\left(V + VG_0^{\pm}V + VG_0^{\pm}VG_0^{\pm}V + \cdots\right)|\psi_0\rangle \tag{4.18}$$

$$= G_0^{\pm}T |\psi_0\rangle \tag{4.19}$$

We see then that the scattered wave is produced from a term that contains the information about scattering points within the scattering region followed by a term that propagates the wave away to the detector. Thus the transition matrix is

$$T^{\pm} = V + VG_0^{\pm}V + VG_0^{\pm}VG_0^{\pm}V + \cdots \tag{4.20}$$

$$T_{BA}^{\pm} = V + VG_0^{\pm}V \tag{4.21}$$

where Equation 4.21 is the Born approximation to first order in the transition matrix (T_{BA}). Applying this to Equation 4.17, the final form of the outgoing wave is of the form

$$|\psi\rangle = |\psi_0\rangle + G_0^{\pm}T_{BA}^{\pm} |\psi_0\rangle \tag{4.22}$$

Returning to Equation 4.16, making the first order Born approximation and taking the asymptotic limit, the integral simplifies

$$\lim_{r \to \infty} \psi\left(\vec{r}\right) = \psi_0\left(\vec{r}\right) + \lim_{r \to \infty} \int d^3 r' d^3 r'' G_0\left(\vec{r}, \vec{r'}\right) T^\pm\left(\vec{r'}, \vec{r''}\right) \psi_0\left(\vec{r''}\right). \tag{4.23}$$

where the label BA has been removed from the transition matrix as this result is independent of the Born approximation. Taking the incident state as a plane wave $\psi_0(\vec{r}) = \mathrm{Exp}[i\vec{k} \cdot \vec{r}] = \mathrm{Exp}[ikz]$ and reducing the Green's function in the asymptotic limit, this reduces Equation 4.16 further to

$$\lim_{r \to \infty} \psi\left(\vec{r}\right) = e^{ikz} - \frac{\mu}{2\pi\hbar^2} \frac{e^{ikr}}{r} \int d^3 r' d^3 r'' e^{-ik\vec{e}(\theta,\phi)\cdot\vec{r'}} T^\pm\left(\vec{r'}, \vec{r''}\right) e^{ik\vec{e}_z \cdot \vec{r''}} \tag{4.24}$$

$$= e^{ikz} - f(\theta,\phi) \frac{e^{ikr}}{r}. \tag{4.25}$$

Comparing Equations 4.24 and 4.25, the form of the scattering amplitude is deduced:

$$f\left(\theta, \phi\right) = -\frac{\mu}{2\pi\hbar^2} \left\langle \psi_0 \left| T^+ \right| \psi_0 \right\rangle \tag{4.26a}$$

$$= -\frac{\mu}{2\pi\hbar^2} \left\langle \psi_0 \left| V \right| \psi^+ \right\rangle \tag{4.26b}$$

$$= -\frac{\mu}{2\pi\hbar^2} T_{fi} \tag{4.26c}$$

where T_{fi} is introduced as short-hand for the transition matrix connecting the incoming and outgoing wave and Equation 4.26b takes only the the first term of the transition matrix

series following the Born approximation.

Following References [50] and [51] to develop the full DWBA, the potential V is split into two components

$$V = U + W \qquad (4.27)$$

where the average potential U describes the elastic scattering of the projectile due to the target and W contains the residual information pertaining to the interaction between nucleons. The distorting potential is then used in the Lippmann-Schwinger equation (Equation 4.13b) to obtain the distorted waves

$$\left|\chi^{\pm}\right\rangle = \left|\psi_0\right\rangle + G_U^{\pm} U \left|\psi_0\right\rangle \qquad (4.28)$$

where $G_U^{\pm}$ is the Green's function defined by the Hamiltonian with potential U. Comparing again with Equation 4.13b, the solution will be of the form

$$\left|\psi^{\pm}\right\rangle = \left|\chi^{\pm}\right\rangle + G_U^{\pm} W \left|\psi^{\pm}\right\rangle . \qquad (4.29)$$

Using this potential, the transition matrix is broken into two parts [51]

$$T_{fi} = \langle \psi_0 \, | U | \, \chi^+ \rangle + \langle \chi^- \, | W | \, \psi^+ \rangle \tag{4.30a}$$

$$= \langle \chi^- \, | W | \, \psi^+ \rangle . \tag{4.30b}$$

where the distorting potential U does not directly connect the initial and final states in a charge-exchange reaction yielding the form in Equation 4.30b. Expanding Equation 4.30b with Equation 4.29 and taking the Born approximation, the transition matrix for the DWBA is obtained,

$$T_{fi} = \langle \chi^- \, | W | \, \chi^+ \rangle . \tag{4.31}$$

Equation 4.31 describes the scattering process. An incoming wave, distorted by the scatterer's potential U, has some nuclear structure which interacts with the scatterer's nucleons via potential W, and exits in a modified form that is also distorted by the potential of the residual of the scatterer. The distortion of the incoming and outgoing waves are taken into account through an optical model to describe the scattering potential. The nature of the interaction between the nucleons (W) participating in the scattering event is not trivial. In practice a form factor describing the potential needs to be taken into account, and is described in Section 4.3. This requires knowledge of the structure of the participating nuclei and the nature of the individual nucleon-nucleon (NN) interaction.

Calculations of the differential cross section in the DWBA were performed using the

code `DWHI` from the package `FOLD` [52]. An essential ingredient to the calculation of the differential cross section in this method are the optical model potentials (OMPs) that distort the incoming and outgoing waves. When available, empirically obtained OMPs are used to describe the potentials that distort the waves. When a suitable OMP is not available for the reacting ions (e.g. ^{28}Si interacting with ^{10}Be, and ^{28}Al interacting with ^{10}B), one may employ various theoretical efforts to obtain the OMP. The method used in this study is described below in Section 4.2.1.

4.2.1 Calculation of Optical Model Potentials

As described in Section 4.2, an essential ingredient in the cross section calculation is the optical model potential that distorts the incoming and outgoing waves. The complex optical potentials used to compute the ^{10}Be-^{28}Si entrance-channel and ^{10}B-^{28}Al exit-channel distorted waves were calculated using the methods used routinely for fast nucleon removal reaction analyses [57]. These employ the double-folding model [58], assuming ^{28}Si and ^{28}Al densities calculated from spherical HF calculations using the SkX parametrization of the Skyrme interaction [59], Gaussian ^{10}Be and ^{10}B densities with root mean squared (rms) radii of 2.30 fm [60], and an effective two-nucleon (`NN`) interaction. A Gaussian `NN` effective interaction is assumed [61], with a range of 0.5 fm. The interaction strength is determined in the usual way [62], from the free pp and np cross sections at 100MeV, with the real-to-imaginary ratios of the forward scattering `NN` amplitudes taken from the tabulation of Ray [63]. OMPs were compared with measured systems from Reference [64] to estimate systematic uncertainties at 10%.

4.3 Form Factors

In Section 4.2, the DWBA was used to simply describe the scattering process in terms of the transition amplitude in equation 4.31.A form factor is calculated by double folding the effective NN interaction over the transition densities of the projectile-ejectile and target residual systems to evaluate the transition amplitude. The resulting form factor is defined as

$$F(\vec{s}) = \left\langle \phi_e \phi_r \left| V_{eff}(\vec{s}) \right| \phi_t \phi_p \right\rangle \tag{4.32}$$

where $\phi_{e,r,t,p}$ represent the single-particle wave functions of the reaction systems. The double-folding over the transition densities of the participant nuclei in the reaction is necessary to account for the composite nature of the nuclei. The coordinates describing the interaction are illustrated in Figure 4.2.

In practice, the the form factor in Equation 4.32 is evaluated by calculating an integral over the target and projectile systems where the transition densities for each system are obtained as a function of $\vec{r}_{p,t}$, the coordinate connecting the interacting nucleons to their core nucleus where p represents the projectile and t represents the target:
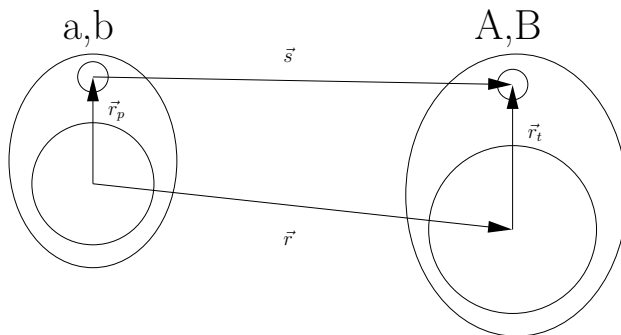
Figure 4.2 Coordinate definitions for the form factor calculation where the projectile/ejectile system is defined with a,b respectively and the target/residual system is defined with A,B respectively.

$$F(\vec{s}) = \int dr_t dr_p \rho_{ab}(\vec{r_p}) V_{eff}(\vec{s}, \vec{r_p}, \vec{r_t}) \rho_{AB}(\vec{r_t}). \tag{4.33}$$

where the transition densities ($\rho_{ab,AB}$) provide the information about the overlap of the final and initial state of the nucleus and are defined as

$$\rho_{LSJ} = \sum_{np} \left\langle f \left\| \left[a^\dagger a \right] \right\| i \right\rangle [\phi^* \phi] \tag{4.34}$$

where i, f are the initial and final states respectively, $a(a^\dagger)$ is the annihilation(creation) operator that acts on the internal wave function of the nucleus to describe the interacting nucleons, and ϕ are again the single-particle wave functions of the nucleus. The reduced matrix element in Equation 4.34 is referred to as the one-body transition density (OBTD).

In this study, the program `FOLD` is used from the package of the same name [52]. The effective interaction and the OBTDs included in this calculation are described in the following subsections. The obtained form factors are then used in the program `DWHI` from the `FOLD` package to calculate the cross section.

4.3.1 The Effective Nucleon-Nucleon Interaction

The effective `NN` interaction (V_{eff}) describes the interaction between the projectile and target nucleons. A phenomenological description of V_{eff} was detailed by Love and Franey in 1981 via a phase shift analysis of `NN` scattering data [21], and updated in 1985 by Franey and Love with an updated data set [65]. In this method, V_{eff} is parameterized by central (V^C), spin-orbit(V^{LS}), and tensor (V^T) contributions to the interaction as

$$V_{12} = V^C(r_{12}) + V^{LS}(r_{12})\vec{L} \cdot \vec{S} + V^T(r_{12})S_{12} \tag{4.35}$$

where 1 and 2 refer to the interacting nucleons, $\vec{L} \cdot \vec{S}$ is the spin-orbit operator, and S_{12} is the tensor operator. Each component of the effective interaction can also be expressed as

$$V^C = V_0 + V_\sigma(r)\vec{\sigma}_1 \cdot \vec{\sigma}_2 + V_\tau(r)\vec{\tau}_1 \cdot \vec{\tau}_2 + V_{\sigma\tau}(r)(\vec{\sigma}_1 \cdot \vec{\sigma}_2) \cdot (\vec{\tau}_1 \cdot \vec{\tau}_2) \tag{4.36}$$

$$V^{LS} = V_{LS}(r)(\vec{L} \cdot \vec{S}) + V_{LS\tau}(r)(\vec{L} \cdot \vec{S}) \cdot (\vec{\tau}_1 \cdot \vec{\tau}_2) \tag{4.37}$$

$$V^T = V_T(r)S_{12} + V_{T\tau}(r)S_{12}(\vec{\tau}_1 \cdot \vec{\tau}_2) \tag{4.38}$$

where σ and τ denote spin and isospin operations respectively.

The terms in Equations 4.36 to 4.38 can be regrouped in terms of the spin-isospin transitions that the potential mediates. In terms of charge exchange reactions, the terms that include τ are of interest. In References [21, 65] it is shown that in the case of zero momentum transfer the central part of the effective interaction (Equation 4.36) is the primary contributor since the spin-orbit term is negligible and the tensor term is small. In Figure 4.3 the amplitudes of the t-matrix for the central components of V_{eff} are shown. The red and blue lines represent the isovector contributions to V_{eff} for the non-spin-transfer and spin-transfer reactions respectively. The square of the volume integral ($|J|^2$) of τ and $\sigma\tau$ components of the effective NN interaction shown in Figure 4.3 illustrate the relative intensity of the peak cross-section as a function of incident beam energy.

For reliable extraction of experimental information about the IVGMR, a clean, single-step $\Delta S = 0$, $\Delta T = 1$ reaction is necessary. This means three requirements must be met.

1. Clean $\Delta S = 0$, $\Delta T = 1$ filter

   The ^{10}Be-^{10}B$+\gamma$ probe acts as the $\Delta S = 0$, $\Delta T = 1$ filter as described in Chapter 1,
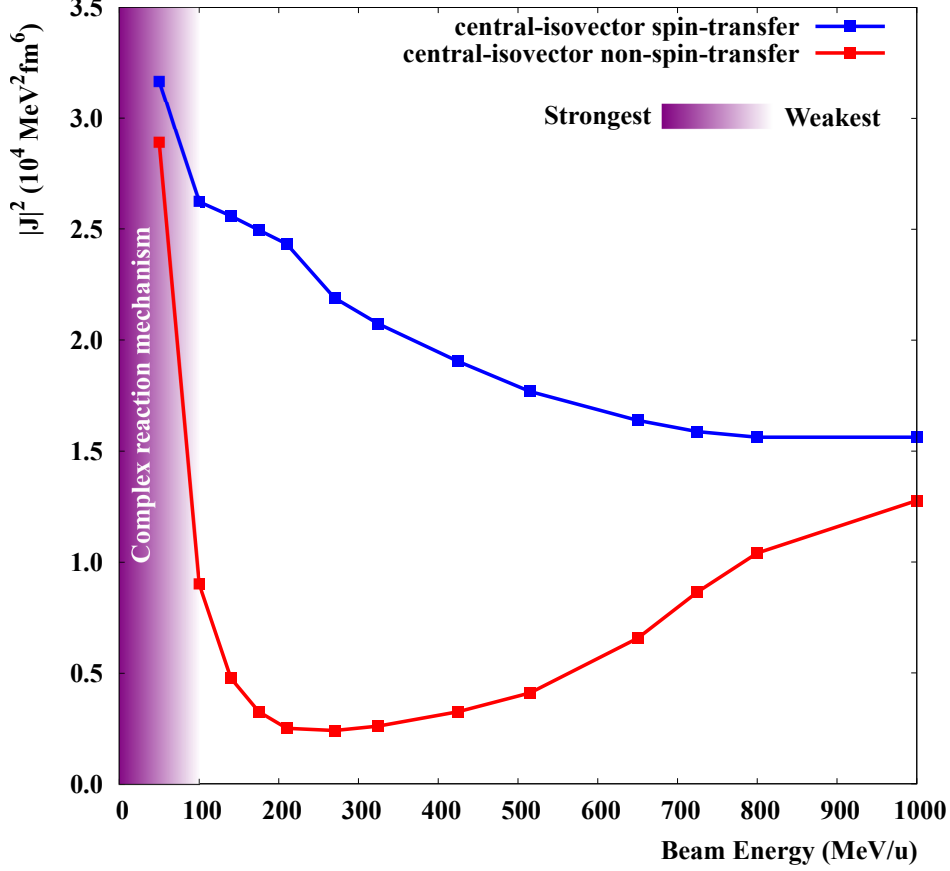
Figure 4.3 Energy dependence of the central components of the effective interaction. The square volume integrals $|J|^2$ are square amplitudes for the the t-matrix representing the transition between final and initial states, from [65]. Shading schematically representing the transition from complex reaction mechanisms to single-step reactions at 100 MeV/u is described in [18].

but the peak cross-section of the V_τ operator is highly sensitive to the incident beam energy. As can be seen in Figure 4.3, the spin-transfer, isovector ($V_{\sigma\tau}$) contribution to V_{eff} is dominant over the V_τ contribution for all but the lowest and highest bombarding energies. Increasing beam energies above 200 MeV begins to increase the relative strength of the V_τ contributions. The same can be achieved by lowering the beam energy, and are in the range of achievable energies in this study. Optimally one would want to lower beam energies such that the V_τ contribution becomes dominant. However, as one lowers beam energies, contributions from complex reactions mechanisms

come into play.

2. Clean single-step CE mechanism

   As illustrated in purple in Figure 4.3, below 100 MeV in incident beam energy, complex, multi-step reactions participate. This makes theoretical description of the reaction more difficult than the direct sing-step reactions assumed in this chapter. An adequate description of the reaction is necessary for separating the multipole (ΔL) components of the observed angular distributions as described in Section 7.1. A balance can be struck at ~ 100 MeV/u where multi-step reactions no longer contribute significantly [18, 64] and V_τ is at its maximum usable level.

3. Probe of nuclear surface

   As shown in Figure 2.2 in Section 2.1, the ^{10}Be-^{10}B probe is strongly absorbed at the nuclear surface. This is important because probing the full volume of the nucleus would reduce the cross-section from cancellation of the strength.

The NN interaction should include exchange terms that represent collisions between nuclei resulting in nucleon exchange. A short-range approximation has been used to estimate the knock-on exchange contributions to the interaction [21], but has been observed to underestimate the destructive contributions for complex probes [66]. In this work, we have attempted to take into account by measuring the over estimation of a known state in Chapter 7, and applying the result to the IVGMR.

4.3.2 One-Body Transition Densities

The one-body transition density (OBTD), as shown in Equation 4.34, represents in a concise manner the most general information needed to connect an initial and final state by the

action of one-body operators. In Equation 4.33, it is shown that the one-body transition density needs to be calculated for both the projectile/ejectile and target/residual systems.

In this study, two methods of calculating the one-body transition densities are employed. For the Fermi and GT transitions in the ^{10}Be-^{10}B system, a shell model calculation was performed to determine the OBTDs. In the ^{28}Si-^{28}Al system where the $1, 2\hbar\omega$ excitations produce configurations outside the major oscillator shell, the calculation in the shell model becomes intractable. For this, OBTDs are calculated in the the normal modes formalism. Descriptions of both methods are covered in the following subsubsections.

4.3.2.1 In the Shell Model

The OBTDs for the ^{10}Be-^{10}B system were calculated using the shell model code `NUSHELLX@MSU` [67, 68]. Schematically, the shell model code calculates the importance of each single-particle transition and the phase factors to incorporate all of the necessary angular momentum coefficients into the OBTD.

4.3.2.2 In the Normal Modes Formalism

The model space necessary to calculate the giant resonance OBTDs in the ^{28}Si-^{28}Al system is much larger than what can be reasonably handled in the shell model calculations referenced above. To obtain the OBTDs for these excitations, a normal modes formalism was employed as described by References [17, 55]. Calculations were performed with the computer code `NORMOD` [55].

The normal-modes calculation gives the most coherent superposition of the 1p-1h excitations for a given operator. They exhaust completely the NEWSR strengths (described in Section 3.2) for the particle-hole operator associated with a resonance, and is generally

defined as

$$O^\mu_{JM} = r^\lambda \left[\vec{Y}_L \otimes \vec{\sigma} \right]^J_M \tau_\mu \tag{4.39}$$

where $\vec{J} = \vec{L} + \vec{S}$, M is the projection of J, $\vec{\sigma}$ is the spin operator, $\vec{Y}_L$ is the spherical harmonic associated with L, τ_μ is the isovector operator in the direction μ, and $\lambda = 2n + L$ where n is the number of major oscillator shells the transition occurs over.

The particle-hole operator O^μ_{JM} connects the initial $|0\rangle$ and final $|JM\rangle$ states. The final state of the nucleus can be written as

$$|JM\rangle = \sum_{ph} X^{JM}_{ph} \left[a^\dagger_p a_h \right]_{JM} |0\rangle \tag{4.40}$$

where

$$X^{JM}_{ph} = \frac{\langle JM| O^\mu_{JM} |0\rangle}{\sqrt{\sum_{ph} |\langle ph; JM| O^\mu_{JM} |0\rangle|^2}} \tag{4.41}$$

and $a^\dagger(a)$ are the raising (lowering) operators for the particle (p) and hole (h) states. The total sum of the multipole strength is described as

$$S_{JM} = \sum_{JM} |\langle JM | O^\mu_{JM} | 0\rangle|^2 . \tag{4.42}$$

The normalization of Equation 4.40 is chosen such that Equation 4.42 exhausts the full multipole strength of the operator O^μ_{JM} [55]. In this definition then, the normal modes are OBTD's.

For the IVGMR in ^{28}Al, the operator takes the form

$$\hat{O}^{IVGMR} = r^2\tau. \tag{4.43}$$

As pictured in Figure 2.1, the particle-hole transitions excited are $\left(0s_{1/2} \rightarrow 1s_{1/2}\right)$, $\left(0p_{3/2} \rightarrow 1p_{3/2}\right)$, $\left(0p_{1/2} \rightarrow 1p_{1/2}\right)$, and $\left(0d_{5/2} \rightarrow 1d_{5/2}\right)$. The total strength calculated in this process is 28.6 fm^4, but no information is given in this method about the strength distribution as a function of excitation energy.

A calculation was also performed for the IVGDR in ^{28}Al, where the operator now takes the form

$$\hat{O}^{IVGDR} = rY_1\tau. \tag{4.44}$$

Here the total strength calculated is 15.2 fm^2.

4.3.3 Single-Particle Wave functions

An important ingredient to the form factor calculation is the inclusion of single-particle (s.p.) wave functions. S.P. wave functions for the one-particle and one-hole states connected by the OBTD are calculated using the program `WSAW` from the the `FOLD` package [52]. A necessary input for the calculation is the binding energy of the single-particle states participating in the excitation. These were calculated using the `NUSHELLX@MSU` package with the `DENS` function [67], employing the SkX Skyrme interaction [59]. The procedure to obtain the radial wave functions from `WSAW` requires fitting the solutions to the Schrödinger equation such that they match the binding energies.

π \ J	0		1		2		3	
	L	S	L	S	L	S	L	S
+	**0**	**0**	0	1	**2**	**0**	4	1
			2	1	2	1	2	1
−	1	1	1	1	1	1	**3**	**0**
			1	**0**	3	1	3	1

Table 4.1 Possible angular momentum transfers, separated by parity. Highlighted in red are the $\Delta S = 0$ used in this study.

4.4 Results of Calculation

Cross sections were calculated in this study from the ground states of ^{28}Si and ^{10}Be. Calculations were performed for excitations of isovector, non-spin-flip ($\Delta T = 1$, $\Delta S = 0$) reactions of multipoles $\Delta L = 0, 1, 2,$ and 3 in the ^{28}Si-^{28}Al system. In this text, the angular momentum transfer ΔL will be used interchangeably with the total angular momentum transfer $\Delta J = \Delta L + \Delta S$ since $\Delta S = 0$ reactions are of interest. Table 4.1 indicates some of the angular momentum transfers that are possible in nuclear reactions. Since the $(^{10}$Be,^{10}B+$\gamma)$ probe isolates the $\Delta T = 1$, $\Delta S = 0$ reactions, the highlighted transitions show that ΔJ and ΔL may be used interchangeably when addressing only $\Delta S = 0$ reactions.

The cross sections are to be applied in the multipole decomposition analysis of the measured data, as described in Section 7.1. To decompose the entire spectrum, the calculations were performed across a range of reaction Q-values that span the observed excitation energy spectrum. Calculated angular distributions at 15 MeV, which is in the expected energy region of the IVGMR, are shown in Figure 4.4.

Similar to the calculation above, angular distributions were also calculated for the ^{12}C$(^{10}$Be,^{10}B$)^{12}$B reaction since data were also taken for this reaction. The interest here is to measure the ^{12}C$(0^+$,g.s.$)\rightarrow^{12}$B$(1^+$,g.s.$)$ transition, which is a GT($0\hbar\omega,\Delta L = 0,\Delta S = 1,\Delta T = 1$) reaction (whereas the IVGMR is $2\hbar\omega$, $\Delta L = 0$, $\Delta S = 0$, $\Delta T = 1$). The measurement of this state
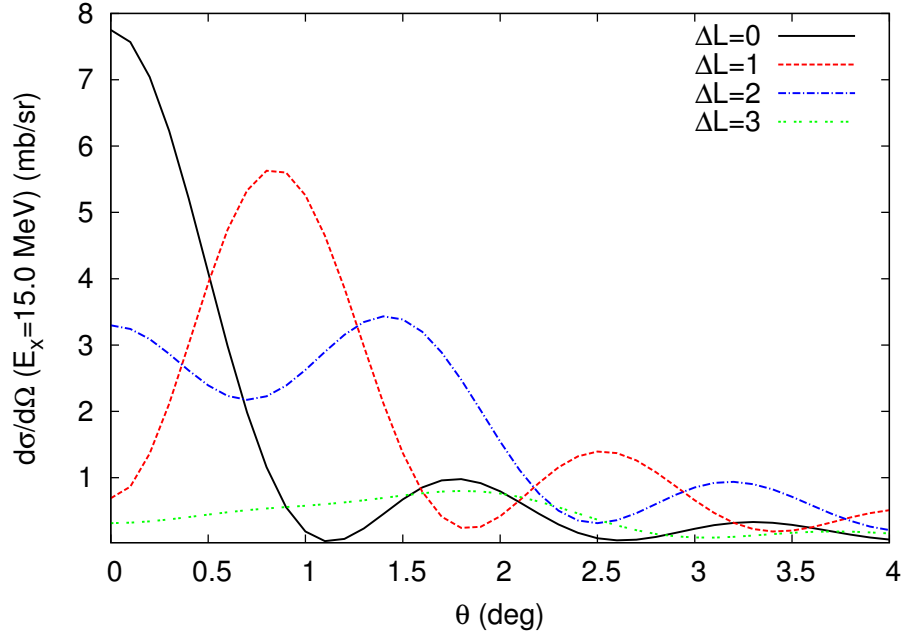
Figure 4.4 Angular distributions for ^{28}Si(^{10}Be,^{10}B)^{28}Al as calculated with   FOLD, at $E_X = 15.0 MeV$.

will allow an estimation of the over calculation of the DWBA cross-section as described at the end of Section 4.3.1, and implemented in Chapter 7. Figure 4.5 shows the results of the calculation for the GT transition to the ground state of ^{12}B. For this data set, calculations were only performed for transitions to the ground state of ^{12}B for evaluation.
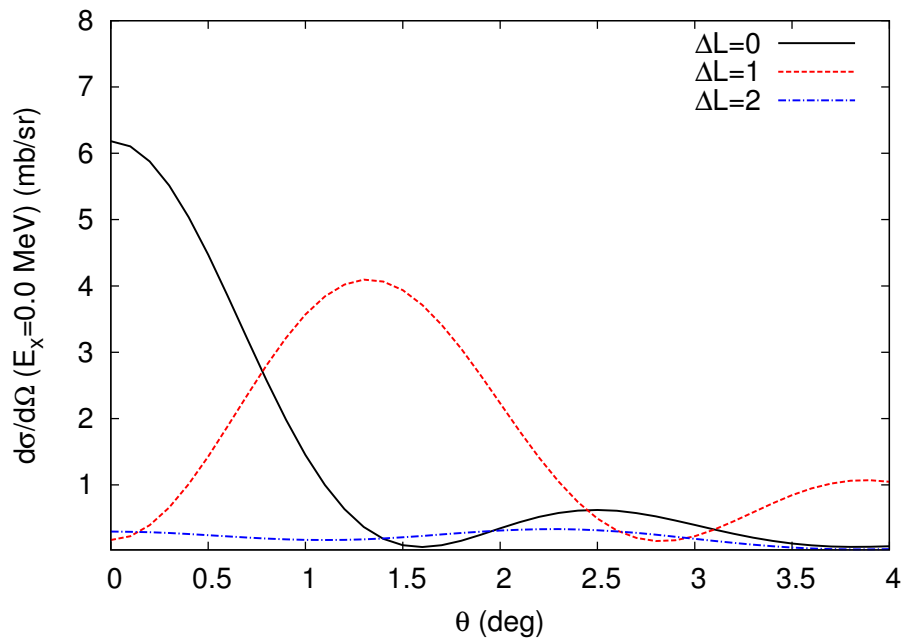
Figure 4.5 Angular distributions for ^{12}C(^{10}Be,^{10}B)^{12}B as calculated with FOLD, at $-2.0 < E_X \le 2.0$ MeV. Some contamination of the GT transition to the ground state of ^{12}B is due to the 0.95 MeV 2^+ state and the 1.67 MeV 2^- state, so dipole contributions are calculated as well.

Chapter 5

Experiment

Experiment 11021 ran in June of 2013 at the National Superconducting Cyclotron Laboratory (NSCL) with the purpose of isolating the IVGMR using the (^{10}Be,^{10}B+γ) charge exchange probe for its sensitivity to the non-spin-flip reaction channel. This chapter details the production of ^{10}Be and the experimental devices used for detection of the reaction.

5.1 Beam Preparation and Delivery

Rare isotope beams at the NSCL are produced in a fast fragmentation process at intermediate energies. A stable isotope of heavier mass than the particle of interest is accelerated to relativistic speeds through the Coupled Cyclotron Facility (CCF) at the NSCL [69] and impinged upon a thick fragmentation target (typically Beryllium). Many of the resulting ejectiles have been broken up, or fragmented, by the target, and since the fragments are produced in flight, relatively short-lived isotopes can be guided to the experimental stations.

The in-flight fragments are purified in the so-called A1900 fragment separator [70]. In this process the fragments are separated by their magnetic rigidity, typically resulting in a highly purified beam of the isotope of interest. The highly purified beam is then transported to the experimental vaults of the NSCL.
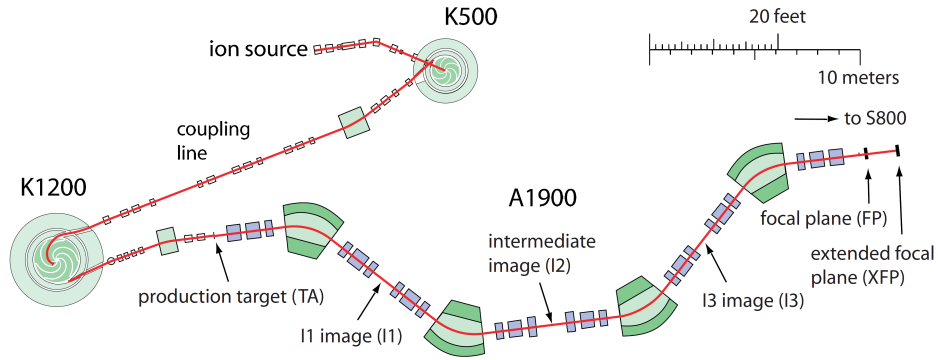
Figure 5.1 Schematic overview of the coupled K500 and K1200 cyclotrons and the A1900 Fragment Separator

5.1.1 Coupled Cyclotrons

The Coupled Cyclotron Facility at the NSCL [69] consists of two particle accelerators, the K500 and the K1200 as shown in Figure 5.1, for the production of primary beams of 100 to 160 MeV/u. The numeric naming of the cyclotrons indicate the maximum extraction energy for protons. The purpose of coupling the cyclotrons was to allow for higher intensities, as well as raising the energy limits for heavier ions.

Operationally, ions in an intermediate charge state are injected into the K500 cyclotron to accelerate them to an intermediate energies of 8 to 12 MeV/u. The beam is then extracted into the coupling line between the K500 and K1200 for injection into the K1200 where the ions are stripped to their final charge state. The extracted beam from the K1200 at 100 to 160 MeV/u is extracted to the production target at the entrance of the A1900 Fragment Separator for fragmentation and separation to what is called the secondary beam.

5.1.2 A1900 Fragment Separator

The A1900 Fragment Separator, pictured on the right of Figure 5.1, serves to select specific ions from the fragmentation products of the fast primary beam bombarding the production

target. The A1900 employs four 45° dipole bending magnets and 8 quadrupole triplet magnets for focusing the beam. The ion selectivity comes from the four dipole bending magnets, which separate the ions by their magnetic rigidity ($B\rho$).

Since the force on the ion due to a dipole magnet causes the ion to travel in a circle, the force observed by the ion due to the magnetic field can be related to the centripetal motions as

$$F = \frac{\gamma m v^2}{\rho} = QvB \tag{5.1}$$

where $\gamma = 1/\sqrt{1 - (v/c)^2}$ is the Lorentz factor to account for relativistic effects, m is the mass of the ion, v is the ion velocity, ρ is the gyroscopic radius of the particle due to the dipole magnetic field, Q is the charge of the ion, and B is the magnetic field of the dipole. The related forces can be rearranged to define the magnetic rigidity:

$$B\rho = \frac{\gamma m v}{Q}. \tag{5.2}$$

From left hand side of Equation 5.2, for a constant magnetic setting in the dipole, the magnetic rigidity defines the radius of curvature of the ion through the magnetic field. Furthermore, for a beam consisting of different, fully ionized, isotopes the momentum-to-charge ratio determine the radius of curvature. In the A1900, the magnetic field of the dipoles are set such that the the path of the ion of interest is bent by 45° through each dipole.

The A1900 system is two-staged. In the first stage, the cocktail of ions coming from fragmentation in the production target pass through the two dipoles magnets before the intermediate image point (see Figure 5.1) to be dispersed by their magnetic rigidity. At the

intermediate image point, an aluminum wedge can be placed to produce a spread in the velocity of the beam particles since energy deposited depends on Z^2 as described by the Bethe formula, as given in Reference [71],

$$\frac{dE}{dx} = \frac{4\pi e^4 Z^2}{m_0 v^2} n_{abs} z_{abs} \left(\ln \frac{2m_0 v^2}{I} - \ln \left(1 - \frac{v^2}{c^2} \right) - \frac{v^2}{c^2} \right) \tag{5.3}$$

where e is the electronic charge, m_0 is the electron rest mass, Z and v refer to the atomic number and velocity of the beam particle, and n_{abs}, z_{abs}, and I refer to the number density, atomic number, and average ionization potential of the absorber material, respectively. By altering the velocity of the beam ions as a function of Z^2, the second stage of the A1900 will further disperse the ions in the beam by their new $B\rho$. Following the two-stage fragment separation in the A1900, there are two slits in the focal plane that can close to further isolate the ion of interest by its rigidity.

For this study, a 120 MeV/u beam of ^{18}O was impinged upon a 1316 mg/cm^2 thick Be target to produce the fragmented beam. A 800 mg/cm^2 aluminum wedge was place at the intermediate image point of the A1900. Slits to restrict the momentum spread of the beam were set to $\frac{dp}{p} = \pm 0.25\%$. In the extended focal plane of the A1900, a suite of detectors are available which allow for particle identification of the transmitted beam (for method see Section 6.2). Using these detectors, it was determined that the ^{10}Be secondary beam extracted from the A1900 was 88% isotopically pure, with contamination coming from ^{8}Li and ^{12}B.

5.1.3 Incoming beam rate measurement

To determine the absolute cross-section, the incoming beam rate must be known. Often, when one measures the beam rate, a detector is placed in the path of the beam to signal as particles pass through. However, use of such a device would introduce more energy straggling in the beam than necessary and degrade the final energy resolution of the measurement, and would be limited to low beam rates.

Therefore, the incoming beam rate was monitored throughout the experiment using a non-intercepting probe (Z001IC) at the exit of the K1200 and a Faraday bar (Z026RC) on the inside wall of the A1900's first dipole magnet as shown in Figure 5.2. This current was then correlated to the count rate of ^{10}Be in the focal plane of the S800 spectrograph (see Figure 5.3). The beam was impinged upon a ^{28}Si (35.35 mg/cm^2) target, and the S800 was tuned to select the unreacted beam. A purity of 98% ^{10}Be was observed in the focal plane, allowing for calibration of the incoming beam rate. An incoming beam rate of greater than 7 MHz of ^{10}Be was observed; incident particles were tabulated for each experimental run.

Early in the experiment, the calibrated beam rates for Z001IC and Z026RC were consistent, as shown in Figure 5.4. However, after a retune of the beam line, Z001IC read a significantly lower value in current and did not have a consistent calibration, as indicated in a systematic drop of beam rate following run 142. Therefore, device Z026RC was used for the incident particle measurement.

5.2 Technical Description of the ^{10}B+γ Measurement

The experimental end-station was located in the S3 vault of NSCL, see Figure 5.3. To perform the momentum analysis of the ^{10}B reaction ejectile, the large-acceptance, high-
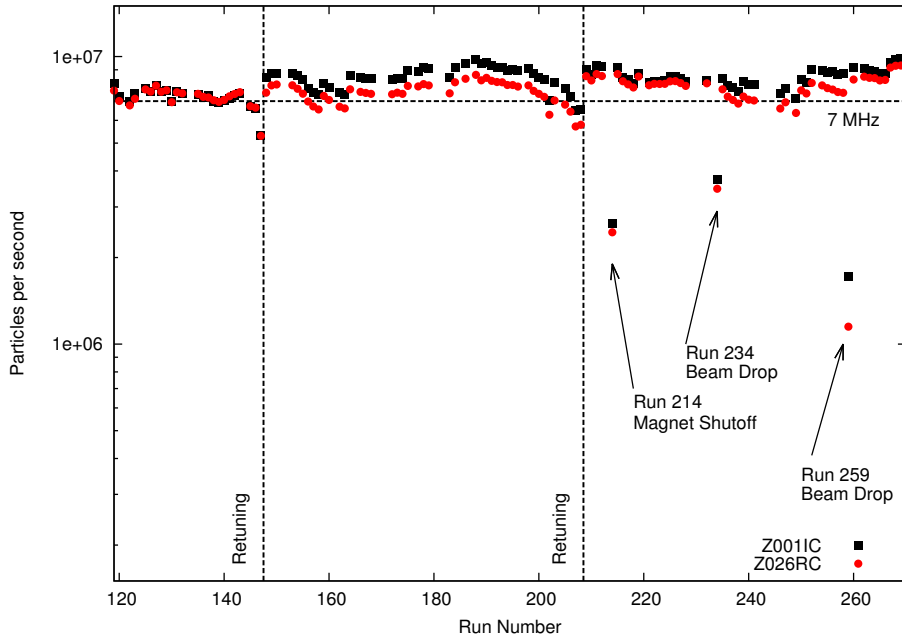
Figure 5.2 Incoming beam rate of ^{10}Be as measured by the non-intercepting probe Z001IC and the Faraday bar Z026RC. Cause for outliers from the trend are indicated with arrows. Also noted are when the beam was returned.

resolution S800 Spectrograph [24] was utilized. The beam line to the spectrograph was matched to the dispersion of the S800 such that the momentum spread of the beam was minimized in the S800 focal plane. In the S800 focal plane detector suite [72] (see Figure 5.5), detectors allowed for beam trajectory tracking and particle identification. Surrounding the S800 target position was the Gamma-Ray Tracking In-beam Array (GRETINA) [73] for the measurement of the Doppler-reconstructed γ-rays.

It was necessary to operate the S800+GRETINA system for this experiment to isolate the ^{10}B particles from other sources of background and to select the single-step, non-spin-transfer CE events as described in Chapter 1 from those produced via other reaction mechanisms. The method of particle identification and gamma analysis will be discussed in Chapter 6.
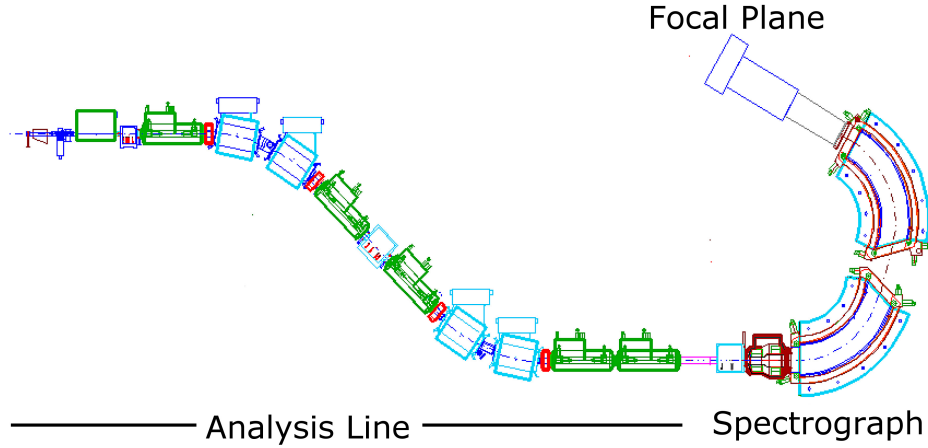
Figure 5.3 Schematic depicting analysis line and spectrograph components of the S800 Spectrograph

5.2.1 S800 Spectrograph

5.2.1.1 Ion Optics Through a Plane Symmetric Magnetic Field

Before examining the dispersion matching technique utilized for optimal energy resolution in the S800 spectrograph, some of the optical ideas behind the movement of the ions through the S800 spectrograph will be examined. The following discussion is to first-order, and will only cover up to the path of an ion through a dipole magnet, as those present in the S800 spectrograph. A complete discussion can be found in Reference [75].

For a general optical system between two profile planes as shown in Figure 5.6 with no optical elements between them, the trajectory of the ion in the $\hat{x}$-direction to first-order is defined as

$$
\begin{pmatrix} x_2(z) \\ tan(\alpha_2(z)) \end{pmatrix} = \begin{pmatrix} (x_2|x_1) & (x_2|tan\alpha_1) \\ (tan\alpha_2|x_1) & (tan\alpha_2|tan\alpha_1) \end{pmatrix} \begin{pmatrix} x_1 \\ tan(\alpha_1) \end{pmatrix} \tag{5.4}
$$

where terms of the form $(B|A)$ are the transport matrix elements that detail the path of
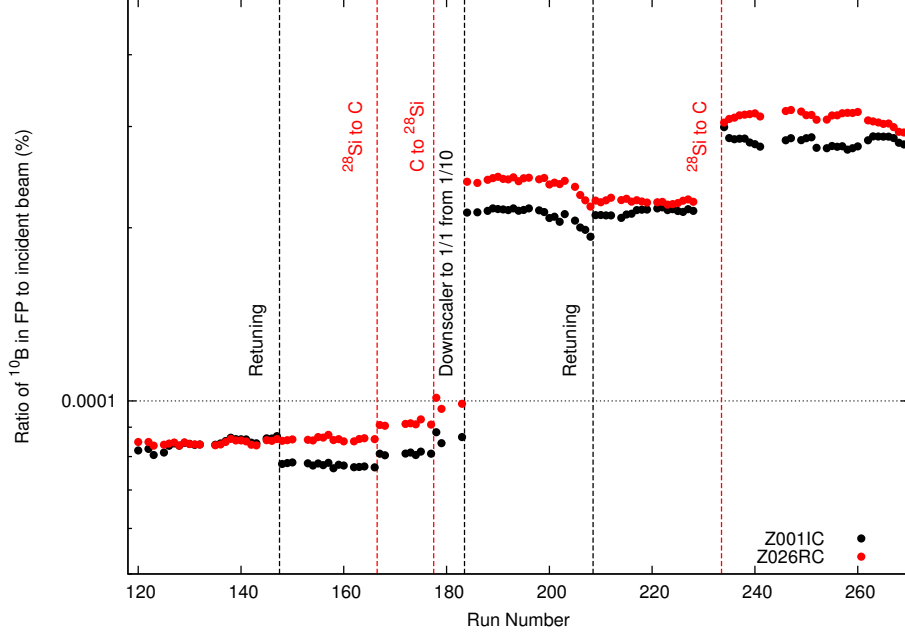
Figure 5.4 Ratio of ^{10}B in focal plane of S800 to incident beam rate as a figure of merit for determining suitability of beam probe. Following run 143 and retuning of the beam, the calibration is lost in the non-intercepting probe Z001IC. Red dashed lines indicate target changes, and black dashed lines indicate changes to the experimental setup that would effect the beam rate.

the projectile from profile plane 1 $|A)$ to profile plane 2 $(B|$. The $\hat{y}$-direction have a similar relation with position y and angle β. The equation can be reduced by introducing the conjugate momenta a, b where $a = v_x/v$ and $b = v_y/v$ where v is the speed of the ion:

$$
\begin{pmatrix} x(z) \\ a(z) \end{pmatrix} = \begin{pmatrix} (x|x) & (x|a) \\ (a|x) & (a|a) \end{pmatrix} \begin{pmatrix} x_1 \\ a_1 \end{pmatrix}
\tag{5.5}
$$

where the subscripts have been dropped in the matrix element notation now.

For the S800, the dipole magnets operate with a field $B_y = B_0 \neq 0$, $B_x = B_z = 0$ where $\hat{z}$ is the beam axis. This optical 'lens' is placed between the two profile planes of Figure 5.6. Due to the Lorentz force, ions travel in circles around the magnetic field such that for an ion of velocity $\vec{v} = v_z \hat{z}$
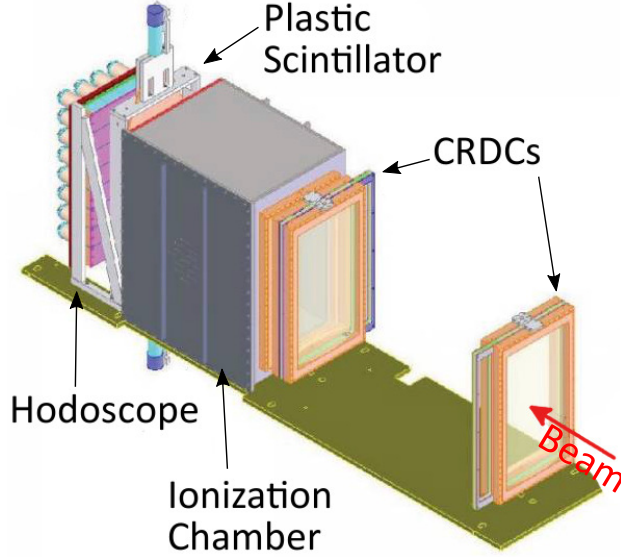
Figure 5.5 Schematic depicting the S800 focal plane detector suite. The Hodoscope was not utilized in this study [74].

$$\vec{F} = Q\left(\vec{v} \times \vec{B}\right) = -Qv_z B_y \hat{x} \tag{5.6}$$

where $\hat{x}$ is deemed the dispersive direction and $\hat{y}$ is the non-dispersive direction. For ions of different magnetic rigidities (see Section 5.1.2 for definition) in a field of constant magnetic flux, the gyroscopic radius (ρ) is defined as

$$\rho = \rho_0(1 + \delta_p) \tag{5.7}$$

where ρ_0 is the trajectory of a central ray through the field and $\delta_p = \frac{p - p_0}{p_0}$ is the momentum deviation from the central ray. Since the momentum and charge of the ion are constant through the magnetic field, δ_p remains the same between the two profile planes and Equation 5.5 can be expanded as
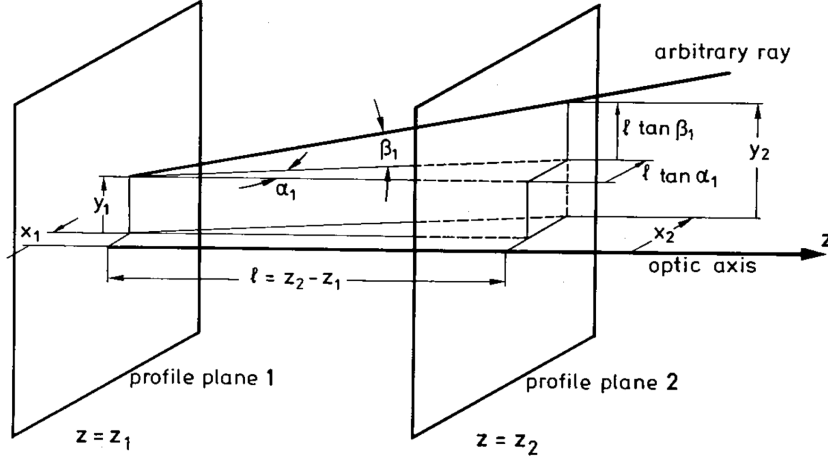
Figure 5.6 Deviations of a particle from the optic axis in a drift length $l = z_2 - z_1$. Taken from Reference [75].

$$
\begin{pmatrix}
x_2 \\
a_2 \\
\delta_p
\end{pmatrix}
=
\begin{pmatrix}
(x|x) & (x|a) & (x|\delta_p) \\
(a|x) & (a|a) & (a|\delta_p) \\
0 & 0 & 1
\end{pmatrix}
\begin{pmatrix}
x_1 \\
a_1 \\
\delta_p
\end{pmatrix}.
\tag{5.8}
$$

Definitions for the transport matrix elements can be found in Reference [75].

5.2.1.2   Dispersion Matching

The secondary ^{10}B beam, isolated by the A1900 Fragment Separator, was transported through the analysis line of the S800 spectrograph (Figure 5.3). The analysis line consists of four dipole and five quadrupole triplet magnets, and has two modes of operation: focused mode and dispersion matched mode. Focus mode transports the beam to the focal plane such that the image is chromatic, and the momentum resolution is determined by the momentum spread of the beam. Dispersion matched mode operates such that the momentum dispersion of the analysis line is compensated for in the dipole magnets of the S800, and the momentum resolution is optimized with all other experimental conditions held constant.
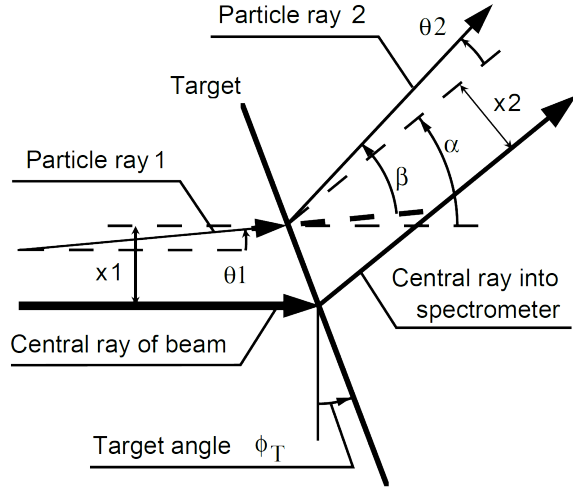
Figure 5.7 Schematic layout of the incident particle 1 and the outgoing particle 2 relative to the beam and spectrometer. Taken from Reference [77].

For this study, the dispersion matched mode was chosen for optimal energy resolution.

In the S800 spectrograph, profile plane 1 is at the entrance to the analysis line and profile plane 2 is the focal plane. As one can see in Figure 5.3, many optical devices are placed between the profile planes, each with an associated transfer matrix. Following the procedure of Reference [76] and discussion by Reference [77], one can follow the ion from the entrance to the analysis line to the target position, from the scattered ion to the focal plane in the dispersive direction as

$$
\begin{pmatrix} x_{fp} \\ a_{fp} \\ \delta_{fp} \end{pmatrix} = S \underbrace{\begin{pmatrix} x_2 \\ a_2 \\ \delta_2 \end{pmatrix}}_{\substack{\text{Behind} \\ \text{target}}} \leftarrow \underbrace{T}_{\substack{\text{Target} \\ \text{transformation}}} \leftarrow \underbrace{\begin{pmatrix} x_1 \\ a_1 \\ \delta_0 \end{pmatrix}}_{\substack{\text{In front} \\ \text{of target}}} \leftarrow B \underbrace{\begin{pmatrix} x_0 \\ a_0 \\ \delta_0 \end{pmatrix}}_{\substack{\text{Entrance to} \\ \text{analysis line}}}. \tag{5.9}
$$

where the conjugate momenta a, b have been replaced with the ion's angle with respect to the beam. So, for a particle entering the analysis line with coordinates $(x_0, \theta_0, \delta_0)$ where δ is the beam dispersion, Equation 5.9 can be interpreted as an ion being transported down the

61

beam line (matrix B) to the target position $(x_1, \theta_1, \delta_1)$ where the optical elements do not change the energy $(\delta_1 = \delta_0)$. The target transformation includes the information, illustrated in Figure 5.7 about the reaction angle α and an arbitrary target angle ϕ_T such that the 'absolute' scattering angle is

$$\beta = \alpha + \theta_2 - \theta_1 = \alpha + \Theta \tag{5.10}$$

where Θ is the relative scattering angle and the target function $T = \mathrm{Cos}(\alpha - \phi_T)/\mathrm{Cos}(\phi_T)$ relates the transformation $x_1 \to x_2$ as

$$x_2 = Tx_1. \tag{5.11}$$

Furthermore,

$$\delta_{fp} = \delta_2 = K\Theta + C\delta_0 \tag{5.12}$$

where K is a kinematic broadening factor $(K = (1/p_{out})(\partial p_{out}/\partial \alpha))$ and C is referred to as the dispersion matching factor [78] (though C shares the same name, it does not define the dispersion matching discussed here).

The transformation to the focal plane can be defined as [79]

$$x_{fp} = x_0(s_{11}b_{11}T + s_{12}b_{21})$$

$$+ \theta_0(s_{11}b_{12}T + s_{12}b_{22})$$

$$+ \delta_0(s_{11}b_{16}T + s_{12}b_{26} + s_{16}C)$$

$$+ \Theta(s_{22} + s_{26}K) \tag{5.13}$$

$$\theta_{fp} = x_0(s_{21}b_{11}T + s_{22}b_{21})$$

$$+ \theta_0(s_{21}b_{12}T + s_{22}b_{22})$$

$$+ \delta_0(s_{21}b_{16}T + s_{22}b_{26} + s_{26}C)$$

$$+ \Theta(s_{22} + s_{26}K) \tag{5.14}$$

where suffices 1,2, and 6 of the matrix elements represent x, θ and relative momentum differ-ence δ, respectively for the matrices $B = b_{\mu\nu}$ and $S = s_{\mu\nu}$ where $\mu, \nu = 1, 2, 6$. The matrix elements in the notation of Section 5.2.1.1 are, for example, $s_{11} = (x|x)_S$, $b_{16} = (x|\delta)_B$, and $b_{26} = (\theta|\delta)_B$ where subscripts S, B denote matrix elements for the spectrometer and extracted beam transport in the analysis line, respectively.

For perfect dispersion matching in position and angle, the coefficients of θ_0, Θ, and δ_0 must be zero. If these conditions are met for Equation 5.13, but not Equation 5.14, it is referred to as 'lateral dispersion matching.' If the conditions are satisfied for both Equations 5.13 and 5.14, it is referred to as 'lateral and angular dispersion matching.'

As mentioned earlier, the S800 spectrograph can be operated in a chromatic (no dispersion matching) mode or in an achromatic (lateral dispersion matching) mode. Since the S800 spectrograph will be solely used to both identify and reconstruct the energies of the ^{10}B
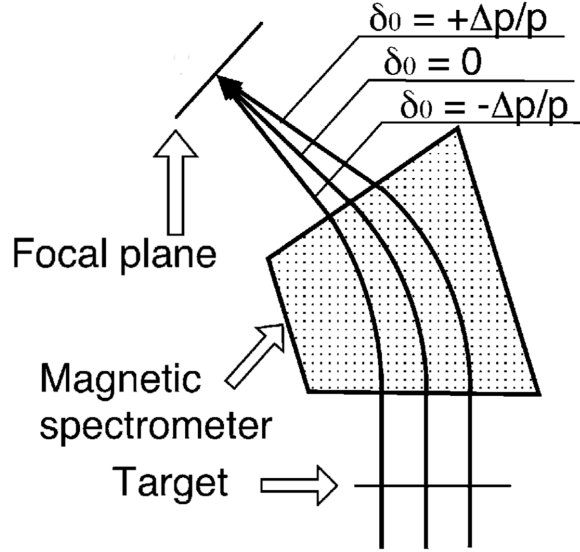
Figure 5.8 Cartoon depiction of lateral dispersion-matching, adapted from Reference [77]. Dispersion of rays with different momenta is compensated by the dispersion of the spectrometer.

ejectiles, it was operated in the achromatic mode. Figure 5.8 illustrates the lateral dispersion matching. Set in this mode, the momentum dispersion of the primary beam entering the spectrograph is compensated by tuning the B, S matrix elements, focusing particles of the same momentum to the same position in the spectrograph.

Cancellation of the coefficients of θ_0 in Equation 5.13 requires

$$s_{12} = -s_{16}K. \tag{5.15}$$

Tuning for this condition could come from changing the focal plane location, but this changes the dispersion and resolution. More practically, one can tune element s_{12} using quadrupoles to adjust the position and angle correlation [76] since $s_{12} \sim (x|\theta)_S$.

For cancellation of the coefficients of δ_0 in Equation 5.13, the requirement can be rearranged as,

$$b_{16} = -\frac{s_{16}}{s_{11}} \left(\frac{C}{T} - b_{26} \frac{K}{T} \right). \tag{5.16}$$

For $K = 0$ (light particle on heavy target), the dispersion matching condition has the size of the beam spot in the focal plane independent of the dispersion of the beam:

$$D_B = - \left(\frac{D_S}{M_S} \right) \tag{5.17}$$

where $D_B = b_{16}$ is the dispersion of the analysis line, $\left(\frac{D_S}{M_S} \right) = \frac{s_{16}}{s_{11}}$, D_S is the dispersion of the spectrometer, M_S is the magnification of the spectrometer, and $\frac{C}{T} \sim 1$.

For the matched system, the remaining term of Equation 5.13 will define the resolution. Substituting Equation 5.15 into the coefficient of x_0, the overall magnification is defined as

$$M_{ov} = s_{11} b_{11} T - s_{16} b_{21} K. \tag{5.18}$$

The resolving power of the system is then [76]

$$R = \left(\frac{1}{2x_0} \right) \left(\frac{s_{16}}{M_{ov}} \right) \tag{5.19}$$

where x_0 is the beam spot size at the S800 image, $s_{16} = D_S$, $M_{ov} = M_S$, and energy resolution is given by

$$R_E = \frac{1}{R} = \frac{2M_S x_0}{D_S}. \tag{5.20}$$

In practice, the S800 spectrograph dispersion matching, shown in Equation 5.17, can be checked by observing the position resolution of a state in the first cathode readout drift

chambers (CRDC). For the S800 spectrograph $D_S = -9.6$ cm/%, $M_S = -0.89$, and in dispersion matched mode the analysis line has a dispersion $D_B = -10.8$ cm/% [80]. Further more, for an object beam spot of 0.05 cm, the maximum achievable resolution is 1/10,000 (for Equation 5.20, $R = \frac{2 \times 0.05}{10.8} = 0.009\%$), and Equation 5.17 holds to better than 0.1%.

The momentum acceptance was limited to $\pm 0.25\%$ in the A1900 fragment separator to allow for an unobstructed transmission of the beam to the focal plane since the momentum spread of the beam at the target position of the S800 spectrograph is large in dispersion matched mode. With this momentum spread, and the dispersion D_B of the analysis line, the beam spot on target was about 5.3 cm.

5.2.1.3 Focal Plane Detectors

After passing through the dipoles of the S800 spectrometer, the ^{10}B ejectiles are then detected and tracked in the S800 focal plane detector array [72]. In this experiment, the focal plane detector suite consisted of detectors for measuring the trajectory, position, energy loss, and time-of-flight information of the ^{10}B.

The position and trajectory of the ^{10}B are measured using two cathode readout drift chambers (CRDCs) separated by 1073 mm, as shown in Figure 5.9. The CRDCs have an active area of 30 cm×59 cm and an active depth of 1.5 cm, with momentum dispersion along the 59 cm direction [72]. Each CRDC has a position resolution of about 0.5 mm in each direction [24]. The CRDCs were filled with a mixture of 20% isobutane and 80% carbon tetrafluoride at a pressure of 50 Torr [72]. A negative bias voltage is applied across the CRDC in the y direction. The gas is ionized by projectiles passing through and the released electrons drift toward an anode wire, held at a constant voltage, where they are collected. Calibration procedures for the CRDC signals are described in Chapter 6.
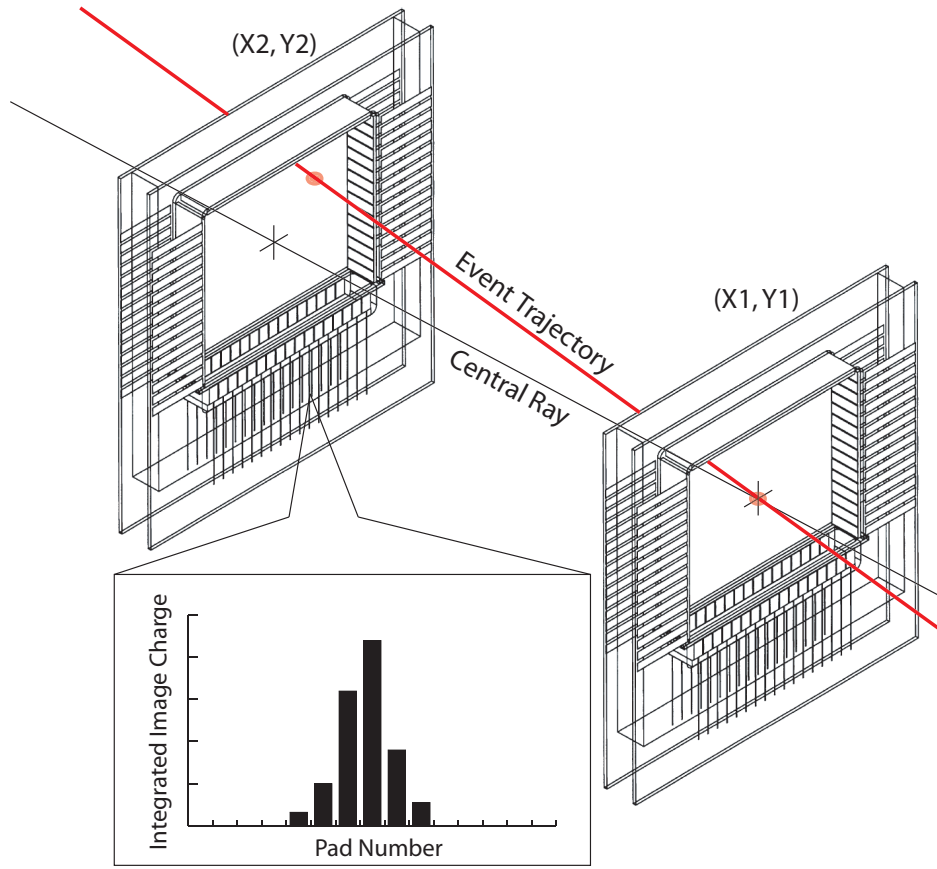
Figure 5.9 Layout of CRDC detectors and cartoon of cathode position determination. Figure taken originally from Reference [72], modified by Wes Hitt in Reference [81]

To determine the x position of the projectile, a cathode consisting of 224, 2.54 mm pads has charge induced on each pad from the ionization electrons drifting toward the anode [72]. A typical image charge distribution is shown in Figure 5.9. A Gaussian distribution was fit to the image charge on the pads, and the centroid defines the x position.

To determine the y position of the projectile, the drift time of the ionized electrons from the projectile position to the anode is utilized. The drift time is determined by the difference between the anode signal time and the event stop signal from the E1 scintillator further down the beam line of the focal plane (the E1 scintillator is described below).

Following CRDC 2, is an ionization chamber consisting of 16 one-inch anodes and filled with a mixture of P10 gas (90% argon, 10% methane) at a pressure of 140 Torr to measure

the energy loss of the reacted beam [72]. The projectile ionizes the gas as it passes through with positive ions being collected at the cathode and the electrons are collected at the anode, where the signal here represents the energy loss through the medium. As noted in Equation 5.3, the energy loss of a particle through a medium is proportional to the square charge (Z^2) of the projectile, allowing determination of the atomic number for particle identification (discussed in Chapter 6).

Downstream of the ionization chamber in the E1 position of the focal plane is a large area (30×59 cm) thin (5 mm thick) plastic scintillator [25]. The E1 scintillator has photomultiplier tubes positioned at the top and bottom, which give energy, position, and timing information for the projectile. The 5 mm thick E1 scintillator was used in this experiment since the signal obtained can be related to energy loss through the scintillator. Though the energy loss signal was not used in this study for particle identification, the energy loss signal helped to reduce additional background (see Chapter 6). The timing of the signal, relative to the RF-signal of the cyclotrons, was used to measure the time-of-flight of the particles.

5.2.1.4   Trajectory Reconstruction in the S800 Spectrograph

The trajectory of the ejected ^{10}B is reconstructed by using the 2 CRDCs in the focal plane of the S800 spectrograph. The target position coordinates are then reconstructed through a ray tracing procedure to relate the focal plane coordinates to the target position. The ray tracing procedure is accomplished by fitting the measured magnetic fields with Enge functions of the form

$$E(z) = \frac{1}{1 + \text{Exp}[P(z)]} \tag{5.21}$$

where z is the direction of a reference path of the beam and $P(z)$ is a fifth order polynomial chosen to fifth order such that the error in the mapping is comparable to the focal plane detectors of the S800 spectrograph [24]. This information is then used as input into the code COSY Infinity [82] to produce an inverted matrix ("inverse map") to relate the focal plane and target position coordinates.

The analytic approach to the inverse map has the benefit of relating positions and angles measured in the focal plane to positions, angles, and energy at the target position. In first order, the inverse mapping appears as

$$(dta, yta, ata, bta) = S^{-1}(xfp, yfp, afp, bfp)$$

$$= \begin{pmatrix} (dta|xfp) & (dta|yfp) & (dta|afp) & (dta|bfp) \\ (yta|xfp) & (yta|yfp) & (yta|afp) & (yta|bfp) \\ (ata|xfp) & (ata|yfp) & (ata|afp) & (ata|bfp) \\ (bta|xfp) & (bta|yfp) & (bta|afp) & (bta|bfp) \end{pmatrix} \begin{pmatrix} xfp \\ yfp \\ afp \\ bfp \end{pmatrix} \tag{5.22}$$

where focal plane coordinates end in "fp" and target position coordinates end in "ta." $x(a)$ refers to the dispersive position (angle) and $y(b)$ refers to the non-dispersive position (angle). Since the dispersive direction is sensitive to the energy spread of the beam, as discussed in Section 5.2.1.1, given the four degrees of freedom as input from the focal plane (xfp, yfp, afp, bfp), one can choose two of the three degrees of freedom in the output for the dispersive direction at the target position. dta is the fractional energy spread of the beam

$$dta = \frac{E - E_0}{E_0} \tag{5.23}$$

where E_0 is the energy of a particle traveling along the reference path through the spectrometer.

Focal plane position calculations and results of the ray tracing are found in Chapter 6.

5.2.1.5 Angular Resolution Improvement in Non-Dispersive Direction

The energy resolution is determined by the thickness of the reaction target, the momentum kick due to γ-emission of the ejectile, and from the intrinsic resolution of the S800 spectrometer. Optimizing the dispersion matching allows for the best possible reconstruction of the excitation energy of the target residual (see Section 6.3), where the momentum spread of the beam and the angular resolution play a role.

More importantly, to isolate the IVGMR from other $\Delta S = 0$, $\Delta T = 1$ events, the best possible angular resolution is crucial. This is because a multipole decomposition analysis (see Section 7.1) is implemented, where the shape of the cross section angular distributions are used to isolate the $\Delta L = 0$ components.

To accomplish this, the beam was defocussed in the non-dispersive direction. It has been observed previously [37] that slightly defocussing the beam in the non-dispersive direction introduces a correlation between the target position variables yta and bta as shown in the left panel of Figure 5.10. To observe the correlation, the unreacted ^{10}Be beam is transported to the focal plane of the S800 spectrograph. The total spread in bta in this setting is 40 mrad . Since the correlation is a single-valued function, a fit of the data can interpolate the correlation and thereby straighten it out. To this end, a function of the form

$$bta = a + b \, \mathrm{ATan}(c + d * yta) \qquad (5.24)$$
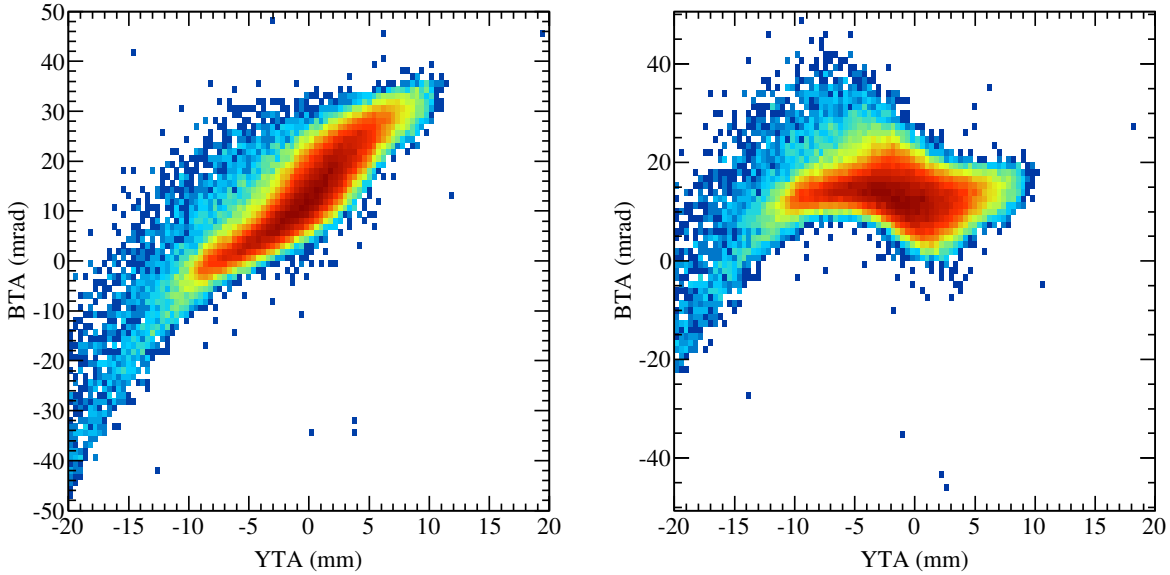
Figure 5.10 (Left) Effect of introduction of correlation in non-dispersive coordinates YTA and BTA through defocusing of the beam. (Right) Result of polynomial fit to correlation in YTA and BTA

was fit for the parameters a, b, c and d to correct for the correlation, as shown in the right panel of Figure 5.10. The correction resulted in an improved spread in bta of 27 mrad.

5.2.2   Gamma Ray Detection

The driving motivation behind this measurement is the ability to isolate the IVGMR from the IVSGMR as described in Chapter 1. The ability to do this is dependent upon separating spin-transfer reactions from non-spin-transfer reactions. By using the $(^{10}\text{Be},^{10}\text{B}+\gamma)$ probe, isolation of the isovector, non-spin-transfer reactions is possible through a coincident measurement of the ^{10}B ejectile and an associated gamma ray "tag" of non-spin-transfer reactions, as described in Section 2.2. The ^{10}B ejectile is measured in the S800 spectrograph's focal plane, as described in the previous section. For detecting gamma rays emitted in-flight by the ^{10}B, it was crucial to have the highest possible signal to noise ratio for measurement
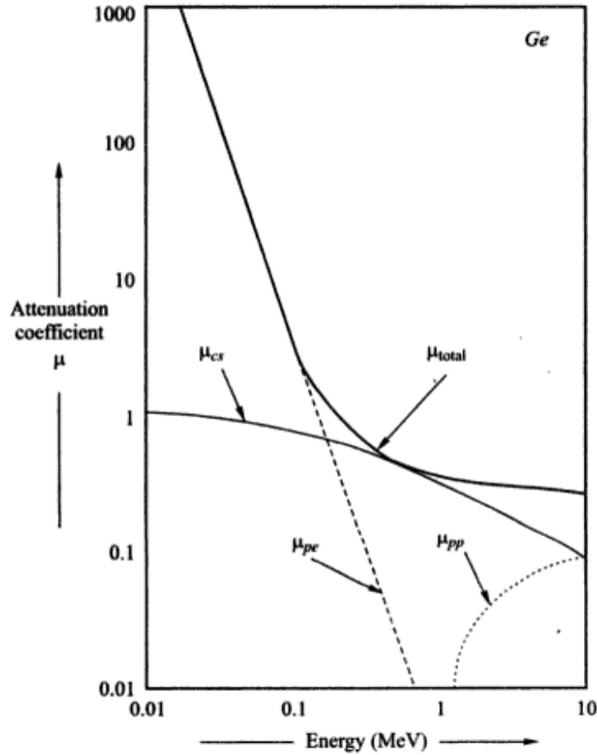
Figure 5.11 Linear attenuation coefficient as a function of photon energy in germanium. The components for the photoelectric absorption, Compton scattering, and pair production are shown as well as the total sum μ_{total}. Figure taken from Reference [83]

of the gamma of interest, therefore the Gamma-Ray Energy Tracking In-beam Nuclear Array (GRETINA) [73] was used for this measurement.

Electromagnetic radiation can interact with material in several ways, and is well described in Reference [71]. The probability that a photon will undergo an interaction per unit path length traveled in a material is called the linear attenuation coefficient, μ, such that a beam of monoenergetic photons incident upon a material of thickness t will be attenuated to an intensity I from an initial intensity before passing through the material I_0:

$$I = I_0 \ \text{Exp}[-\mu t].$$
(5.25)

Here μ is described by three processes that remove the gamma ray from the beam either by

absorption or by scattering away from the detector:

$$\mu_{total} = \mu_{pe} + \mu_{cs} + \mu_{pp} \tag{5.26}$$

were μ_{pe} describes photoelectric absorption, μ_{cs} describes Compton scattering, and μ_{pp} describes pair production. The relative size of each contribution is shown in Figure 5.11. A gamma ray incident on the germanium detector and undergoing photoelectric absorption transfers its entire energy to the detection material, releasing a photoelectron for detection. This is the dominant process for low energy gammas, up to about 0.2 MeV. Compton scattering is the dominant process up to about 8 MeV. In this process, the incident gamma ray undergoes an inelastic collision with an electron, resulting in a scattered photon with an energy less than the incident gamma ray and a free electron with an energy of that lost by the incident gamma ray. Finally, in pair production the gamma ray is of sufficient energy to produce an electron and positron pair that carry off the remaining energy of the gamma ray in the form of kinetic energy. This is the dominant process above 8 MeV, but is first energetically possible at 1022 keV since the rest mass of both the electron and positron is 511 keV. For this experiment, the gamma ray energies of interest are well below the region where pair production processes dominant, and photoabsorption and Compton scattering are the primary methods of interaction with the detector material.

In a measured gamma ray spectrum, there can be a 1022 keV peak due to the pair production process. As discussed in Section 2.2, the transition energy of interest in this experiment is of 1022 keV. This is not an issue in this experiment since the pair production peak is not observed in the coincident data (See Chapter 6). The measured gamma ray is from in-flight decay of the ejectile, and requires Doppler-correction as defined by

73

$$E_\gamma = \frac{E_{\gamma,lab}(1 - \beta\mathrm{Cos}\theta)}{1 - \beta^2} \qquad (5.27)$$

where E_γ is the Doppler-corrected energy of the gamma ray, θ is the angle between the emitted gamma ray and the emitting particle, and $\beta = v/c$, where v is the velocity of the emitting particle and c is the speed of light. The Doppler-correction process corrects for the smearing observed from the in-flight decay at relativistic speeds.

As can be seen in Equation 5.27, the Doppler-corrected energy of the gamma rays are dependent upon E_γ, lab, β, and θ. This means that the broadening of the Doppler-corrected gamma ray not only depends on the uncertainty in the velocity of the particle (β), but also the uncertainty in the intrinsic energy resolution of the detector (ΔE) and the uncertainty in the angle between the gamma ray and the scattered projectile ($\Delta\theta$). Since ΔE and $\Delta\theta$ are gamma detector dependent, to optimize the resolution, it is best to choose a detector system with excellent spatial resolution. It is also important to choose a detector with high efficiency as well as high resolution to increase the signal-to-noise ratio of the measurement to reduce the uncertainty that will be present when subtracting off the background present underneath the peak.

At the time of running the experiment, there were three gamma detection systems at the NSCL: the Caesium Iodide Array (CAESAR) [84], the Segmented Germanium Array (SeGA) [85], and GRETINA [73]. The cross section for the IVGMR is small, even for the lightest elements probed (see Section 2.3). As such, given a choice of gamma-ray detector systems, not only is energy resolution critical, but so is detector efficiency. CAESAR is a sodium-doped caesium iodide (CsI(Na)) array that provides high efficiency gamma ray measurements, but with an intrinsic energy resolution of 10% FWHM for a 1 MeV gamma-
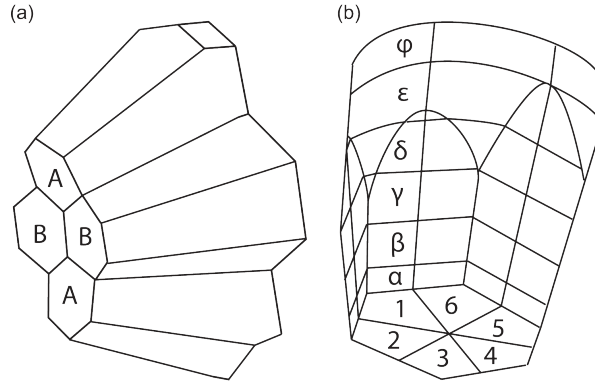
Figure 5.12 Schematic drawing of (a) four crystals packed into one module, two A-type crystals and two B-type crystals and (b) an individual crystal showing the electrical segmentation of its outer contact. Figure from Reference [73]

ray after Doppler correction, CAESAR did not have the optimum energy resolution [84]. The latter two detection systems are composed high-purity germanium (HPGe) detectors, and while delivering good efficiency, HPGe systems typically have intrinsic energy resolutions of about 0.2% for 1 MeV gamma-rays after Doppler-correction. For this study, GRETINA was chosen as the optimal detector system.

5.2.2.1 GRETINA and Detector Placement

GRETINA [73] is placed around the reaction target for detection of gamma-rays in coincidence with the ^{10}B observed in the S800 focal plane. GRETINA is an array of twenty eight 36-fold segmented HPGe crystals designed for detection and tracking of gamma-rays scattering into the germanium crystals. Each crystal is about 90 mm in length and 80 mm in diameter with segmentation into six slices and six regions, with two crystal geometries implemented such that the crystals may be grouped by fours to cover 1/4 of the full 4π solid angle as shown in Figure 5.12.

With each GRETINA module containing four of the 28 crystals, seven modules were available at the time of the experiment. Each module could be placed in a variety of positions
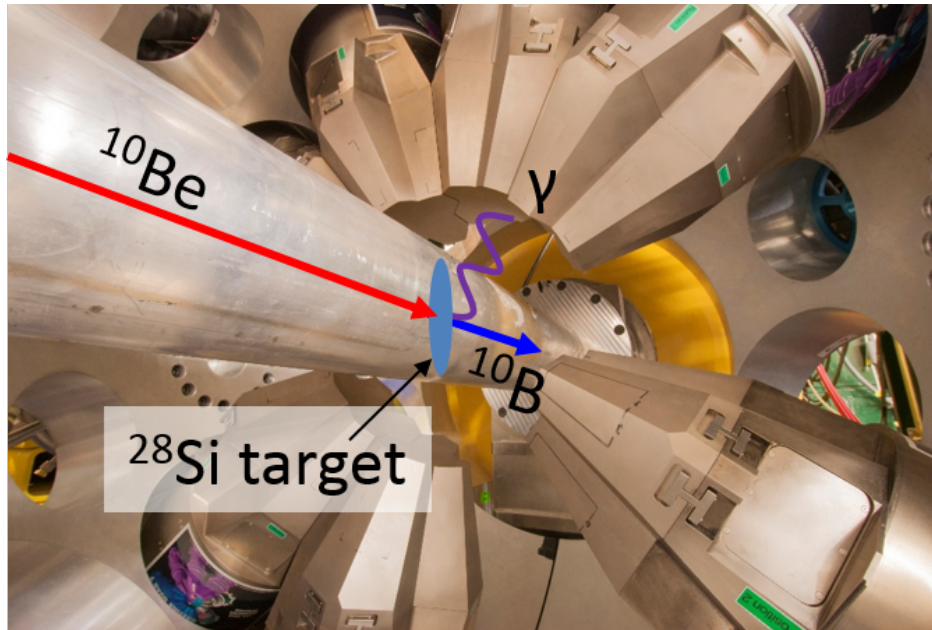
Figure 5.13 Experimental setup of the GRETINA detector array with all 7 detectors placed in their 90° location surrounding the S800 spectrograph target position. Cartoon representations of the reaction of interest are drawn on the photograph. Photograph taken by Shumpei Noji.

surrounding the target location of the S800 spectrograph. At the NSCL, detector positions were offered at 58° (4 positions), 90° (8 positions), and 122° (4 positions) relative to the beam direction. In this experiment, all seven modules populated 90° positions in the detector frame as shown in Figure 5.13, where the reaction of interest is illustrated on the picture.

The modular nature of GRETINA, as well as the electrical segmentation of the crystals, work to improve the resolution of the detector system beyond just the intrinsic energy resolution of germanium because the detector system can be arranged for optimal experimental conditions and one can obtain sub-segment resolutions. The Doppler-corrected energy resolution depends on three factors, as seen in Equation 5.27: the intrinsic energy resolution of germanium (ΔE_{intr}), the uncertainty in the source velocity due to the slowing down of the projectile in the target ($\Delta\beta$), and the uncertainty in the emission angle of the gamma ray due to the finite opening angle of the gamma-ray detector and ambiguity of the scattered
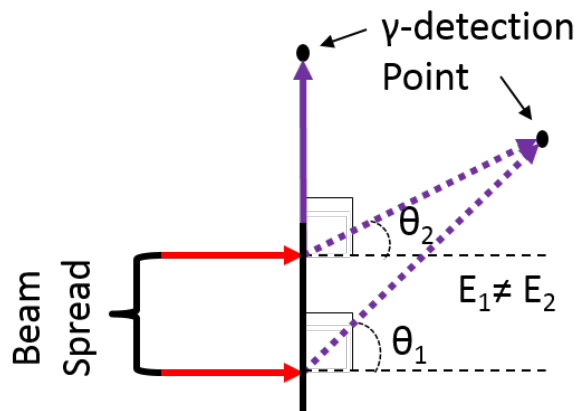
Figure 5.14 Cartoon depiction of angular uncertainty for forward angled detectors due to large beam spot as a result of dispersion matching. Image not drawn to scale.

particle ($\Delta\theta$). The segmentation of the germanium crystals, as shown in Figure 5.12, reduce the angular uncertainty of the Doppler-corrected gamma-ray by allowing precise determination of the hit position with in the crystal, significantly improving the reconstructed energy resolution.

However, a large contribution to the angular uncertainty comes from the large beam spot size necessary for dispersion matching, see Section 5.2.1.2. As shown in Figure 5.14, the large beam spot on the target introduces ambiguity in the emission angle at forward angles, since reactions at the bottom of the target appear in the detector the same as reaction at the top of the target. By placing the detectors at $90°$ with respect to the beam line at the target position, this effect is reduced. The remaining contribution to the angular uncertainty in the measurement is then a result of detector geometry.

In fact, in Table 5.1, the relevant parameters for using a simulation [28] of the resolution and detection efficiency of GRETINA at the NSCL for the 1.022 MeV transition in ^{10}B are listed and show the improvement due to detector position selection. It was decided from this information to use the configuration of all detectors placed at $90°$ surrounding the target position since the gain in resolution was critical, while the loss in efficiency was

	Implemented		Alternative	
GRETINA Detector Positions	All at 90°		4 at 58°, 3 at 90°	
^{10}Be Beam Energy	100 MeV/u			
^{28}Si Target Thickness	40 mg/cm^2			
Beam Spot Size, Dispersive Direction	50 mm			
	Resolution	Efficiency	Resolution	Efficiency
1.022 MeV $\Delta S = 0, \Delta T = 1$ Tag	1.9%	9.4%	4.2%	11.7%

Table 5.1 Relevant parameters used in the simulation of GRETINA resolution and detection efficiency of the 1.022 MeV transition in ^{10}B [28]. The Implemented column represents the configuration used in this experiment. The Alternative column represents another possible configuration for measurement.

tolerable. The requirement of higher energy resolution of the Doppler-reconstructed gamma ray stems from the method of separating the gamma signal from the background in the spectrum. This is done through a "side-band study" where the background next to the signal is used to characterize the background of the gamma peak. Further details of the Doppler-reconstruction and observed resolutions are found in Section 6.1.2.2.

Chapter 6

Data Analysis

The purpose of this chapter is to take the raw data obtained in Chapter 5 and convert it into the physical quantities used to identify the IVGMR: excitation energy, scattering angle, and differential cross-sections. Data was taken in the summer of 2012 during the S800+GRETINA campaign at the NSCL. Data taken were analyzed "online" during the experimental run using the SpecTcl package at the NSCL [86], which was modified to support the attached GRETINA data acquisition system [73]. The "online" mode served to ensure quality data during the experimental run, and the full "offline" analysis of the data was performed using the analysis package `GrROOT` [87].

The analysis was performed in three steps: event building, calibration, and physical calculations. To perform the event building, a raw event file, containing detector response information along with a time stamp, is analyzed and events are time correlated to produce a reduced data file, termed an "event built" file. Calibrations are performed for each detector on the event built file, to produce a calibrated event file. The physical quantities of interest are then determined by calculations performed on the calibrated signals from each detector.
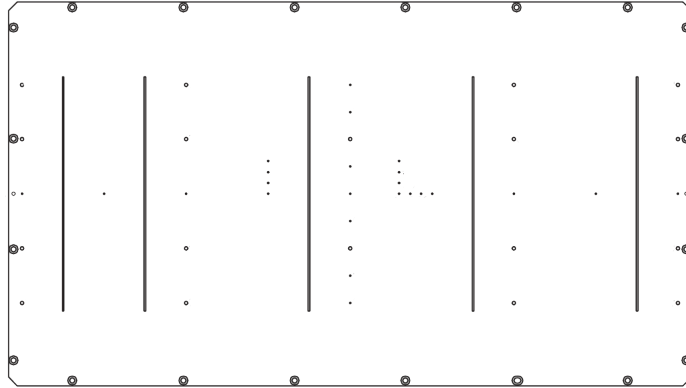
Figure 6.1 Diagram depicting hole and slit pattern in 24.603"x13.835"x0.250" CRDC masks

6.1 Calibrations

6.1.1 S800 Calibrations

As described in Section 5.2.1, the data coming from the S800 is from the detector suite in the focal plane of the spectrograph. The goal of using the S800 spectrograph is to reconstruct the excitation energy and scattering angle at the target position by passing the reacted beam through the S800 focal plane. Timing information comes from the E1 scintillator at the end of the focal plane, and comes from the internal clock in the data acquisition system, which is already calibrated as 100 ps per channel in the time to digital converter for the scintillator photo-multiplier tubes. The particle identification uses the timing information and energy loss through the ionization chamber. A description of the particle identification is in Section 6.2. To reconstruct the excitation energy and scattering angle of the reaction as described in Section 5.2.1.4, the tracking information from the Cathode Readout Drift Counters (CRDCs) is necessary to relate the detector signals to the projectile position in space.

80
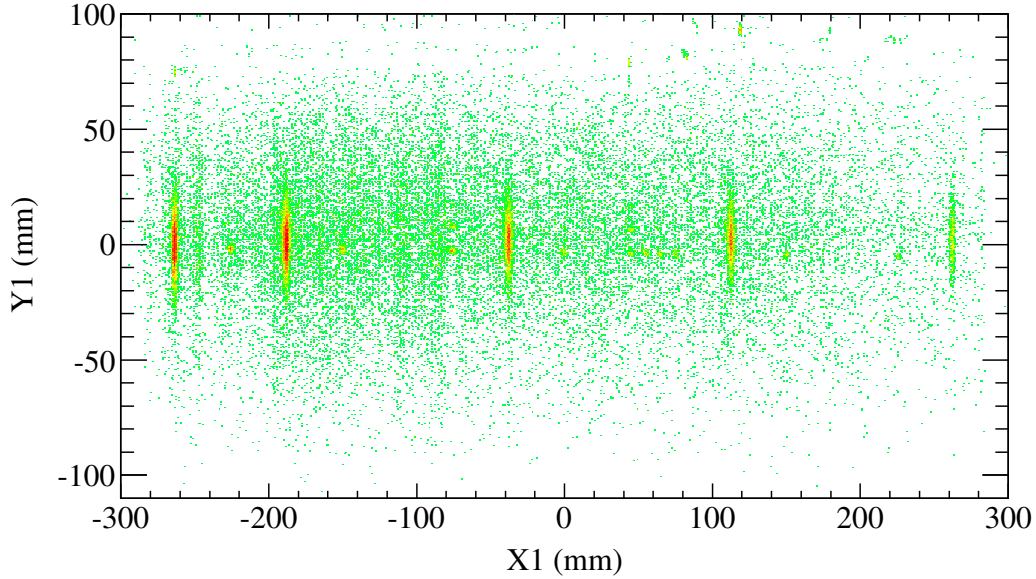
Figure 6.2 Sample spectrum of CRDC1. Calibration is complete in spectrum.

The position calibration of the CRDC is performed by remotely placing a thick tungsten plate with a precision slit and hole pattern directly up stream of the CRDC to be calibrated, see Figure 6.1. Particles that are detected in the CRDC are those that have passed through a hole in the tungsten plate, and the CRDC spectrum is then an impression of the slit and hole pattern illuminated as shown in Figure 6.2.

The calibration process involves fitting the mask data with first-order polynomials, relating the known mask hole positions (in mm) to the channel number from the data, where the units are $pads$ in the x-direction and ns in the y-direction:

$$x_{1,2}(mm) = m_{1,2}(mm/pad) \times x_{1,2}(pad) + b_{1,2}(mm) \tag{6.1}$$

$$y_{1,2}(mm) = n_{1,2}(mm/ns) \times y_{1,2}(ns) + c_{1,2}(mm). \tag{6.2}$$

Each CRDC was calibrated separately. The slope in the x-direction ($m_{1,2}$) is determined

from the charge induced on cathode, and is fixed by the segmentation of the cathode pads at 2.54 mm/pad. The slope in the y-direction ($n_{1,2}$) is determined from the drift velocity of the electrons to the anode wire. The offsets in both directions ($b_{1,2}, c_{1,2}$) are set such that the corner of the "L" shape in the mask shown in Figure 6.1 is at 0 mm. The results of the mask calibration are listed in Table 6.1.

The slope in the y-direction, not being defined with a fixed geometry as the other parameters are, is subject to the most variability. The drift velocity of the electrons in the CRDC is a dependent upon the gas composition and pressure, as well as other experimental parameters that can vary minorly throughout the experiment. It was noted that the measured y-position of the ^{10}B ejectiles drifted smoothly as a function of run number, indicating the the calibration was also changing smoothly as a function of run number. By observing the channel in which the centroid of the ejectile's y-distribution appears, and comparing this to the channel in which the centroid of the ejectile's y-distribution appears directly following calibration, the slope can be corrected for the specific run number as

$$n_{corrected}(mm/ns) = n_{measured}(mm/ns) \times \frac{y_{reference}(channel)}{y_{observed}(channel)} \qquad (6.3)$$

where $n_{corrected}$ is the corrected drift velocity, $n_{measured}$ is the original drift velocity as determined in the mask calibration, $y_{reference}$ is the position of the ejectile directly following the original mask calibration, and $y_{observed}$ is the position of the ejectile for the run of interest. The result of the correction is plotted in Figure 6.3. The most prominent fluctuation in the drift velocity is near run number 200. This corresponds to a spread in the channel (Equation 6.3) centroid of about channel 60, but the full width at half maximum of the $y_{observed}$ signal is channel 92.1. The smooth change in the drift velocity was fit with a

m_1	b_1	m_2	b_2	n_1	c_1	n_2	c_2
2.54	-281.737	2.54	-279.867	-0.074	-107.098	0.072	105.534

Table 6.1 Mask calibration parameter values obtained from CRDC mask measurement fitting.
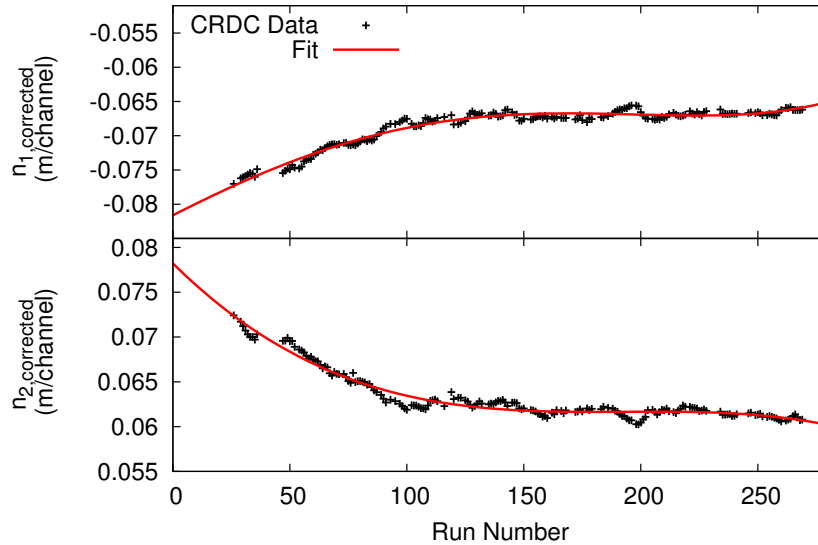
Figure 6.3 Polynomial fit of CRDC TAC data to track changes in electron drift velocity in the CRDC fill gas.

fourth-order polynomial to account for the smaller fluctuations observed in the changes to the drift velocity. Fortunately, there were no long periods without beam in the experiment, so each hour long run number can be used for the fit since it correlates well with time. The most prominent fluctuation near run number 200 is a small percentage of the total data, and is averaged out by the fitting. A mask measurement taken half-way through the experimental run confirmed the calibration to be consistent with the extrapolated measurement.

The ray tracing described in Section 5.2.1.4, used to determine the target position tracking parameters, depends upon the focal plane positions and and angles in the dispersive and non-dispersive directions. The focal plane tracking parameters are defined as

$$xfp = x_1 \tag{6.4}$$

$$yfp = y_1 \tag{6.5}$$

$$afp = ATan\left[(x_1 - x_2)/z_{sep}\right] \tag{6.6}$$

$$bfp = ATan\left[(y_1 - y_2)/z_{sep}\right] \tag{6.7}$$

where $xfp(yfp)$ and $afp(bfp)$ are the (non-)dispersive positions and angles, respectively, and $z_{sep} = 1073 \ mm$ is the distance between the two CRDCs. The parameters from Equations 6.4-6.7 are used as input into Equation 5.22 to produce the target position tracking parameters.

6.1.2 GRETINA Calibrations

6.1.2.1 Source Calibrations

Calibration of the absolute energy and efficiency of the GRETINA detectors was performed using four gamma sources placed at the target position of the S800: ^{56}Co, ^{60}Co, ^{226}Ra, and ^{152}Eu. Since the GRETINA detection system was delivered to this experimental study in a precalibrated state, source measurements were taken at the beginng and end of the experimental run to confirm the accuracy of the calibration.

Data were taken with the sources, and the spectra were fit with Lorentzians on top of a linear background in the region of the peak. Lorentzians are fit to the gamma peak since the signal is of Lorentzian shape. The centroid of the Lorentzian represents the observed energy of the gamma ray from the source. All reference energies used in this comparison are listed

Source	γ transitions used in calibration (keV)							
^{56}Co	846.8	1037.9	1175.1	1238.3	1360.2	1771.4	2015.2	2034.8
	2598.5	3202.0	3253.4	3273.0	3451.2	3548.3		
^{60}Co	1173.2	1332.5						
^{152}Eu*	121.8	244.7	344.3	411.1	444.0	778.9	867.4	964.1
	1112.1	1213.0	1299.2	1408.0				
^{226}Ra	186.2	242.0	295.2	351.9	609.3	768.4	934.1	1120.3
	1238.1	1377.7	1509.2	1729.6	1764.5	1847.4	2118.5	2204.1
	2447.7							

* source used for efficiency

Table 6.2 Reference energies for verification of gamma ray energy calibration and efficiency.

in Table 6.2. As shown in Figure 6.4, the observed energies agree well with the known data, verifying the energy calibration of the detector system.

To verify the efficiency, the ^{152}Eu source was used since it has well known emission probabilities for the gamma rays and the activity of the source has been measured. The efficiency is defined as

$$\epsilon(\%) = \frac{N_\gamma}{A \times t \times \epsilon_{emm}} \times 100 \qquad (6.8)$$

where ϵ is the measured efficiency in percent, N_γ is the number of counts in the photo-peak, A is the activity of the source, t is the duration of the calibration run adjusted for deadtime in the data acquisition system, and ϵ_{emm} is the emission probability of the photopeak. The absolute activity of the ^{152}Eu source was measured to be 8.46 μCi on May 1, 1978, and with a well-known half-life of 13.537±0.006 years, the current absolute activity was calculated. The results of the efficiency measurement are summarized in Figure 6.5. The red data points are those data points that were measured at the end of the experimental run, and the black data points are the known efficiencies of the detector system. The data taken verifies that the observed efficiency is consistent with the reported values. To estimate the efficiency of
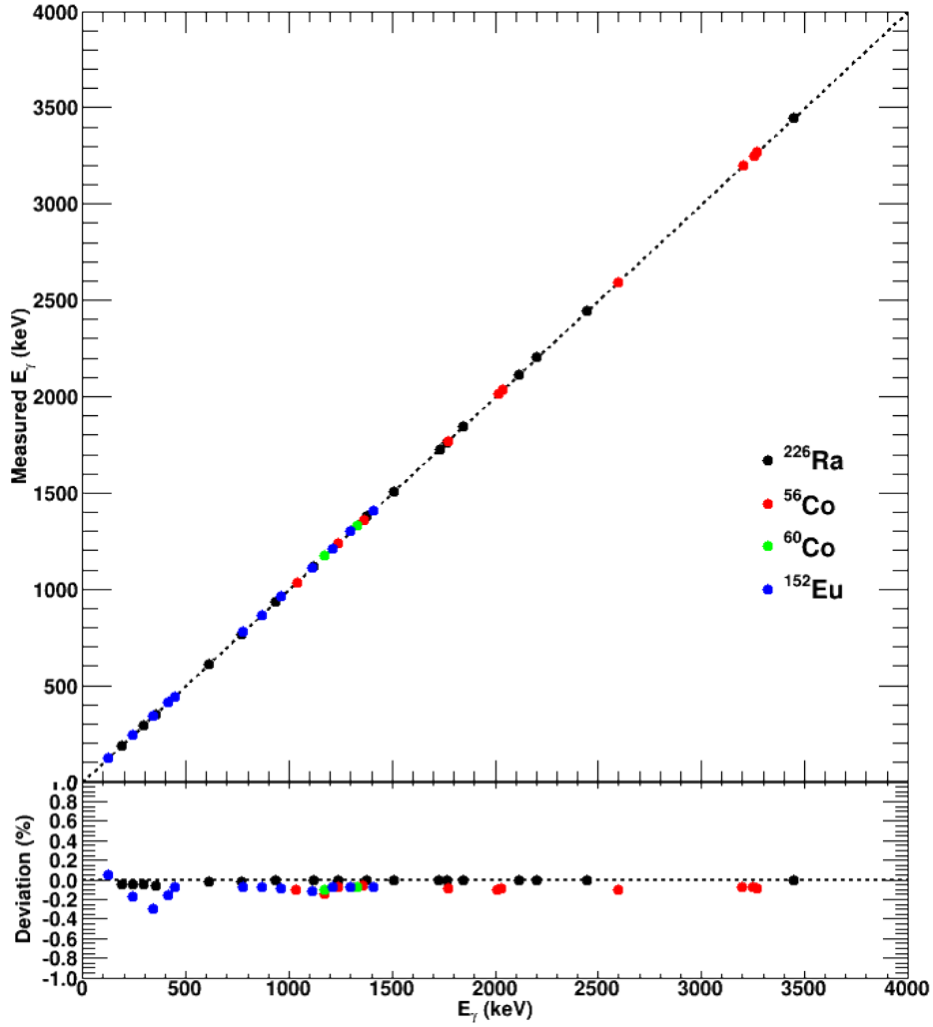
Figure 6.4 Comparison of known and measured peak energies for gamma sources ^{56}Co, ^{60}Co, ^{226}Ra, and ^{152}Eu.

the gamma rays observed from the de-excitation of the ^{10}B, the reported data was fit with

the power-law function

$$\epsilon(E_\gamma) = 595.66 \times \text{Exp}[-0.675 \times \text{Log}[E_\gamma + 148.9]] \qquad (6.9)$$

where the fit is shown as the dashed blue line in Figure 6.5. Based upon this fit, the estimated

efficiency for the 1022 keV transition from ^{10}B was $5.06\% \pm 0.05\%$.
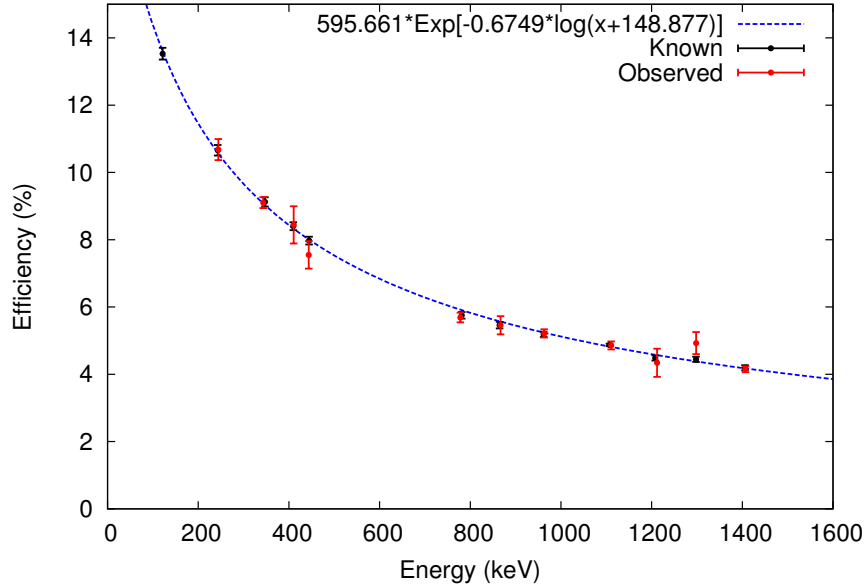
Figure 6.5 GRETINA efficiency as measured by ^{152}Eu. Observed values are from data taken during experimental run for comparison with reported efficiencies. The line is fit to the known data.

6.1.2.2 In-Flight Corrections

In this experiment, the ^{10}B ejectiles from the reaction ^{28}Si(^{10}Be,^{10}B*) are traveling at about 43% of the speed of light when de-excitation occurs. Due to the velocity of the particle, the energy observed by the detector in the lab frame is Doppler shifted such that at forward (backward) angles, the measured energies were higher (lower) than in the projectile frame. It is necessary to know the energy in the projectile frame, as this is the energy that characterizes the state of the projectiles state. To do this, the observed energies are Doppler-corrected using Equation 5.27.

To properly perform the Doppler-correction, the direction of the ejectile must be taken into account. If the beam were to travel along the z-axis, no correction would be necessary since the beam would be perfectly perpendicular to the target. However, if there is a slight deviation from perpendicularity of the beam on the target, as can be seen in the left panel

of Figure 6.6, a correlation exists between the azimuthal scattering angle and the Doppler-corrected beam energy. To correct for this, a vector is defined from the GRETINA position data for the scattering angle (θ_{GR}, ϕ_{GR}) of the gamma-ray and from the ray traced scattering angles $(\theta_{S800}, \phi_{S800})$ from the S800 tracking. The term $\text{Cos}(\theta)$ of the Doppler-correction, Equation 5.27, is calculated by taking the scalar product of the two vectors:

$$\text{Cos}(\theta) = \text{Sin}(\theta_{GR}) \times \text{Sin}(\theta_{S800}) \times$$

$$\left(\text{Sin}(\phi_{GR}) \times \text{Sin}(\phi_{S800}) + \text{Cos}(\phi_{GR}) \times \text{Cos}(\phi_{S800}) + \text{Cos}(\theta_{GR}) \times \text{Cos}(\theta_{S800})\right).$$

$$(6.10)$$

The result of this correction is shown in the right panel of Figure 6.6. The correction has to be performed on an event-by-event basis, and for each crystal. The results in Figure 6.6 are for one of the 28 crystals in GRETINA. Before correction, the FWHM resolution of the 1022 keV peak from ^{10}B was 36.2 keV, and following correction, the observed resolution became 20.2 keV, a 44% increase in resolution.

As shown in Figure 6.7, the Doppler-correction of the beam shifted throughout the experiment. Investigation of this effect showed that the displacement coincided with target changes. Figure 6.8 shows the effect of the assumed target position for the 1022 keV Doppler-corrected gamma-ray, when shifting the assumed target position upstream or downstream from the S800 target position. Since the Doppler-corrected energy is proportional to $\text{Cos}(\theta)$ as shown in Equation 5.27, a shift upstream, or in the negative z-direction, causes the scattering angle of the gamma-ray to appear smaller, and increases the Doppler-corrected energy. Likewise, a shift down stream, or in the positive z-direction, causes the Doppler-corrected energy to
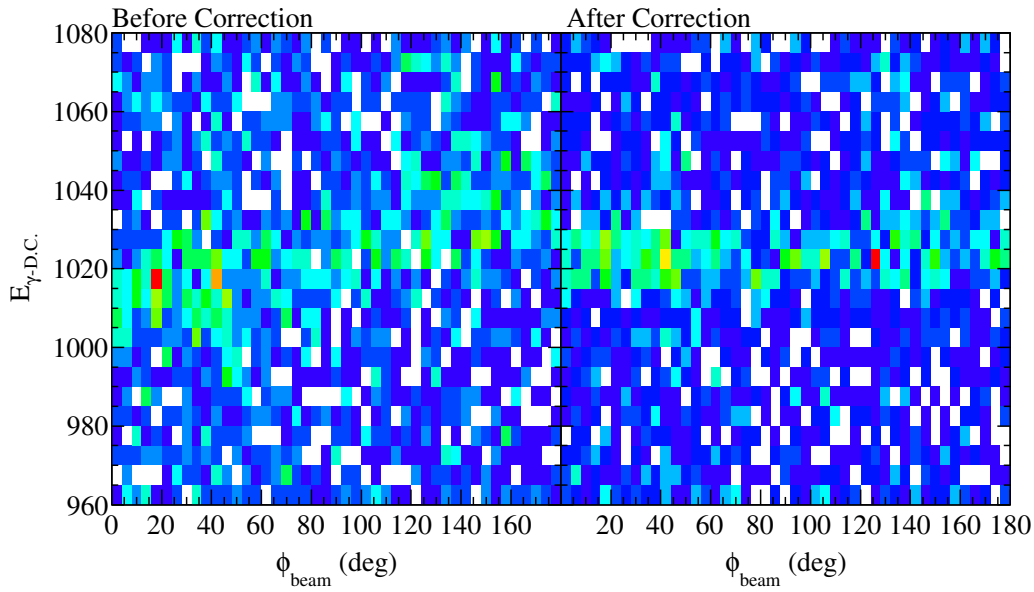
Figure 6.6 Correction of Doppler corrected gamma-ray energy for scattering angle of particle. Results of one crystal is shown.

appear lower.

In the analysis software, the assumed target position was shifted up and down stream in 0.5 cm steps in a range of 2 cm. For each target placement, the Doppler-corrected peaks were fit with Lorentzians plus a linear background to extract the position and width. The correlation between Doppler-corrected energy and assumed target position was found to be linear, and was used to account for the shift in target position. The corrected target positions are listed in Table 6.3. The position correction for the Silicon data set is systematically larger than the correction for the Carbon because the 7.6 cm in diameter Silicon disc was held at $10°$ off from perpendicular to the beam direction. Figure 6.9 shows the corrected gamma-spectrum for the 1022 keV Doppler-corrected gamma-ray for the target holder position.
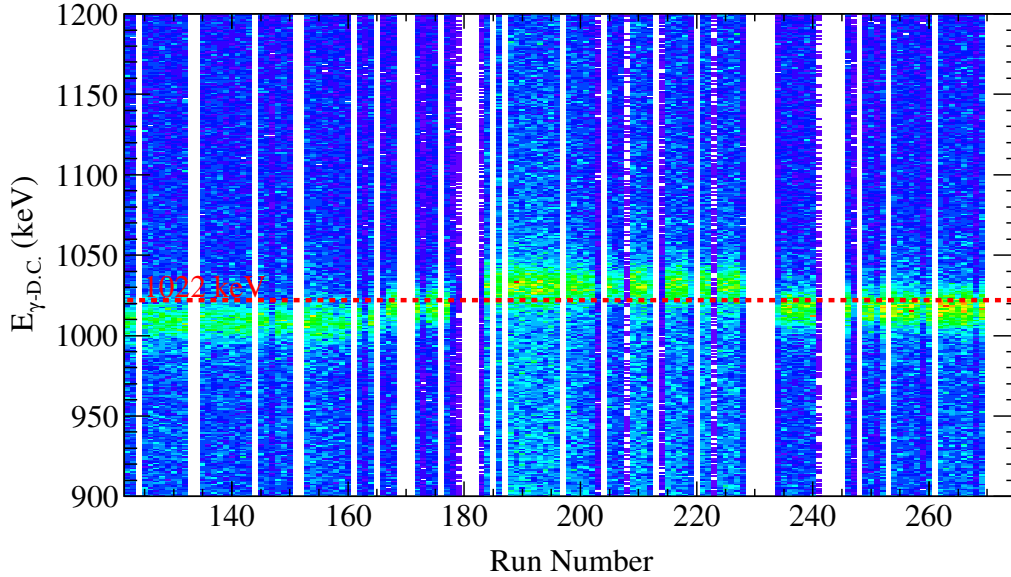
Figure 6.7 Observed energy shift of Doppler corrected 1022 keV gamma-ray due to target placement inaccuracies. Shifts above and below known energy are a result of the target placement upstream or downstream, respectively, of the assumed target location.

Data Set	Runs	Position Correction (mm)
Silicon	122-166	-6.4371
Carbon	167-177	-1.8155
Silicon	178-228	4.6618
Carbon	234-269	-2.3255

Table 6.3 Reference energies for verification of gamma ray energy calibration and efficiency.

6.2 Particle Identification

The S800 spectrograph was tuned to an optimal magnetic rigidity for accepting the ^{10}B ejectiles. However, the purity of the ^{10}Be incoming beam was of 88%, with contamination due to ^{8}Li and ^{12}B which is separable in particle identification. The ^{nat}Si target consisted of 92.2% ^{28}Si, 4.7% ^{29}Si, and 3.1% ^{30}Si. Since the target was self-supporting, reactions in addition to the reaction of interest, ^{28}Si(^{10}Be,^{10}B)^{28}Al, were a result of reactions in any combination of the contaminants. Fortunately, with the spectrograph tuned for the ^{10}B ejectiles, we exploited the energy loss, timing , position, and angle measurements from
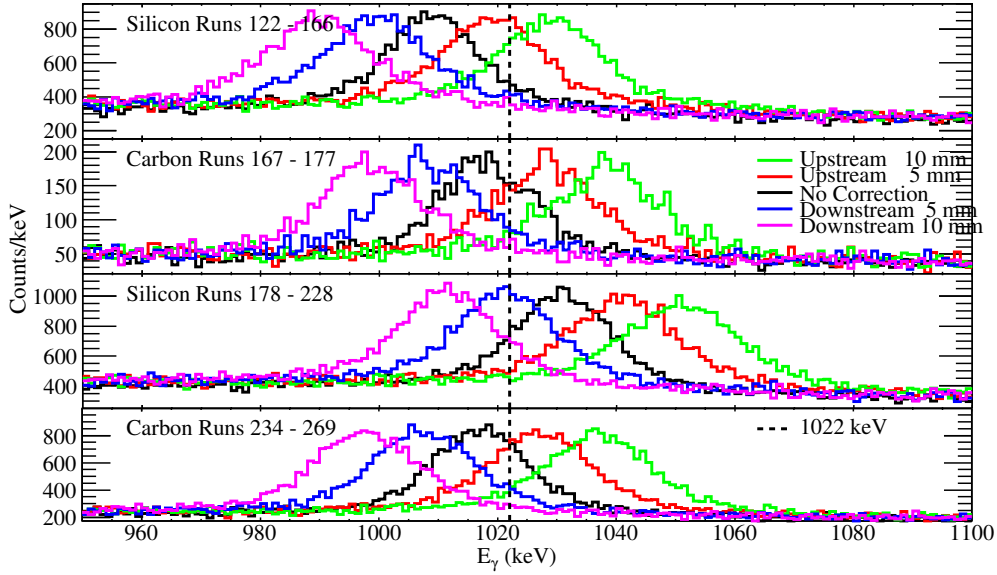
Figure 6.8 Effect of target placement on Doppler-correction of 1022 keV gamma-ray.

the focal plane to isolate the ^{10}B particles of interest from other reaction products and contaminants.

To identify the particle of interest, the $\Delta E - ToF$ method was implemented. As mentioned previously (see Section 5.1.2), the energy loss of an ion through a medium is proportional to its proton number squared (Z^2). In this way, an energy loss measurement determines the element passing through the medium, without directly relating which isotope it is. The time-of-flight (ToF) measurement analyzes the velocity of the particle, which in turn relates back to the momentum to charge ratio of the particle as detailed in Equation 5.2. So, given a constant magnetic rigidity ($B\rho$) and a known flight path length (L), a ToF measurement will relate the mass to charge of the particle as:

$$B\rho = \gamma\frac{mv}{q} \rightarrow \frac{1}{v} = \text{const.} \times \frac{m}{q} = \frac{tof}{L}.\tag{6.11}$$

91
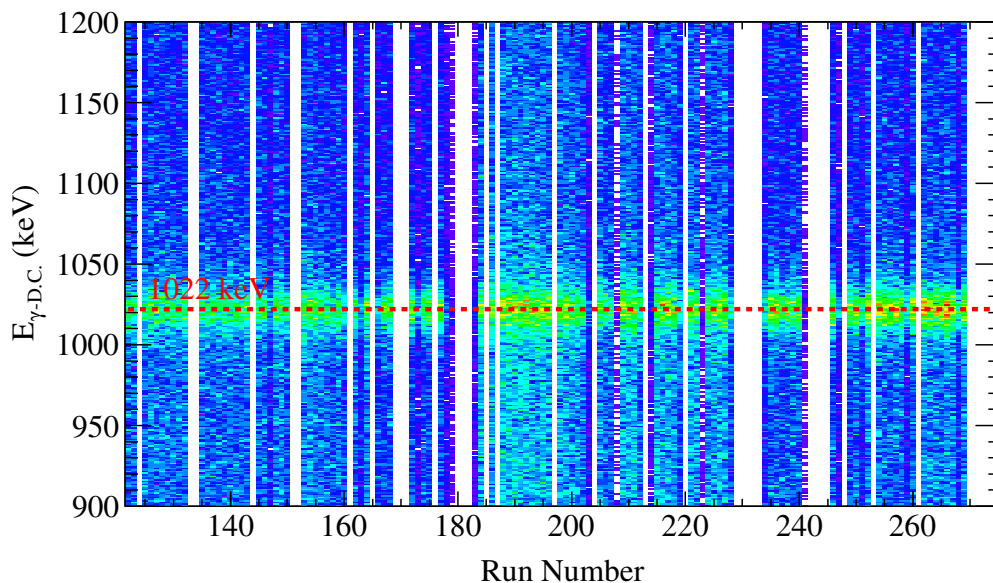
Figure 6.9 Target holder position corrected spectrum for the 1022 keV Doppler-corrected gamma-ray.

Therefore a measurement of $\Delta E - ToF$ will isolate the isotope of interest.

To properly implement the ToF measurement, the trajectory of the particles through the beam line must be taken in to account. As shown in Figure 6.10, there is a correlation between the ToF of the ^{10}B and the trajectory in the dispersive direction. By correcting first for the linear dependence of the dispersive angle, then the dispersive position, the separation of the different species in the beam is improved, and the final particle identification (PAID) spectrum is shown in Figure 6.11, where an arbitrary offset in time has been implemented to center the ^{10}B at 0 ns.

Figure 6.11 indicates the position of the ^{10}B projectile of interest. The gate applied to the PID is an ellipse around with the center and radius in $T.O.F.$ and ΔE shown in Table 6.4. The position and radii were determined from Gaussian fits to the ^{10}B signals.
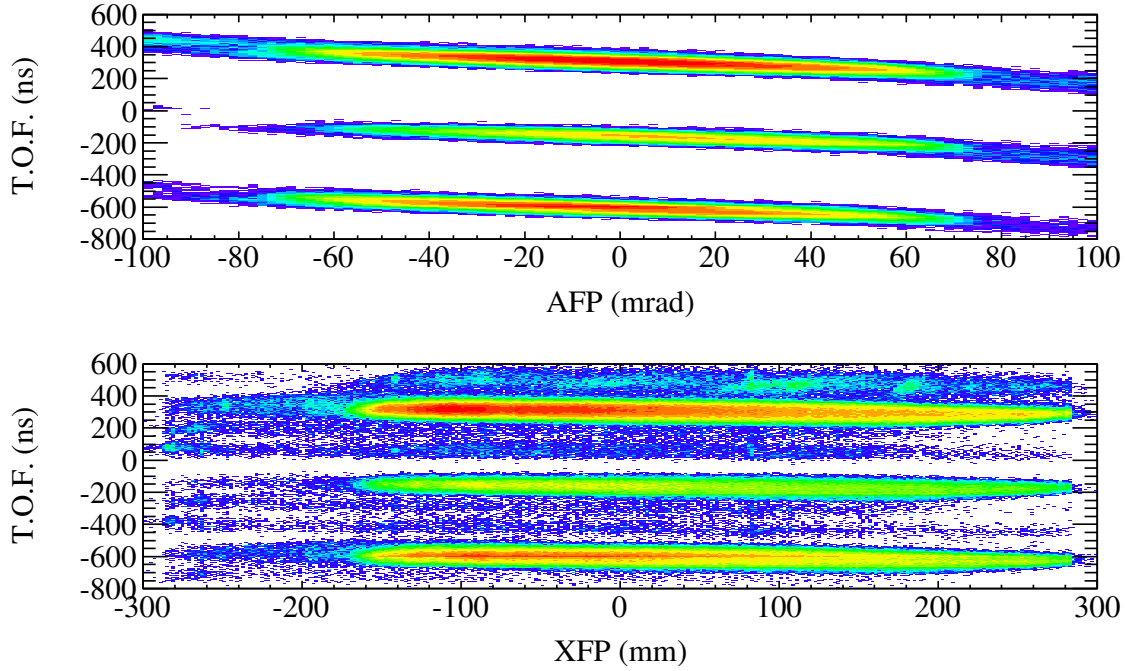
Figure 6.10 Correlation between ToF and the dispersive direction coordinates afp, xfp

Signal	Center	Radius
$T.O.F.$	0.428 ns	4.68 ns
ΔE	126.9 a.u.	46.4 a.u.

Table 6.4 Definition of elliptical gate on ^{10}B in PID.

6.3 Excitation Energy Reconstruction

The excitation energy of the ^{28}Al residual of the ^{28}Si(^{10}Be,^{10}B) reaction is reconstructed in a 'missing mass' calculation by relating the reconstructed target position energies (dta) and angles (ata, bta) of the ^{10}B ejectile to the mass missing in the system. In the following derivation, the speed of light has been set to 1.

Consider a binary reaction which is denoted as $A(a, b)B$, where $A = ^{28}$Si, $B = ^{28}$Al, $a = ^{10}$Be, and $b = ^{10}$B for this study. As shown in Figure 6.12, for a particle participating in the interaction, m is the mass, p is the momentum, T is the kinetic energy, and θ is the scattering angle, where the subscript denotes the particle. The conservation of energy and
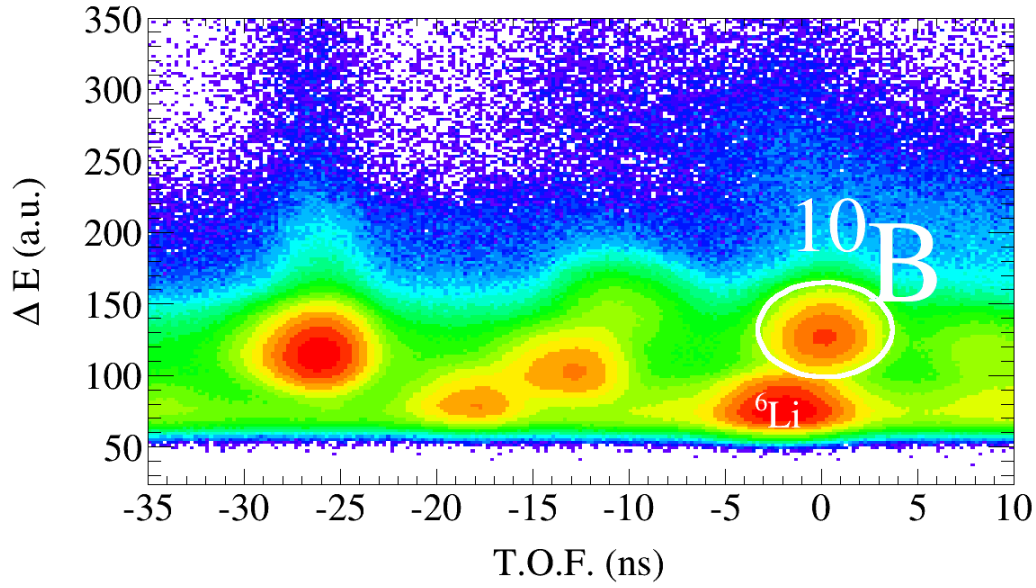
Figure 6.11 PID indicating ^{10}B particles. Figure includes corrections to the time-of-flight spectrum.

linear momentum are expressed as

$$(m(^{10}\text{Be}) + T(^{10}\text{Be})) + m(^{28}\text{Si}) = (m^*(^{10}\text{B}) + T(^{10}\text{B})) + (m^*(^{28}\text{Al}) + T(^{28}\text{Al})) \quad (6.12)$$

$$\mathbf{p}(^{10}\text{Be}) = \mathbf{p}(^{10}\text{B}) + \mathbf{p}(^{10}Al) \quad (6.13)$$

where the ejectile and residual are left in excited states such that

$$m^*(^{28}\text{Al}) = m(^{28}\text{Al}) + E_X(^{28}\text{Al}) \quad (6.14)$$

$$m^*(^{10}\text{B}) = m(^{10}\text{B}) + E_X(^{10}\text{B}) \quad (6.15)$$

where the $*$ indicates an excited nucleus.
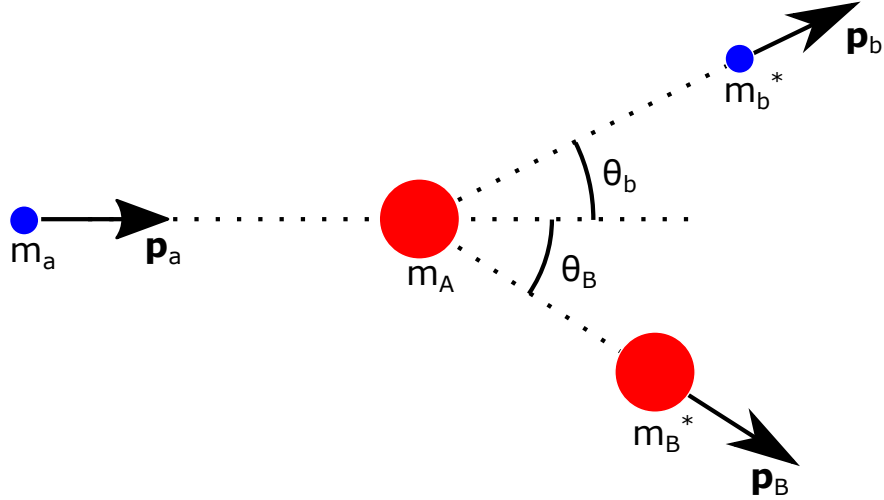
Figure 6.12 Definitions of the kinematic variables in the laboratory frame.

Using the conservation of energy from Equation 6.12,

$$m^*(^{28}\text{Al}) + T(^{28}\text{Al}) = (m(^{10}\text{Be}) + T(^{10}\text{Be})) + m(^{28}\text{Si}) - (m^*(^{10}\text{B}) + T(^{10}\text{B})). \quad (6.16)$$

Rewriting the left-hand side of Equation 6.16, and using Equation 6.13,

$$m^*(^{28}\text{Al}) + T(^{28}\text{Al}) = \sqrt{m^{*2}(^{28}\text{Al}) + \mathbf{p}^2(^{28}\text{Al})} \quad (6.17)$$

$$= \sqrt{m^{*2}(^{28}\text{Al}) + (\mathbf{p}(^{10}\text{Be}) - \mathbf{p}(^{10}\text{B}))^2}. \quad (6.18)$$

In the lab frame, ^{28}Si is at rest and the kinetic energy is carried by the ^{10}Be, the excitation energy of the ^{28}Al can be inferred from the missing mass of the observed ^{10}B. In Equation 6.18, the missing energy and momentum of the ^{10}B are

$$E_{missing} = (m(^{10}\text{Be}) + T(^{10}\text{Be})) + m(^{28}\text{Si}) - (m^*(^{10}\text{B}) + T(^{10}\text{B})) \text{ and} \qquad (6.19)$$

$$p_{missing} = \mathbf{p}(^{10}\text{Be}) - \mathbf{p}(^{10}\text{B}). \qquad (6.20)$$

Employing the energy relation $E^2 = m^2 + p^2$, the missing mass is

$$m_{missing} = \sqrt{E_{missing}^2 - \mathbf{p}_{missing}^2}. \qquad (6.21)$$

The excitation energy simplifies to

$$E_X(^{28}\text{Al}) = m_{missing} - m(^{28}\text{Al}). \qquad (6.22)$$

In this derivation, the necessary ingredients of the excitation energy calculation are the masses of each participating nucleus, and the kinetic energy and momenta of ^{10}Be and ^{10}B. The following five bullet points address each of the terms:

- The masses were obtained from a nuclear data database [88].

- The kinetic energy of the incident ^{10}Be was inferred from the rigidity setting of the analysis line by the square of Equation 5.2,

$$(B\rho)^2 = \frac{m^2 v^2}{Q^2} = 2\frac{mE}{Q^2}. \qquad (6.23)$$

Since $E = p^2/2m$

$$p^2 = 2mE. \qquad (6.24)$$

Dividing and multiplying by the charge squared, and using the relation $E^2 = m^2 + p^2$,

$$p^2 = \left(2\frac{mE}{Q^2}\right) Q^2 = (B\rho)^2 Q^2 = E^2 - m^2. \tag{6.25}$$

Solving for the energy and using the relation $E = m + T$,

$$E = \sqrt{(B\rho Q)^2 + m^2} = m + T. \tag{6.26}$$

Therefore, the total kinetic energy of ^{10}Be is

$$T(^{10}\text{Be}) = \sqrt{(B\rho Q)^2 + m^2(^{10}\text{Be})} - m(^{10}\text{Be}). \tag{6.27}$$

- The kinetic energy of the ^{10}B was calculated on an event-by-event basis using the energy of a central ray through the spectrograph (T_0), calculated as above using Equation 6.27, and the ray traced fractional energy dta as

$$T(^{10}\text{B}) = T_0(1 + dta), \tag{6.28}$$

where $dta = \frac{T(^{10}B) - T_0}{T_0}$

- The momentum of ^{10}Be defines the beam axis along the z-direction as

$$p_x(^{10}\text{Be}) = p_y(^{10}\text{Be}) = 0 \tag{6.29}$$

$$p_z(^{10}\text{Be}) = p(^{10}\text{Be}). \tag{6.30}$$

The total momentum is determined by using the relation $E = m + T$ in the relation $E^2 = p^2 + m^2$ and solving for the momentum, such that

$$p(^{10}\text{Be}) = \sqrt{T^2(^{10}\text{Be}) + 2T(^{10}\text{Be})m(^{10}\text{Be})}. \tag{6.31}$$

- The momentum of the ^{10}B is defined as

$$p_x(^{10}\text{B}) = p(^{10}\text{B}) \times \text{Sin } ata \tag{6.32}$$

$$p_y(^{10}\text{B}) = p(^{10}\text{B}) \times \text{Sin } bta \tag{6.33}$$

$$p_z(^{10}\text{B}) = p(^{10}\text{B}) \times \text{Cos } \theta_{ta} \tag{6.34}$$

where ata, bta, and θ_{ta} are the dispersive, non-dispersive, and overall scattering angle, respectively, and $p(^{10}\text{B})$ is the total momentum calculated on an event-by-event basis using the momentum of a central ray through the spectrograph (p_0), calculated using Equation 6.31 for ^{10}B, and the ray traced fractional momentum dta_p.

dta_p is calculated from its definition

$$dta_p = \frac{p - p_0}{p_0} \tag{6.35}$$

and solving for p and using Equation 6.31, adapted for ^{10}B,

$$p = p_0(1 + dta_p) = \sqrt{T^2(^{10}\text{B}) + 2m(^{10}\text{B})T(^{10}\text{B})}. \tag{6.36}$$

Solving back for dta_p,

$$dta_p = \frac{\sqrt{T^2(^{10}\text{B}) + 2m(^{10}\text{B})T(^{10}\text{B})}}{p_0} - 1 \qquad (6.37)$$

where $T(^{10}\text{B})$ is related from Equation 6.28.

The scattering angle of the reaction in the laboratory frame is calculated from the dispersive and non-dispersive angles as

$$\theta_{ta} = \text{ATan}\sqrt{\text{Tan}(ata)^2 + \text{Tan}(bta)^2}. \qquad (6.38)$$

Correlations between the excitation energy and the scattering angle are observed in the data. The top two panels of Figure 6.13 show this correlation in the coordinates E_X, ata, and bta using the data taken with the ^{12}C target. The ^{12}C target is beneficial for observing and correcting this effect due to the strong $^{12}\text{C}(0^+, g.s.)\rightarrow^{12}\text{B}(1^+, g.s.)$ transition. The ground state peak of ^{12}B appears as a line in the excitation energy versus scattering angle data, as shown in the top panels of Figure 6.13. Correlations present in the energy and scattering angle data are corrected for by fitting a line to the peak observed.

The bottom panels of Figure 6.13 shows the effect of the correction for data taken on the ^{12}C target (bottom-left) and on the ^{28}Si target (bottom-right). Indicated on the bottom-left panel is the ground state of ^{12}B. The correction gives a slight improvement in the excitation energy resolution of the ^{12}B ground state peak. In the bottom-right panel, there are no clearly separated states in the ^{28}Si target data, and no clear improvement observed.

The ground state energy calibration for the data sets was done by fitting the ground state peak in ^{12}B (see Figure 6.13, bottom-left) with a Gaussian plus another Gaussian to

99
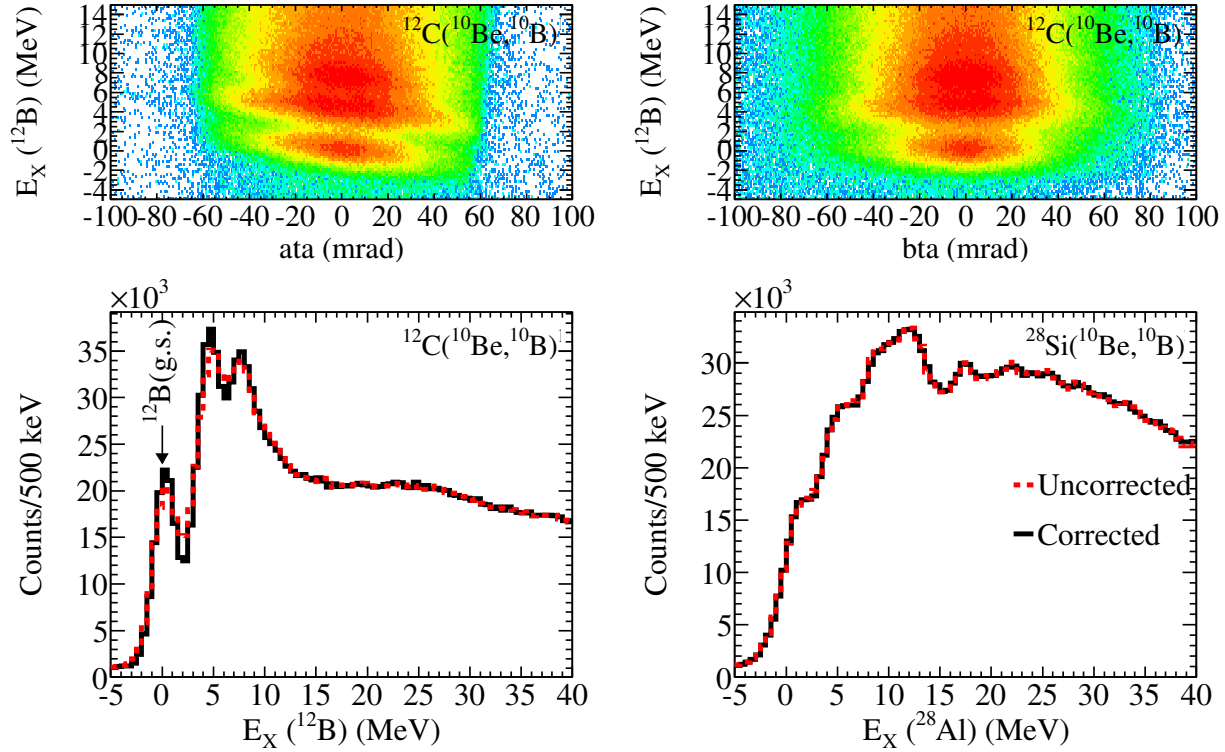
Figure 6.13 (Top) Correlation between dta and the dispersive and non-dispersive scattering angles. (Bottom, Left) Effect of correction on ^{12}C(^{10}Be,^{10}B) ^{12}B excitation energy resolution. The ^{12}C(g.s.)→^{12}B(g.s.) transition is indicated. (Bottom, Right) Effect of correction on ^{28}Si(^{10}Be,^{10}B)^{28}Al excitation energy resolution.

represent the drop in counts from 10 to 5 MeV. The fit of the ground state peak in the ^{12}C(^{10}Be,^{10}B+γ(0.718 MeV))^{12}B data found the peak to be located at 13.1 MeV, and this shift has been applied to the presented data. This shift in the energy scale can occur from the assumption that the rigidity ($B\rho$) of the beam line is correct and fixed, but the kinematic enegy of the particles varies due to reactions occuring within the target material. The energy scale of the ^{28}Al spectrum (see Figure 6.13, bottom-right) was established by an additional shift of 2.618 MeV to account for the energy loss difference of the beam through the ^{12}C and ^{28}Si targets. The energy loss through the target was calculated in Lise++ [27].

In the bottom panel of Figure 6.14, below -5 MeV, there appears to be some contamination present in the data. This is likely due to the PID gate from Section 6.2 not fully
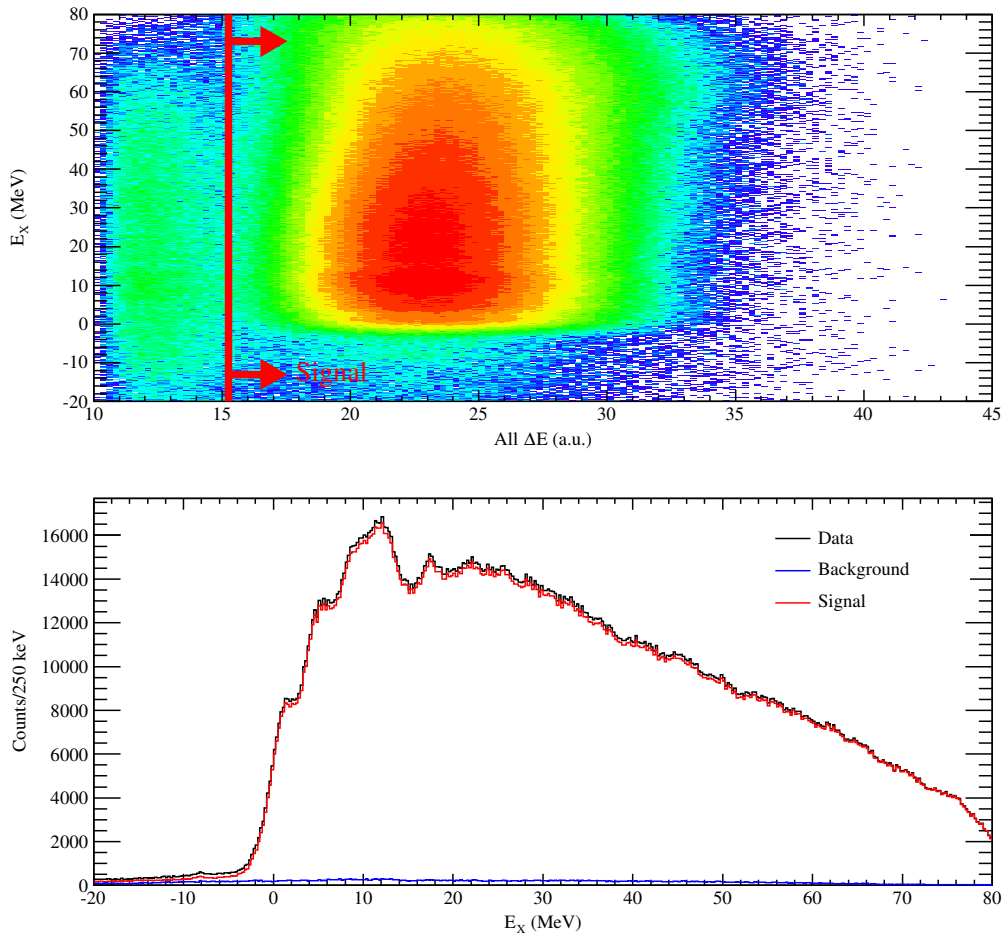
Figure 6.14 (Top) "All ΔE" as described in the text plotted as a function of ^{10}B excitation energy. A division between good events and background contamination is visible. The red line shows the "All ΔE" threshold of 15.25 in arbitrary units. (Below) Background subtracted excitation energy spectrum of ^{28}Al.

isolating the ^{10}B ejectile. Using a convolution of energy loss signals from the ion chamber and the 5 mm E1 scintillator in the focal plane of the S800, a new signal called "All ΔE" was defined as

$$\text{All } \Delta E = (\Delta E)_{I.C.} \times (\Delta E)_{Scint}/4000, \tag{6.39}$$

where 4000 was chosen to scale the units arbitrarily. The top panel of Figure 6.14 shows the excitation energy of ^{28}Al as a function of the "All ΔE" signal. To the left of the red line is a
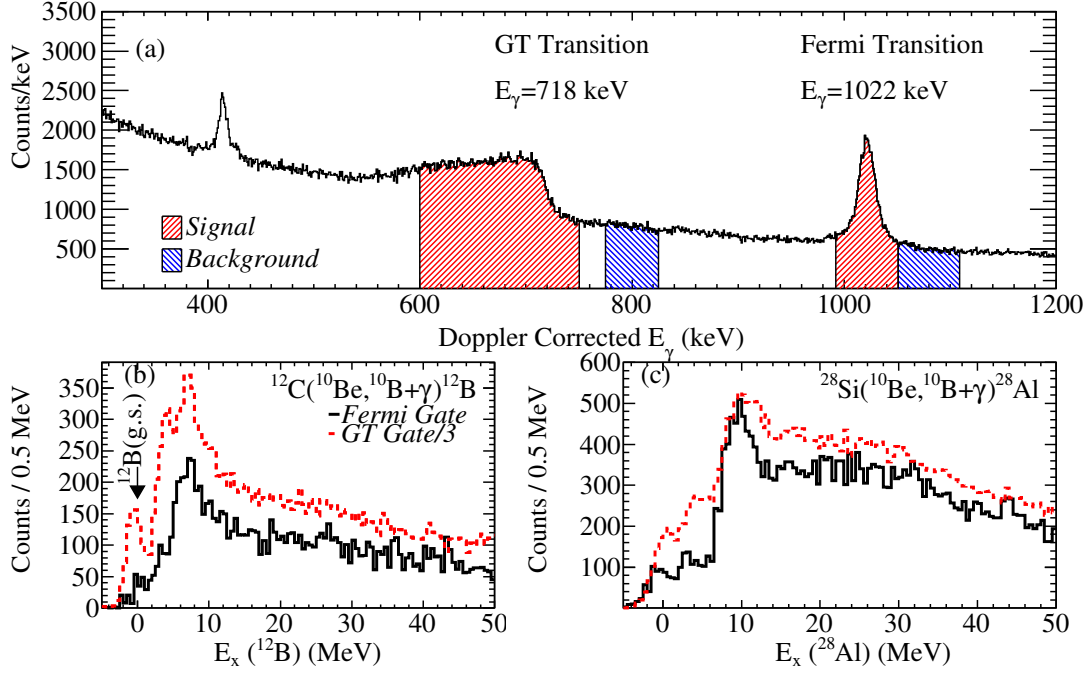
Figure 6.15 (a) Doppler-corrected gamma-ray spectrum. Indicated are the GT and F transitions, which indicate $\Delta S = 1$ and $\Delta S = 0$ reactions, respectively. Also shown is the signal, along with the side-band used for background subtraction. (b) Excitation energy spectrum of ^{12}B for the ^{12}C(^{10}Be,^{10}B+γ) reaction. Shown are background subtracted results for $\Delta S = 0$ reactions in black and $\Delta S = 1$ reactions in red. (c) Similar to (b), but for the ^{28}Al(^{10}Be,^{10}B+γ)^{28}Al reaction.

region that is identified as the contamination. To the right of the red line is the "signal" or usable data. The location of the "All ΔE" gate was determined by reversing the gate and moving the gate until no features of the ^{28}Al spectrum were observed. A location of 15.25 was determined in this definition of "All ΔE". The bottom panel of Figure 6.14 shows the result of gating out the All ΔE background.

6.4 Coincidence Data

Up until this point, all data shown has not included information from the in-flight gamma-emission of the ^{10}B ejectile. As such, the "singles" data shown includes both spin-transfer
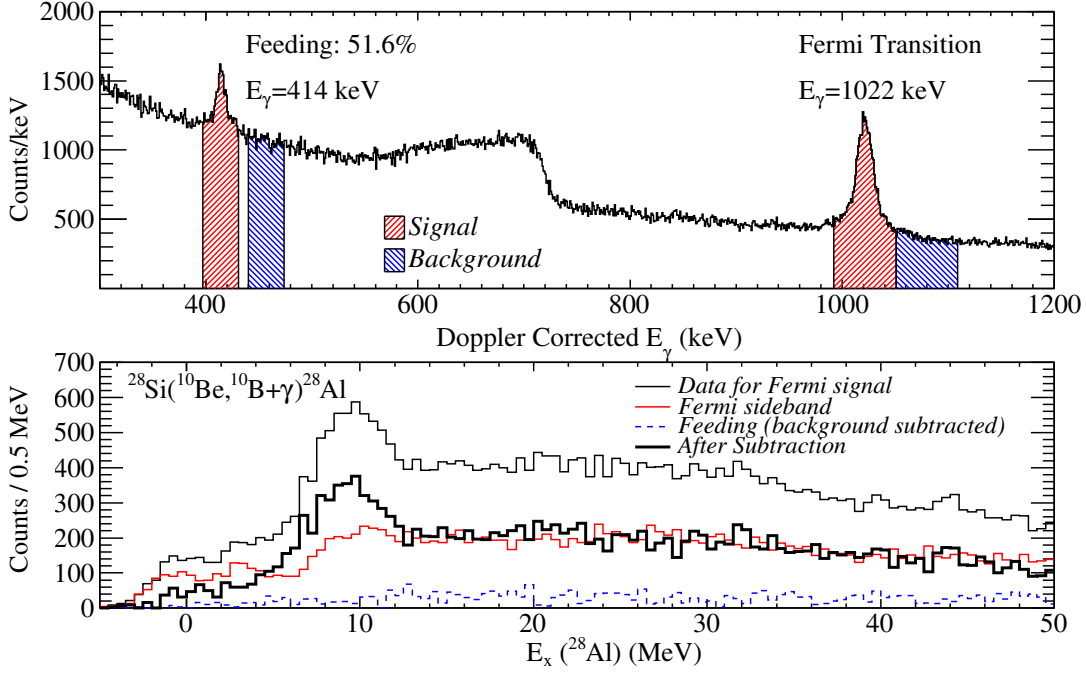
Figure 6.16 (Top) Doppler-corrected gamma-ray spectrum. Indicated are the 1022 keV Fermi transition of interest and the 414 keV GT transition that feeds into this state. Also shown is the signal, along with the side-band used for background subtraction. The gamma data in this figure is the same as in Figure 6.15, but now different regions are highlighted. (Bottom) Excitation energy spectrum of ^{28}Al for the ^{28}Al(^{10}Be,^{10}B+γ) reaction. The thick black line is the result of subtraction of background and feeding in the coincidence data.

($\Delta S = 1$) and non-spin-transfer ($\Delta S = 0$) contributions and contributions from various other excited states in ^{10}B. The "coincidence" data is the data where a ^{10}B ejectile is observed in the focal plane of the S800 along with a gamma ray in GRETINA. The top panel of Figure 6.15 shows the Doppler-corrected gamma-ray spectrum gated on ^{10}B, where the spin-transfer and non-spin-transfer tags are indicated as the 718 keV GT transition and the 1022 keV Fermi transition, respectively. The blue hatched region to the right of the signal is the side-band which is used to characterize the noise under the peak. The broad nature of the GT transition is due to the long half-life of the 718 keV in ^{10}B ($t_{1/2}$ =0.71 ns) which results in the angle for the Doppler reconstruction to be uncertain since the decay will occur $\langle z_\gamma \rangle = 14.0$ cm down stream of the S800 target; this could not be corrected for on an event-

by-event basis. Though the GT transition was not well resolved and suffered from a large background contamination due to excitations in the target and feeding from deexcitation of the 1.740 MeV state in ^{10}B, it served as a good example for showing spin-transfer reactions.

The bottom panel of Figure 6.15 compares the singles data with coincident data for spin-transfer and non-spin-transfer reactions for the ^{12}C and ^{28}Si reaction targets. Each data set gates out the "All ΔE" background (see Section 6.3), and the coincident data has the side-band background subtracted. Feeding is also taken into account for the coincident data.

Before elaborating on Figure 6.15, the feeding of the 1022 keV peak in the Doppler-corrected gamma-ray spectrum needs to be detailed. Figure 6.16 shows the results of removal of counts due to feeding. In the top panel, the 414 keV transition that feeds into the 1022 keV peak is indicated (see also Figure 2.4). Counts due to this state are corrected for the detector efficiency of the the gamma ray energies and the branching ratio of the 414 keV transition to the 1.740 MeV state (52.6%) and subtracted from the data to account for contamination from this spin-flip transition. The feeding accounted for 8% of the counts in the 1022 keV Fermi peak. The result of the feeding subtraction is shown in the bottom panel of Figure 6.16.

In the data taken on the ^{12}C target, there appear to be three structural features below 10 MeV, see Figures 6.13 and 6.15. Comparing the singles data with coincidence data in Figure 6.15(b) shows that the data is predominantly spin-transfer in nature because the dominant spin-transfer reaction ^{12}C(0^+,g.s.)$\rightarrow$^{12}B(1^+,g.s.) does not appear in the Fermi filter. This data serves as an excellent test for the ability of the probe to separate spin-transfer reactions from non-spin-transfer reactions. The ^{12}C($0^+, g.s.$)$\rightarrow$^{12}B($1^+, g.s.$) reaction is indicated in the bottom-left panel of Figure 6.15. By definition, this is a $\Delta S = 1$ transition (that can be $\Delta L = 0$ or $\Delta L = 2$ in nature, see Table 4.1), and is therefore a spin-transfer reaction. In

Resolution		
E_X	2.3	MeV
θ	0.5°	lab
θ	0.7°	c.o.m.
E_γ	4.2	keV
$E_{\gamma-DC}$ (414 keV peak)	8.4	keV
$E_{\gamma-DC}$ (1022 keV peak)	18.1	keV
Efficiencies		
$E_{\gamma-DC}$ (414 keV peak)	8.3%	
$E_{\gamma-DC}$ (1022 keV peak)	5.1%	

Table 6.5 Relevant experimental resolutions and efficiencies.

the GT gamma-ray gate data, this peak is clearly visible, whereas in the Fermi gamma-ray gate data does not have this transition, and the small peak under the location of ^{10}B ground state peak in the $\Delta S = 0$ data can be attributed to the ^{12}C(0$^+$,g.s.)→^{12}B(2$^+$,0.95 MeV) transition. As a result, the data obtained from the Fermi gamma-ray gate is observed to be CE reactions of non-spin-transfer nature.

In the data taken on the ^{28}Si target, there is some structure at low excitation energy and a broad peak near 10 MeV. As in the data taken on the ^{12}C target, the spectrum is dominated by spin-transfer reactions, but non-spin-transfer reactions were separated . Section 7.1 will separate the multipoles to determine the individual contributions to the spectra.

6.5   Experimental Resolutions

The experimental resolutions for the excitation energy (E_X) and scattering angle (θ) of the target residual ^{28}Al are listed in Table 6.5, along with the resolutions and efficiencies of the 1022 keV non-spin-transfer tag and the 414 keV feeding state (see Section 6.1.2.2). Figure 6.17 shows the manner in which the resolutions of E_X and θ were determined. The
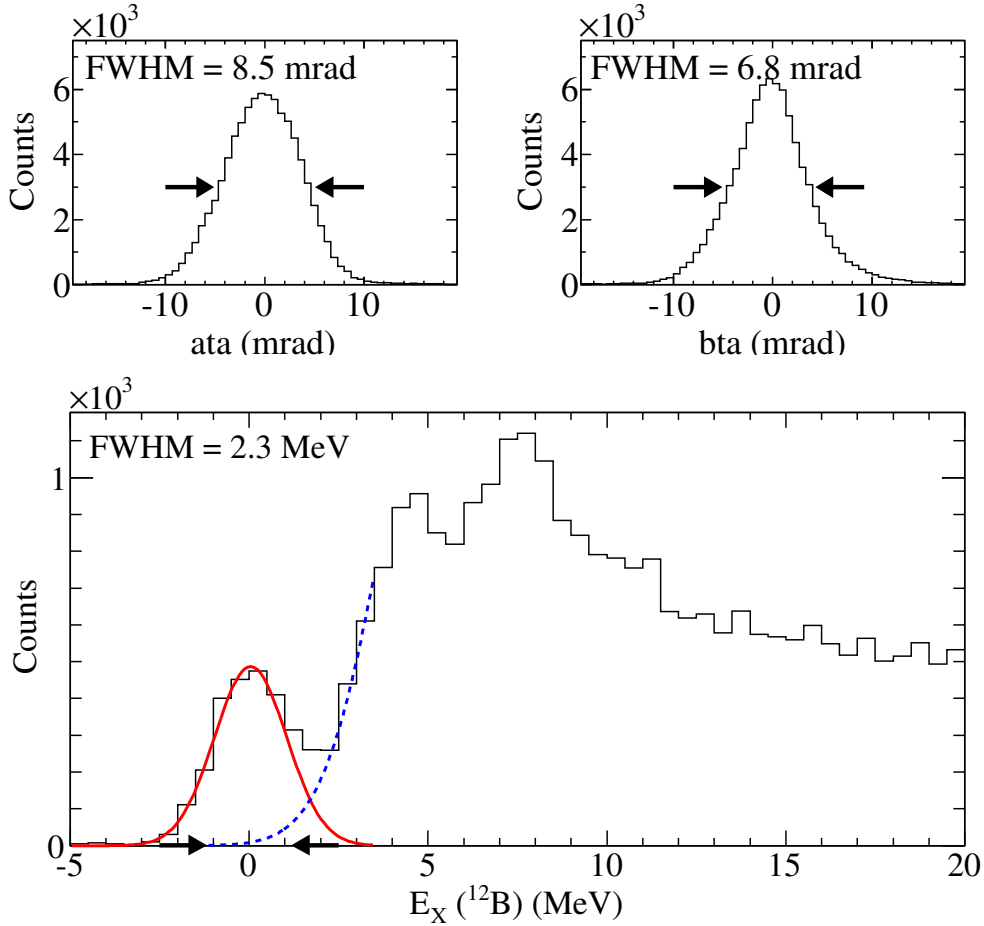
Figure 6.17 Experimental resolutions for scattering angle and excitation energy. (Top Left) Dispersive scattering angle of unreacted beam through Silicon target. (Top Right) Non-dispersive scattering angle of unreacted beam through Silicon target. (Bottom) Excitation energy spectrum for ^{12}C(^{10}Be,^{10}B+γ(0.718 MeV))^{28}Al reaction with indicated energy resolution of ^{12}B ground state.

resolutions and efficiencies of the gamma-rays were determined in Section 6.1.2.2.

In the top two panels of Figure 6.17, the full width at half-maximum (FWHM) resolution of the dispersive and non-dispersive scattering angles were determined through a measurement of the unreacted beam in the focal plane of the S800. ata was fit with a Gaussian, and bta was best represented by a Lorentzian. The propagated resolution for the total scattering angle as described by Equation 6.38 is determined to be 0.5° in the lab frame, and 0.7° in the center-of-mass (c.o.m.) frame for the ^{28}Si(^{10}Be,^{10}B)^{28}Al reaction.

In the bottom panel of Figure 6.17 the FWHM resolution of the E_X was determined by the ground state peak of ^{12}B from data taken for the ^{12}C(^{10}Be,^{10}B+γ(0.718 MeV))^{12}B reaction. As seen in the figure, there is a strong peak at 0 MeV, which is due to the ^{12}C(0^+, $g.s.$)$\rightarrow$^{12}B(1^+, $g.s.$) transition. The distribution was fit with two Gaussians, one representing the ground state peak of ^{12}B and the tail of the second represents the higher energy tail of the distribution included in the ground state peak. From this, the E_X resolution was determined to be 2.3 MeV.

In Table 6.5, the energy resolutions of the gamma rays are listed. The Doppler reconstructed peaks are broader than the non-reconstructed peaks due to Doppler broadening as described in Section 5.2.2. Doppler reconstructed resolutions and efficiencies are reported only for the 414 keV and 1022 keV gammas since the 718 keV gamma was not well resolved.

6.6   Cross-section Calculations

With the reaction spectra obtained, the last step in the data analysis before extraction of the IVGMR from the data can be realized is converting the counts in the ^{28}Al excitation energy spectrum to the differential cross-section. The bottom panel of Figure 6.16 includes the result of the background subtracted $\Delta S = 0$, $\Delta T = 1$ coincidence data. When converted to a differential cross-section spectrum, re-binned near the experimental resolution (2 MeV), and each energy bin plotted as a function of scattering angle in the c.o.m. frame ($\theta_{c.o.m.}$), the angular distributions are obtained. The scattering angle is separated into $0.5°$ bins for producing the angular distributions and were comparable to the angular resolutions. The bin sizes were determined such that there were reasonable statistics in each energy bin for producing the angular distributions. The excitation energy spectra for each angular bin is
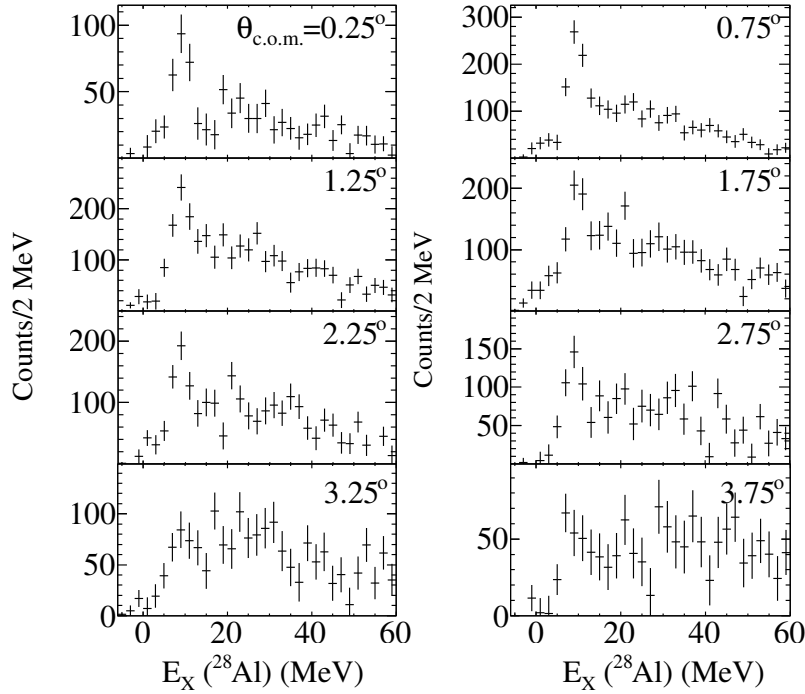
Figure 6.18 Excitation energy spectrum divided into angular bins used in cross-section calculation for the ^{28}Si(^{10}Be,^{10}B+γ(1.022 MeV))^{28}Al reaction for $\Delta S = 0$ reactions. Uncertainties represented are statistical.

shown in Figure 6.18.

The differential cross-section is defined as

$$\frac{d\sigma}{d\Omega} = \frac{N_m}{N_i N_t} \frac{1}{\epsilon_\gamma C_a \mathcal{L}} \frac{1}{d\Omega_{c.o.m.}} \tag{6.40}$$

where N_m refers to the counts in a bin after background subtraction, N_i refers to the number of incident ^{10}Be ions, N_t refers to the number of ^{28}Si atoms in the target, ϵ_γ is the efficiency of GRETINA for the coincident gamma-ray, C_a is a correction on the acceptance of the S800, and $d\Omega_{c.o.m.}$ is the opening angle subtended by the scattering angle in the c.o.m. frame. In the focal plane, the E1 scintillator provides the start signal for an event, so the efficiencies of CRDC 1, CRDC 2, and the IC relative to the E1 scintillator for the unreacted beam are
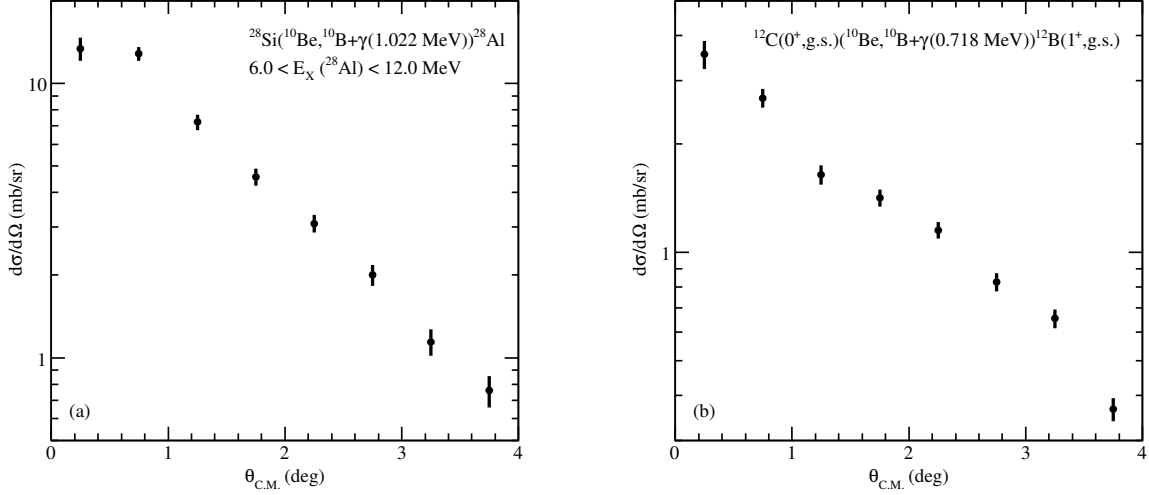
Figure 6.19 (a) Angular distribution for the ^{28}Si(^{10}Be,^{10}B+γ(1.022 MeV))^{28}Al ΔT= 1,ΔS= 0 reaction in the peak region of the excitation energy spectrum. (b) Angular distribution for the ^{12}C(0^+,g.s.)(^{10}Be,^{10}B +γ(0.718 MeV))^{12}B(1^+,g.s.) ΔT= 1,ΔS= 1 reaction.

determined to be 99.98%, 99.97%, and 98.93%, respectively. Each variable's determination is detailed below.

- N_m: The counts in each energy bin of Figure 6.18 are the integrated counts of the angular distribution associated with the energy bin. To calculate the cross-section from Equation 6.40, N_m is obtained by energy and angular bins after gamma-coincidence and background subtraction.

- N_i: The number of incident particles is determined on a run-by-run basis as described in Section 5.1.3.

- N_t: The number of atoms in the target is determined as the areal number density of the target. For the ^{nat}C target (98.88% ^{12}C) with a thickness of 56.33 mg/cm^2, $N_t = 2.80 \times 10^{21}$ cm^{-2}. For the Silicon target the crystalline structure of the ^{nat}Si target produces channels for the beam to pass through unreacted, as such the target
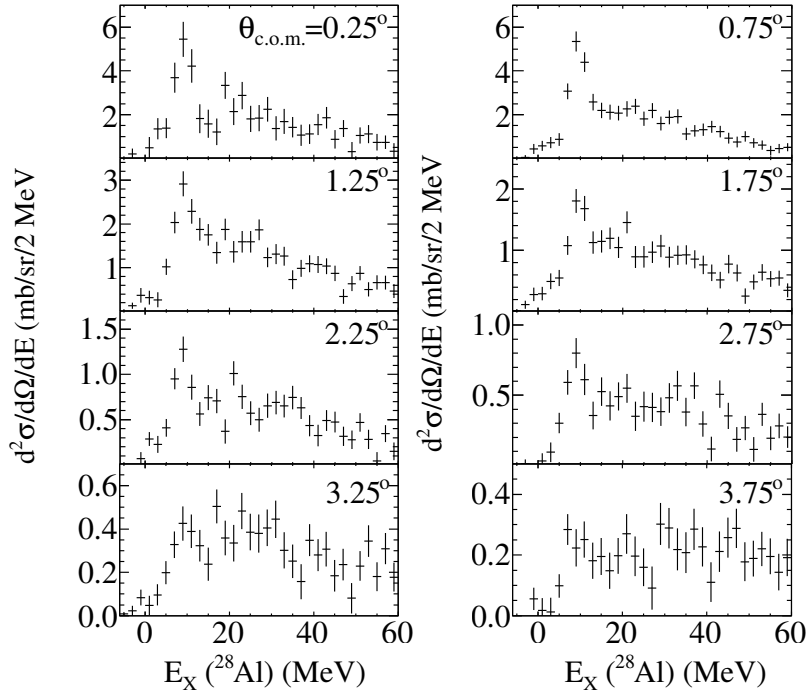
Figure 6.20 Double differential cross section for the ^{28}Si(^{10}Be,^{10}B)^{28}Al reaction, divided into angular bins. Uncertainties represented are statistical.

was placed at an angle of $10°$ with respect to the beam axis to eliminate any channeling effects. So, for a ^{nat}Si target of thickness 150 μm, the beam passed through 152.3 μm (35.36 mg/cm^2) of target material, giving $N_t = 7.02 \times 10^{21}$ cm^{-2}.

- ϵ_γ: The efficiency of the observed gamma-ray was detailed in Section 6.1.2.2, and is listed in Table 6.5.

- C_a: The correction of the acceptance is determined in a Monte-Carlo simulation, where the experimental beam conditions are taken into account. Prior to the development of the simulation, CE experiments would measure only a small portion of the laboratory scattering angle [89]. The complex function describing the S800 acceptance is dependent upon the energy (dta), scattering angle (θ), and position (yta) of the particle.

The simulation produces a three dimensional acceptance matrix, and returns a correction which can be applied on an event-by-event basis depending on the event's dta, θ, and yta. Use of this simulation has been successfully implemented in CE experiments [90, 91]. Using this method extended the useable scattering angle from 3.9° c.o.m. to 4° c.o.m.

- $\mathcal{L}$: The live time for each experimental run was determined from the readout of the data acquisition system. The average live time for the experiment was recorded to be 95%.

- $d\Omega$: The opening angle is obtained for each angular bin as

$$d\Omega = 2\pi \int_{\theta_i}^{\theta_f} \mathrm{Sin}\theta d\theta \tag{6.41}$$

where θ_i and θ_f are the upper and lower c.o.m. angular bin limits.

Figure 6.19 shows the angular distribution for the peak region in the $^{28}\mathrm{Si}(^{10}\mathrm{Be},^{10}\mathrm{B}+\gamma(1.022$ MeV$))^{28}\mathrm{Al}$ data and for the ground state peak in the $^{12}\mathrm{C}(^{10}\mathrm{Be},^{10}\mathrm{B}+\gamma(0.718$ MeV$))^{12}\mathrm{B}$ data. The data was converted to differential cross-sections as described above. Figure 6.20 shows the excitation energy differential cross-section spectra for each angular bin. Since N_m in Equation 6.40 is for coincidence data with background subtraction, Figures 6.19(a) and 6.20 show cross-sections for $\Delta T = 1, \Delta S = 0$ reactions. In principle, any angular momentum (ΔL) transfer can occur in this data set. The following chapter includes details of the method of separation. Figure 6.19(b) shows the $\Delta T = 1$, $\Delta S = 1$ data for the ground state peak in $^{12}\mathrm{B}$. Both data sets will be decomposed by multipole contributions in Chaper 7.

Chapter 7

Results

The previous chapter detailed how the experimental data was processed into angular distributions, representing $\Delta S = 0$, $\Delta T = 1$ reactions. Within this data, there are contributions that are not monopole ($\Delta L = 0$), and obscure the IVGMR.

In this chapter, the IVGMR in ^{28}Al is isolated in the spectra for comparison with theoretical calculations and determination of strength exhaustion. The first step is to determine the multipole (ΔL) contributions to the spectra with a Multipole Decomposition Analysis (MDA) using the theoretical differential cross-sections described in Chapter 4. The results are then obtained for the IVGMR with the $\Delta L = 0$ contribution. Also obtained in this study are angular distributions for the IVGDR with the $\Delta L = 1$ contribution, which has been measured experimentally for ^{28}Al. Finally, theoretical calculations of the NEWSR are compared to the data, as well as calculations of the strength distribution from the RTBA (see Chapter 3).

7.1   Multipole Decomposition Analysis

The MDA is implemented to disentangle the various multipole contributions to the observed angular distributions and double differential cross-sections, illustrated in Figures 6.19 and 6.20 for data taken on the ^{28}Si and ^{12}C targets. Figure 6.20 is an example of the sensitivity of the angular distributions to angular momentum transfer. A strong peak in the $\theta = 0.25°$

plot of the double differential cross section near 10 MeV diminishes relative to the remaining spectrum as the scattering angle increases. This is a good display of monopole ($\Delta L = 0$) behavior, since the angular distribution for the monopole peaks at $0°$ in scattering angle.

To perform the MDA, each energy bin of Figure 6.20 is plotted as an angular distribution and fit with a linear combination of theoretical (DWBA) cross-sections as

$$\left[\frac{d\sigma}{d\Omega}\right]_{total}^{DWBA} = a\left[\frac{d\sigma}{d\Omega}\right]_{\Delta L=0} + b\left[\frac{d\sigma}{d\Omega}\right]_{\Delta L=1} + c\left[\frac{d\sigma}{d\Omega}\right]_{\Delta L=2} + \cdots \qquad (7.1)$$

where fitting parameters a, b, c, and so on were allowed to vary freely until the total DWBA cross-section converged to a "best fit" for the data. "Best fit" was defined by the lowest reduced χ^2 value (χ^2/N, where N is the number of angular bins less the number of components included in the fit). The structural input to the theoretical angular distributions for the ^{28}Si$\rightarrow^{28}$ IVGMR came from the normal-modes calculation as described in Section 4.3.2.2.

As Table 4.1 shows, for a given angular momentum transfer with no spin-transfer, there exists only one total angular momentum transfer in the target, simplifying the choice of angular distributions for the MDA. If spin-transfer were were present, the choice of spin-dipole ($\Delta L = 1$, $\Delta S = 1$), for example, would be more complex due to the selection rules governing angular momentum coupling, and would introduce more systematic uncertainty.

Before performing the MDA, the theoretical angular distributions need to take into account the experimental angular resolution and the difference in bin size between the data and calculation. The experimental angular resolution needs to be taken into account because the angular bin size was comparable to the resolution. The procedure for incorporating the experimental angular resolution into the DWBA cross-section was to :

$E_X(^{28}Al)=10.0$ MeV
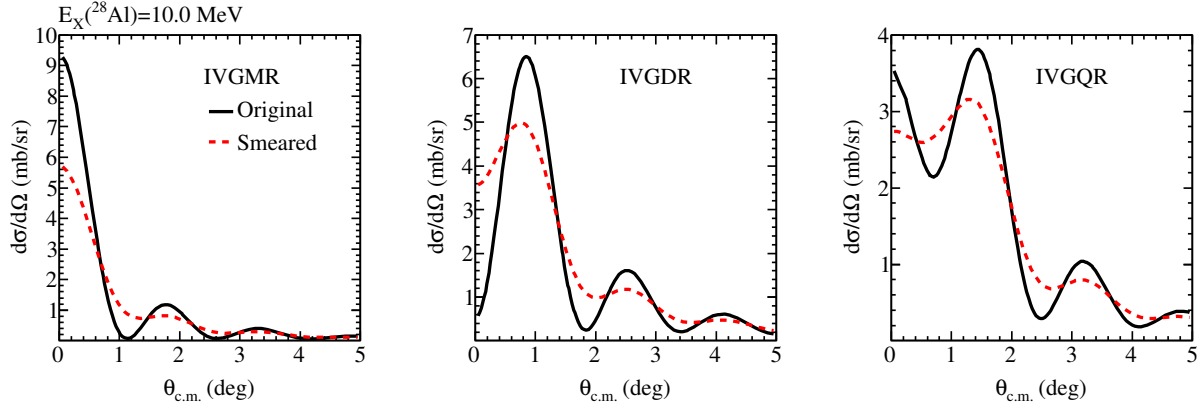
Figure 7.1 Effect of smearing the theoretically calculated angular distributions for the IVGMR, IVGDR, and IVGQR in the ^{28}Si(^{10}Be,^{10}B(IAS))^{28}Al reaction at 10.0 MeV. Angular distributions shown are used in the MDA of the peak region of the ^{28}Al double differential cross section spectrum.

1. Calculate the DWBA angular distributions in steps of 0.5 MeV across the observed excitation energy range for $\Delta L = 0,1,2,3$. Angular distributions were calculated in $0.1°$ increments for $0.0 < \theta_{c.o.m.} < 8.0$.

2. The calculated angular distributions were read into a program to generate the angular distribution in the laboratory frame.

3. The laboratory frame angular distributions were smeared with the experimental resolution.

4. The smeared angular distributions were converted back to the laboratory frame.

Figures 7.1 and 7.2 shows the original angular distributions, as well as the angular distributions after smearing with the experimental resolution for the ^{28}Si(^{10}Be,^{10}B+γ(1.022 MeV))^{28}Al ($\Delta S = 0$, $\Delta T = 1$) reaction at 10 MeV and ^{12}C(^{10}Be,^{10}B+γ(0.718 MeV))^{12}B ($\Delta S = 0$, $\Delta T = 1$) reactions at 0 MeV, respectively. The smearing of the angular distributions washes out the sharp maxima and minima of the angular distributions.
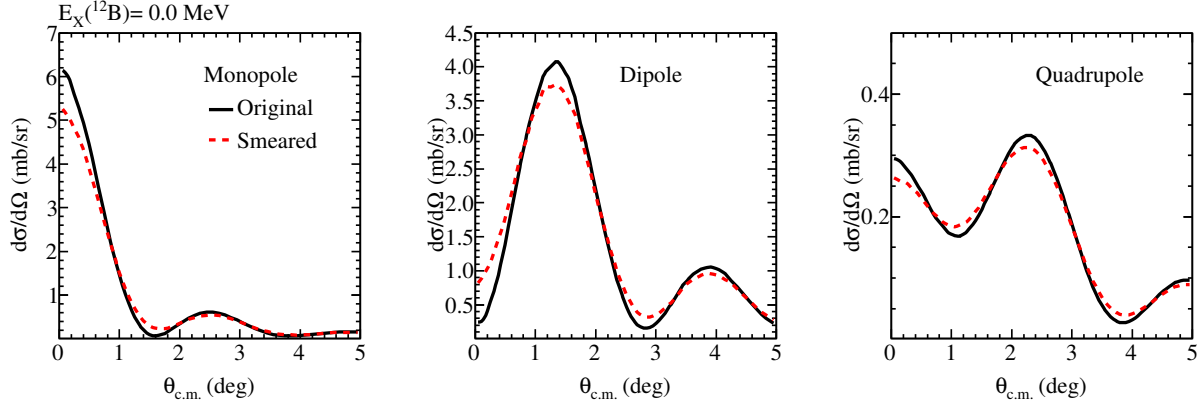
Figure 7.2 Effect of smearing the theoretically calculated angular distributions for the monopole, dipole, and quadrupole contributions to the ^{12}C(0^+, g.s.)(^{10}Be(0^+,g.s.),^{10}B(1^+,0.718 MeV))^{12}B(1^+,g.s.) reaction. Angular distributions shown are used in the MDA of the ground state peak in ^{12}B.

7.1.1 ^{12}C(0^+,g.s.)(^{10}Be,^{10}B+γ(0.718 MeV))^{12}B(1^+,g.s.) MDA Results

	^{12}C
$\Delta L = 0$	0.615±0.053
$\Delta L = 1$	0.266±0.025
$\Delta L = 2$	2.102±0.211

Table 7.1 Scaling factors obtained from the MDA fit of the ^{12}C(0^+,g.s.)(^{10}Be,^{10}B+γ(0.718 MeV))^{12}B(1^+,g.s.) reaction as shown in Figure 7.3. Scaling factors represent the scaling of the theoretically calculated angular distribution necessary for the sum to represent the data as shown in Equation 7.1.

The results of the MDA on the ground state peak in the ^{12}B data are shown in Figure 7.3. The data was fit with $\Delta L = 0, 1$ and 2 components. The ^{12}C(0^+,g.s.)$\rightarrow$^{12}B(1^+,g.s.) transition is GT by definition, so the angular distribution peaks at $0°$ and has strong $\Delta L = 0$ contributions in the MDA. $\Delta L = 2$ contributions can couple to this transition, resulting in the relatively strong contribution found in the MDA, but also serves to fill out the higher angles. The $\Delta L = 1$ component from the fit likely comes from contamination from transitions to the ^{12}B(2^-,1.67 MeV) state, since the MDA of the ^{12}B(1^+,g.s.) peak was performed on
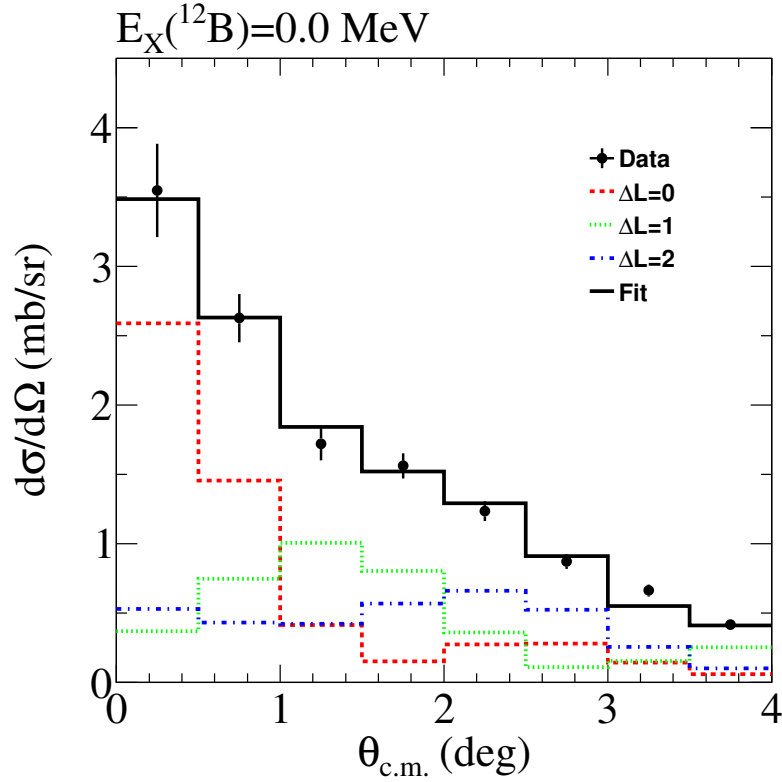
Figure 7.3 MDA of the GT ground state peak of ^{12}B in the ^{12}C(^{10}Be,^{10}B+γ)^{12}B reaction. The measured angular distribution was fit with a linear combination of $\Delta L = 0, 1$, and 2 theoretical angular distributions.

the range $-2 < E_X(^{12}B) \leq 2$ MeV. For this MDA fit, $\chi^2/N = 2.5$. The results of the fit are shown in the fourth column of Table 7.1, where the parameters for $\Delta L = 0, 1$ and 2 represent a, b, and c from Equation 7.1, respectively.

One goal of the analysis of the ^{28}Si(^{10}Be,^{10}B+γ(1.022 MeV))^{28}Al data is to determine the total exhaustion of the NEWSR (see Chapter 3) observed in this experiment. To do this, the cross-section for the reaction is calculated in the DWBA formalism, where the cross-

	B(GT) (Exp.)	B(GT) (Shell Model)
^{10}Be(0^+,g.s.)$\rightarrow$^{10}B(1^+_1,0.718 MeV)	3.51	4.454
^{12}C(0^+,g.s.)$\rightarrow$^{12}B(1^+,g.s.)	0.99	0.995

Table 7.2 Known and calculated GT strength for the ^{10}Be(0^+,g.s.)$\rightarrow$^{10}B(1^+, 0.718 MeV) transition.

section represents the complete exhaustion of the NEWSR at each energy calculated. As discussed in Chapter 4, the DWBA calculation overestimates the reaction cross-section due to its treatment of exchange. Additional effects on the calculation come from the choice of OMP. To account for these effects, the known GT strength for both the probe and target systems are taken into account, and are listed in in Table 7.2. The scaling to take this into account is

$$S' = S \times \left(\frac{B(GT)(SM)}{B(GT)(Experiment)} \right)_{10_{Be} \to 10_B} \times \left(\frac{B(GT)(SM)}{B(GT)(Experiment)} \right)_{12_C \to 12_B}$$
$$= 0.615 \times \left(\frac{4.454}{3.51} \right) \times \left(\frac{0.995}{0.99} \right) = 0.784 \tag{7.2}$$

where SM stands for Shell Model. This scaling factor represents the scaling required to, in first-order, take into account effect due to exchange and OMP choice for $\Delta L = 0$ cross-sections calculated in the DWBA.

7.1.2 ^{28}Si(^{10}Be,^{10}B+γ(1.022 MeV))^{28}Al MDA Results

Figure 7.4 shows the result of performing the MDA on the peak region of the ^{28}Si(^{10}Be,^{10}B+γ(1.022 MeV))^{28}Al data (see Figure 6.19). In the left panel, the result of including $\Delta L = 0, 1$, and 2 components are shown. At zero degrees, the $\Delta L = 0$ component is strongest, and serves to represent the data at the lowest angular bin. The $\Delta L = 1$ component best describes the following two angular bins, with $\Delta L = 2$ and the lower multipole components becoming similar in shape at higher angles, to fill out the remaining region. The right panel of Figure 7.4 shows the sensitivity of the decomposition to the $\Delta L = 0$ component. Exclusion of the $\Delta L = 0$ component from the MDA raises the reduced χ^2 from
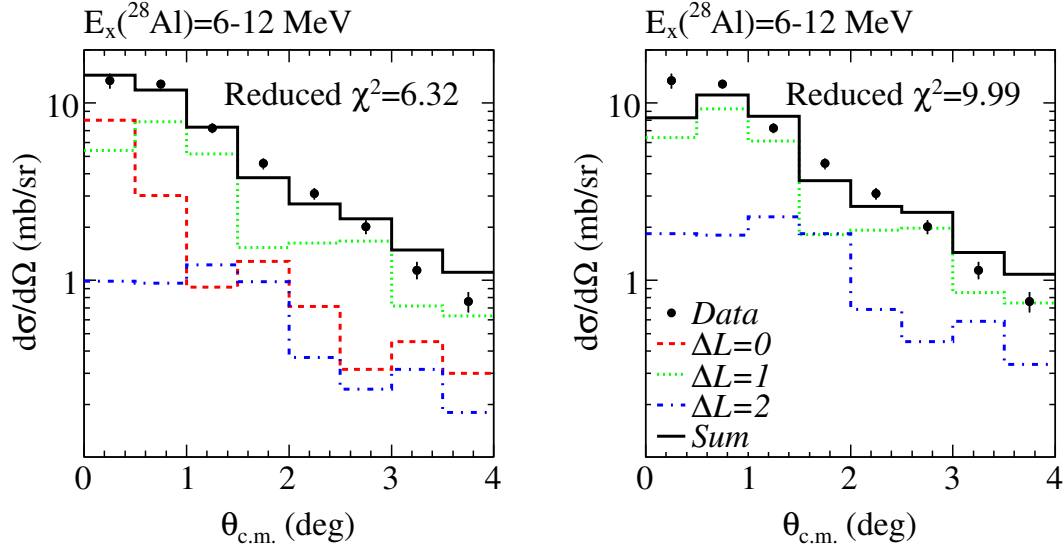
Figure 7.4 MDA of the peak region $6 < E_X(^{28}Al) \leq 12$ MeV in the ^{28}Si(^{10}Be, ^{10}B+γ)^{28}Al reaction. (left) MDA result including the $\Delta L = 0, 1$ and 2 multipoles. (right) MDA fit excluding the $\Delta L = 0$ monopole, and only fitting with $\Delta L = 1$ and $\Delta L = 2$, to observe the sensitivity of MDA to the monopole.

$\chi^2/N = 6.3$ to $\chi^2/N = 10.0$. Exclusion of the $\Delta L = 0$ component raises the $\Delta L = 2$ component's scaling by a factor of 2 and slightly increases the $\Delta L = 1$ component, while failing to reproduce the shape at low angles. The result of the MDA for this fit of the peak region is displayed in the third column of Table 7.1. Higher order multipoles were not included since the angular smearing and wide angular bins washed out the dominant features of the distribution. In the full analysis of the ^{28}Si(^{10}Be,^{10}B+γ(1.022 MeV))^{28}Al data, each 2 MeV energy bin is fit as in the left panel of Figure 7.4. The results of the full MDA are shown in Figure 7.5.

The results of the RTBA calculation as described in Chapter 3 indicate that below about 30 MeV almost all of the contributions to the IVGMR come from the single particle transition $0d_{5/2} \rightarrow 1d_{5/2}$. Illustrated in Figure 7.6, the calculated angular distributions, before smearing, for the IVGMR are almost identical in shape. As a result, a MDA of the data using individual single particle contributions to the IVGMR does not change the extracted distribution.

118
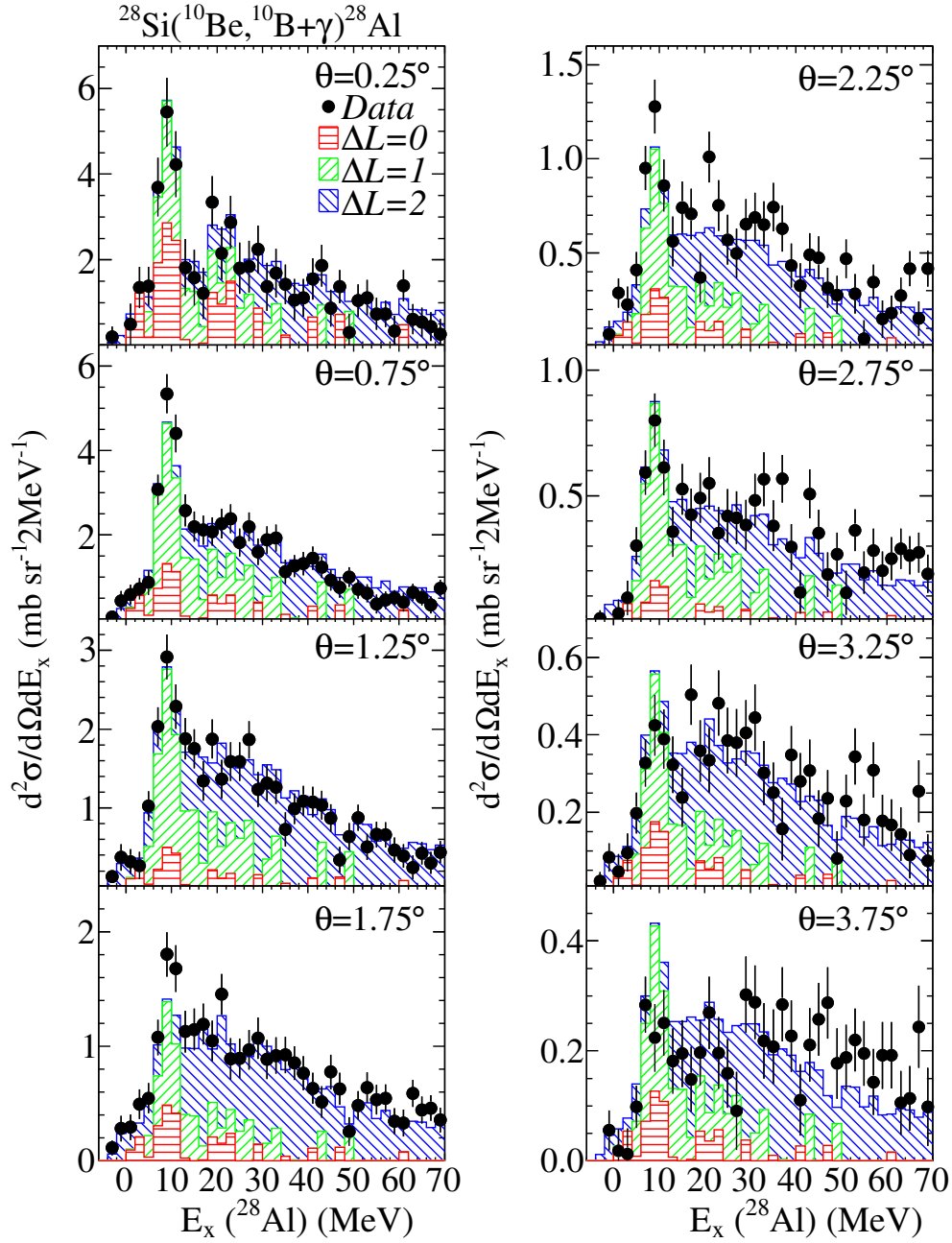
Figure 7.5 Result of the MDA presented as the double differential cross-section of the ^{28}Si(^{10}Be,^{10}B+γ)^{28}Al reaction for each scattering angle bin of the angular distribution. Each 2 MeV energy bin's associated angular distribution was fit in the MDA with $\Delta L = 0, 1,$ and 2 theoretical angular distributions.
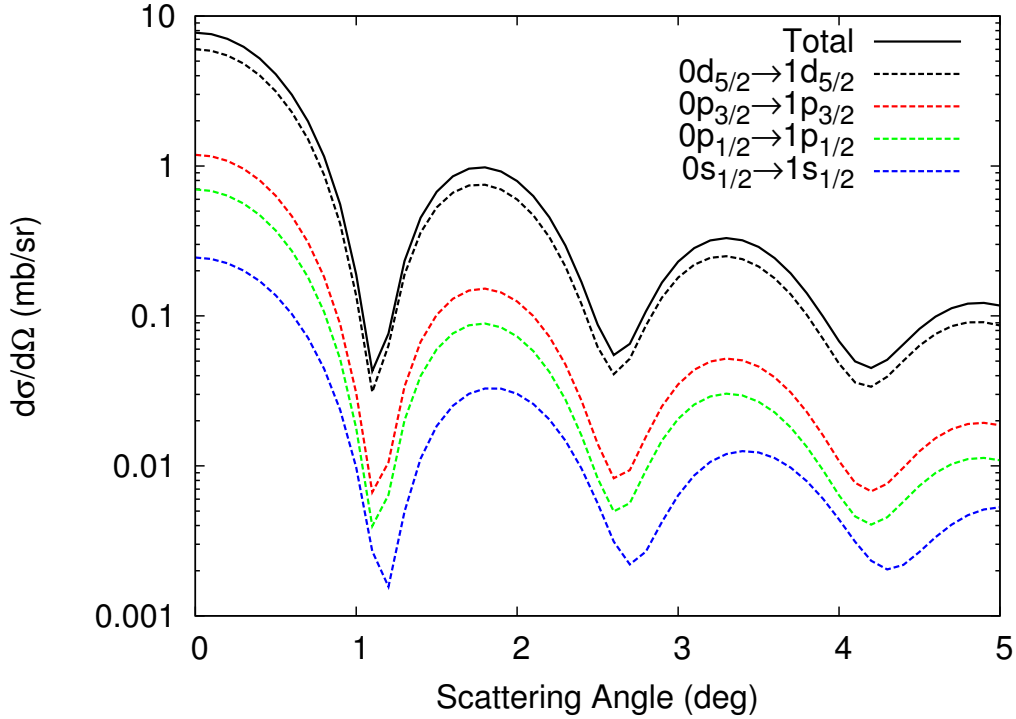
Figure 7.6 Calculated angular distributions for the IVGMR. The curve labeled total includes all single particle transitions in the excitation. Each dashed line represents only the indicated single particle transition for the IVGMR.

7.2   Extracted differential cross-sections in ^{28}Al

With the MDA complete, individual components of the spectra can be analyzed. In principle, multipole contributions greater than $\Delta L = 2$ can contribute to the spectrum, so contributions from these higher multipoles were effectively absorbed into contributions from $\Delta L = 2$ when performing the MDA. As such, commentary can only be made on the $\Delta L = 0$ and $\Delta L = 1$ results of the MDA.

Figure 7.7 shows the extracted $\Delta L = 0$ and $\Delta L = 1$ distributions for the ^{28}Si(^{10}Be,^{10}B+γ)^{28}Al reaction. The double-differential cross-sections are plotted in the angular bin in which they peak. For $\Delta L = 0$, the angular distribution peaks at $0°$, so the $0.25°$ angular bin is displayed. For $\Delta L = 1$, the angular distribution peaks near $0.8°$,
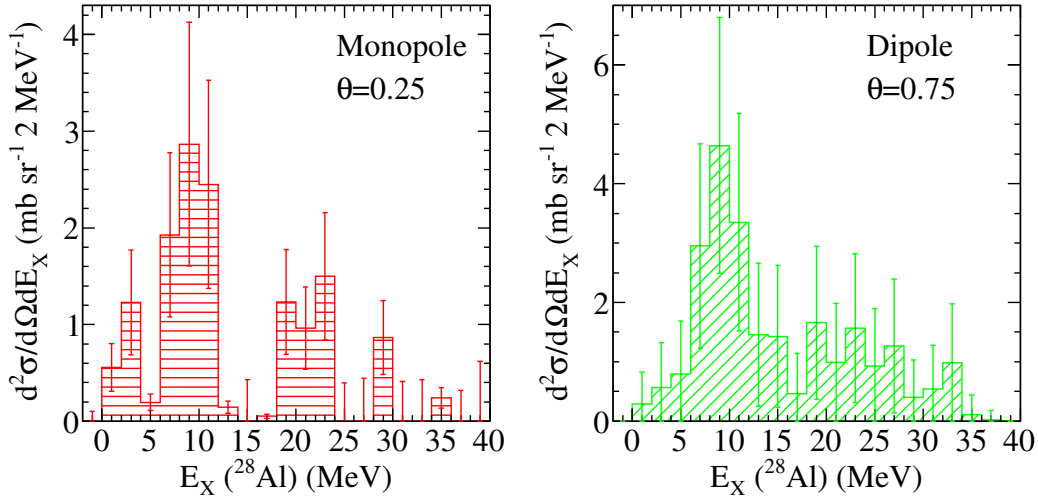
Figure 7.7 Extracted $\Delta L = 0$ (monopole) and $\Delta L = 1$ (dipole) double differential cross-sections for the ^{28}Si(^{10}Be,^{10}B$+\gamma$)^{28}Al reaction. Distributions are shown for the experimental angular bin in which the angular distribution peaks.

	E_X (^{28}Al) (MeV)
Current Work	9.3
^{28}Si(γ,n) [4]	~11
^{28}Si(n,p) [92]	~10
^{28}Si(^{7}Li,^{7}Be) [93]	~11
^{28}Si(γ,abs) [41]	8.2−12.2

Table 7.3 Comparison of the observed peak position of the extracted $\Delta L = 1$ (dipole) distribution for the ^{28}Si(^{10}Be,^{10}B$+\gamma$)^{28}Al reaction with the peak position of the IVGDR measured in previous experiments through the ^{28}Si(γ,n) [4], ^{28}Si(n,p) [92], ^{28}Si(^{7}Li,^{7}Be) [93], and ^{28}Si(γ, abs) [41] reactions. Where necessary, energies relative to the ground state of ^{28}Si were converted to the ground state of ^{28}Al.

depending on E_X(^{28}Al), so the 0.75° angular bin is displayed.

The $\Delta L = 0$ monopole distribution in the left panel of Figure 7.7 is assigned to the IVGMR, since there is no IAS ($0\hbar\omega$,$\Delta L = 0$,$\Delta S = 0$,$\Delta T = 1$) transition in the ^{28}Si$\rightarrow^{28}$Al system as a result of ^{28}Si being a light, stable nucleus in its $J^{\pi} = 0^{+}$ ground state.

The right panel of Figure 7.7 displays the result for the $\Delta L = 1$ dipole distribution. It is dominated by a single peak near 9 MeV, with cross-section diminishing with increased excitation energy. The distribution can be associated with the IVGDR, which has been
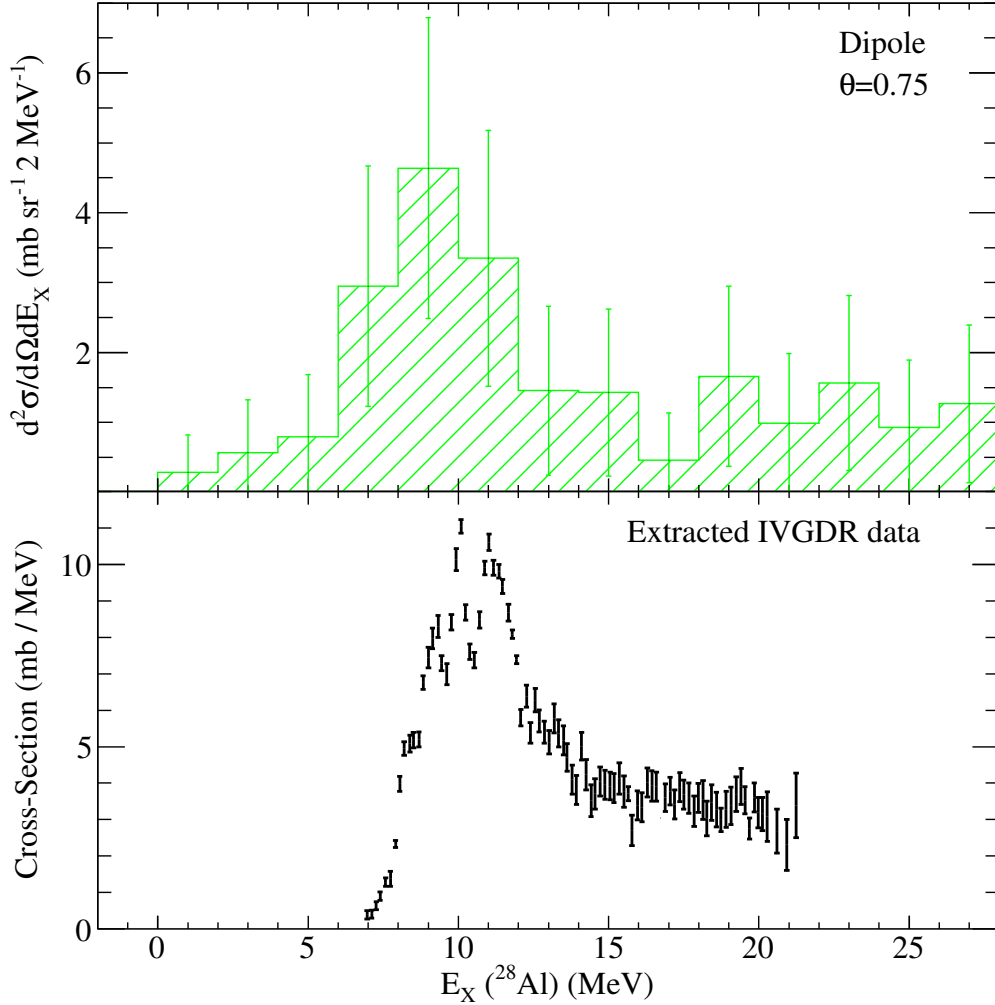
Figure 7.8 Comparison of the measured $\Delta L = 1$ (dipole) distribution for the $^{28}\text{Si}(^{10}\text{Be},^{10}\text{B}+\gamma)^{28}\text{Al}$ reaction with the IVGDR distribution measured previously in the $^{28}\text{Si}(\gamma,\text{n})$ reaction [4].

measured in ^{28}Si and ^{28}Al. Table 7.3 lists the peak energy measured in this experiment, and the observed energy of the peak for References [4], [92], [93] and [41], where Reference [41] measured the fine structure of the peak, so the range is the region of observation. The position of the peak in this experiment agrees with previously measured positions. Figure 7.8 shows the distribution measured in this experiment in the top panel, and the distribution first measured in Reference [4] for the $^{28}\text{Si}(\gamma,n)$ reaction. Including location, the shape of the extracted IVGDR is consistent with previous observations.

Single Particle Transition	$\frac{d\sigma}{d\Omega}(q=0, \theta_{com}=0°)$ (mb/sr)	IVGMR Strength (fm^4)	Ratio
0d$_{5/2}$→1d$_{5/2}$	9.33	15.4	0.61
0p$_{3/2}$→1p$_{3/2}$	1.80	7.34	0.25
0p$_{1/2}$→1p$_{1/2}$	1.06	3.67	0.29
0s$_{1/2}$→1s$_{1/2}$	0.34	2.20	0.16
Total	11.36	28.62	0.41

Table 7.4 Theoretical DWBA cross-section calculation for $q=0$ (no momentum transfer) and 0° scattering angle for each individual state participating in the IVGMR in ^{28}Si. The normal-modes strength obtained when calculating the OBTD for the DWBA cross-section is also shown. The ratio of the cross-section to the strength shows that an assumption of linearity between strength and cross-section does not hold between states.

7.2.1   Comparison with theoretical calculations

As described in Chapters 3 and 4, there are many theoretical techniques available to interpret the data, though a complete model has not been derived. In this section, RTBA calculations, as described in Chapter 3, will be compared with the measured IVGMR and IVGDR because the RTBA is able to fragment strength to more realistic distributions. Also, the data for the IVGMR will be compared against DWBA cross-sections with OBTD's calculated in the normal-modes formalism to determine the percent of the NEWSR observed (see Chapter 4).

Figure 7.9 compares the extracted $\Delta L = 0$ and $\Delta L = 1$ distributions with RTBA calculations for the IVGMR and IVGDR, respectively. The RTBA calculations determine transition strength for a point of energy, so the strengths were smeared with Lorentzians of 2 MeV in width for comparison.

In the case of Figure 7.9(a), the RTBA strengths have been converted to cross-section by assuming a direct relation between strength and cross-section at 0° scattering angle, similar to studies of GT strength distributions ([29], and references therein). Though there is reason to assume this proportionality, 7.4 shows that a constant of proportionality does not hold across states since each particle-hole contribution exhibits a different ratio of cross-

	Strength	
Transition	NORMOD	RTBA
IVGMR	28.62 fm^4	31.36 fm^4
IVGDR	15.22 fm^2	14.67 fm^2

Table 7.5 Total predicted strength for the IVGMR and IVGDR as calculated in the normal-modes and RTBA frameworks.

section to strength. Due to the surface nature of the reaction, and the fragmentation of the strength to high excitation energy, as shown in the RTBA calculation, the $0d_{5/2} \rightarrow 1d_{5/2}$ contribution is selected for conversion of the strength to cross-section. In Figure 7.9(b), the RTBA calculation is presented as its strength.

In Figure 7.9(a), the measured $\Delta L = 0$ distribution is reproduced by the RTBA calculation, but with a shift up in energy of a few MeV. In the RTBA calculation of the IVGMR, there appears to be 2 major peaks, located at $\sim$9 MeV and $\sim$19 MeV, and it is possible to determine the particle-hole composition of the strength. For the lower energy peak, the primary contributor is the $0d_{5/2} \rightarrow 1d_{5/2}$ transition at 59% of the peak strength. Similarly for the second peak, the $0d_{5/2} \rightarrow 1d_{5/2}$ transition participates at 53%. This suggests that the lower energy region of the $\Delta L = 0$ spectrum is primarily composed of $0d_{5/2} \rightarrow 1d_{5/2}$ transitions, where the $p_{3/2}$, $p_{1/2}$, and $2_{1/2}$ contributions begin to participate at higher excitation energy. In Figure 7.9(b), the measured $\Delta L = 1$ distribution is reproduced well by the RTBA calculation. Most notably, the relative shape of the distribution matches nicely with the observation.

Table 7.5 shows the total strength of the IVGMR and IVGDR as calculated in the normal-modes formalism using the code `NORMOD` (see Section 4.3.2.2) and the RTBA. Overall, the methods determine similar strengths, with the RTBA slightly higher for the IVGMR and slightly lower for the IVGDR.

Figure 7.10 compares the DWBA calculation (see Chapter 4) for the IVGMR with the $\Delta L = 0$ distribution to determine the percent exhaustion of the NEWSR (see Chapter 3) in the measured data. In Figure 7.10(a), the DWBA curve represents the cross-section if all of the strength were placed at each point along the curve, since in the normal-modes no information of the strength distribution in energy is given. Assuming the $0d_{5/2} \rightarrow 1d_{5/2}$ transition comprises almost all of the observed spectrum, the DWBA curve is calculated with only this single-particle transition.

With the scaling of the DWBA results applied, Figure 7.10(b) compares the cross-section observed in each energy bin with the DWBA calculated cross-section at the bin's center to determine the percent of the NEWSR observed in the bin, since as mentioned above, the DWBA curve represents the cross-section if all of the strength was placed at that energy. The cross-section was scaled by a factor of 0.784 to account for effects from exchange and choice of OMP on the DWBA calculation, as described in Section 7.1.1. Most strength is concentrated in peaks at 9 and 21 MeV, with sums of $66 \pm 36\%$ and $59 \pm 32\%$, respectively. Figure 7.10(c) shows the running total of Figure 7.10(b). The total exhaustion of the NEWSR observed is $177^{+136}_{-100}\%$ at 35 MeV.
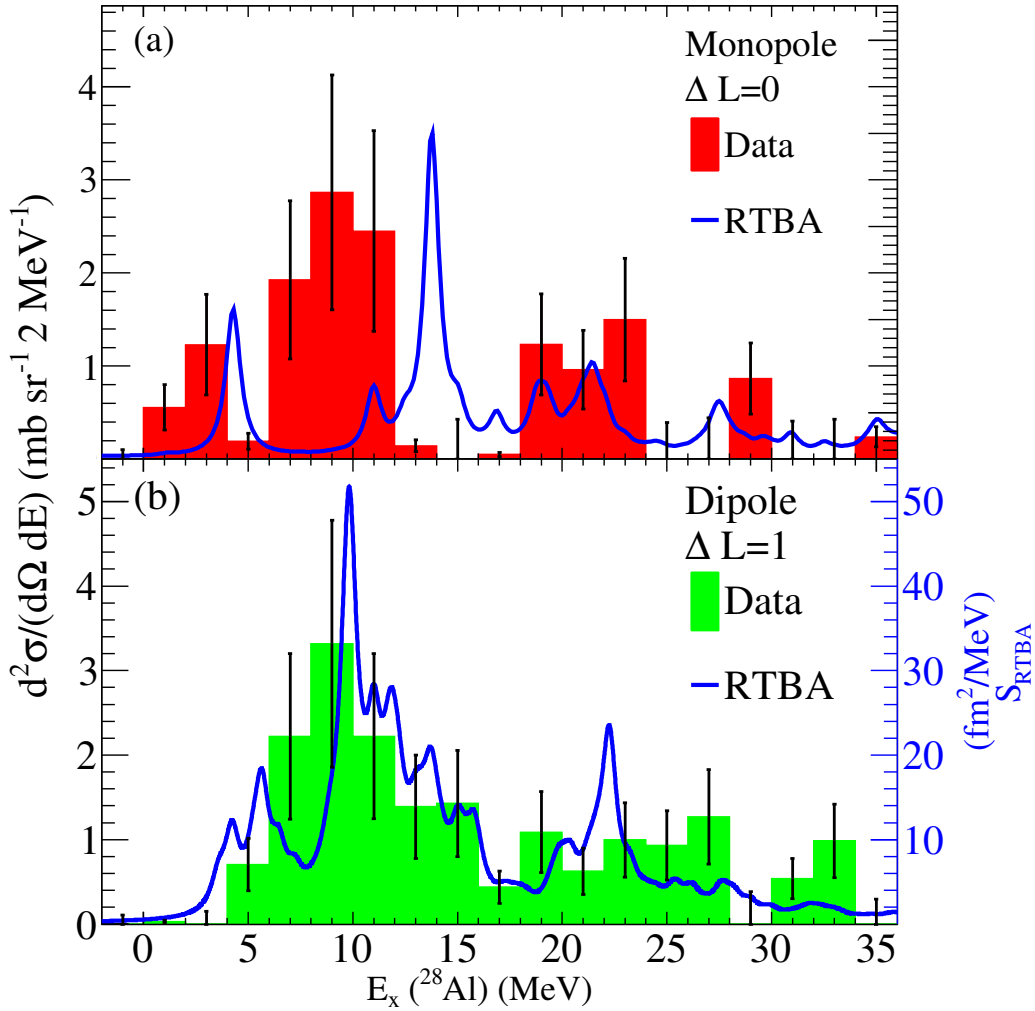
Figure 7.9 Comparison of measured $\Delta L = 0$ (monopole) and $\Delta L = 1$ (dipole) distributions with theoretical calculations from the RTBA. (a) The RTBA strength calculation has been converted into units of mb/sr/MeV. (b) The RTBA strength calculation is presented in units of fm^2/MeV
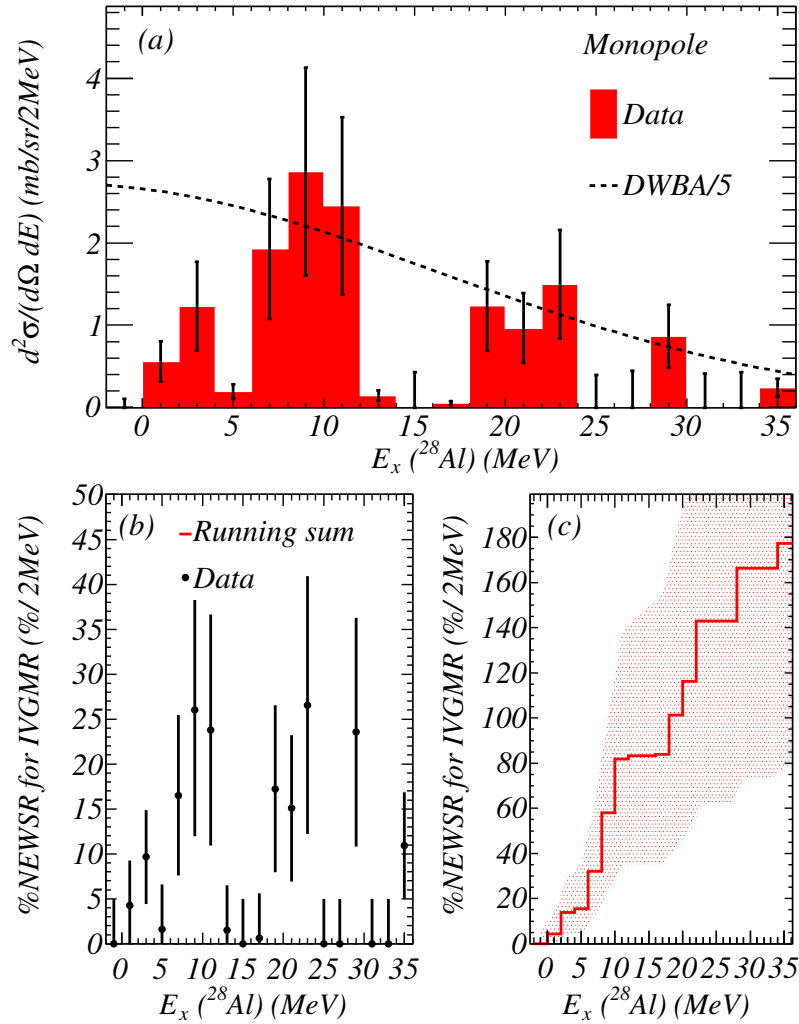
Figure 7.10 (a) Extracted monopole distribution at $\theta_{com} = 0.25°$. The filled histogram represents the data. The dashed line is the calculated DWBA cross-section for the IVGMR as a function of excitation energy. The structural input to the theoretical angular distributions for the ^{28}Si→^{28} IVGMR came from the normal-modes calculation as described in Section 4.3.2.2. (b) Exhaustion of the NEWSR for the IVGMR for each energy bin of the extracted data. (c) Running total of the exhaustion of the NEWSR from (b).

Chapter 8

Conclusion

8.1 Summary

The $(^{10}\text{Be},^{10}\text{B}+\gamma)$ probe is a powerful tool for the isolation of non-spin-flip transitions since these transitions are relatively weakly excited. This is especially important since isolation of the non-spin-flip IVGMR has been difficult for decades due to the lack of a clean non-spin-transfer charge-exchange probe. Complementary to the $(^{10}\text{C},^{10}\text{B}+\gamma)$ probe from Reference [20], the addition of the $(^{10}\text{Be},^{10}\text{B}+\gamma)$ probe to the list of available probes for studying charge-exchange reactions allows for $\Delta S = 0$, $\Delta T = 1$ studies in both the (p,n) and (n,p) directions.

Using the $(^{10}\text{Be},^{10}\text{B}+\gamma)$ charge-exchange probe, the isovector giant monopole resonance (IVGMR) in ^{28}Al was measured. The high-resolution, high-efficiency gamma-ray detector array GRETINA was coupled to the high-resolution spectrometer, the S800, to isolate $\Delta S = 0$, $\Delta T = 1$ events in ^{28}Al. The spectrometer allowed for reconstruction of the excitation energy and scattering angle in ^{28}Al from the $^{28}\text{Si}(^{10}\text{Be},^{10}\text{B}+\gamma)$ reaction. From this, angular distribution of the cross-section across the observed excitation energies were generated. The angular distributions were decomposed into their constituent multipole components using theoretical cross-sections, calculated in the distorted wave Born approximation formalism. The $\Delta L = 0$ and $\Delta L = 1$ cross-section distributions were extracted for $0 < E_X(^{28}Al) \leq 35$ MeV.

The extracted $\Delta L = 1$ (dipole) distribution served to illustrate the successful separation of the multipole components with close agreement to previous measurements of the isovector giant dipole resonance (IVGDR). Also, close agreement with the predicted strength distribution from the relativistic time blocking approximation (RTBA) for the IVGDR was observed.

The extracted $\Delta L = 0$ (monopole) distribution was compared to theoretical calculations. Reasonable agreement with the RTBA calculation for the IVGMR was observed, though the predicted peaks appeared with a small shift in excitation energy relative to the measurement. The measured IVGMR distribution was also compared to the predicted strength calculated in the normal-modes formalism for determination of the percent exhaustion of the non-energy weighted sum-rule (NEWSR). The exhaustion of the NEWSR was observed to be $177^{+136}_{-100}\%$ up to 35 MeV.

8.2 Outlook

The $(^{10}\mathrm{Be},^{10}\mathrm{B}+\gamma)$ probe was shown to be useful in isolating non-spin-transfer charge-exchange reactions. However, as is seen in this experiment in the relatively large uncertainty on the extracted data, higher intensity beams and high-efficiency/high-resolution gamma-ray detection systems are required. The beam intensity for $^{10}\mathrm{Be}$ will be improved when FRIB comes online, and will allow studies of the IVGMR in higher mass nuclei, where the fragmentation of the strength will be less of an issue. Improvements in the gamma-ray tracking in GRETINA will allow for reconstruction of gamma-ray scattering events for even higher efficiency and resolution of the detector system. It may even be possible, given $^{10}\mathrm{Be}$'s long half-life ($t_{1/2} = 1.4 \times 10^6 years$) to produce a $^{10}\mathrm{Be}$ primary beam. This would allow

measurements of higher energy resolution and studies of nuclei of higher mass. In either case, a higher intensity secondary beam or a primary beam of ^{10}Be, the crucial next step is measurement of heavier nuclei. Light nuclei are a good first step, but due to structural effects in light nuclei, strength is fragmented to higher excitation energy.

BIBLIOGRAPHY

BIBLIOGRAPHY

[1] M. N. Harakeh and A. van derWoude. *Giant Resonances: Fundamental High-Frequency Modes of Nuclear Excitation.* Oxford University Press, 2001.

[2] W. Bothe and W. Gentner. Atomumwandlungen durch.-strahlen. *Z. Phys.*, 106:236–248, 1937.

[3] A.B. Migdal. Quadrupole and dipole γ-radiation of nuclei. *J. Phys. USSR*, 8:331, 1944.

[4] B. L. Berman and S. C. Fultz. Measurements of the giant dipole resonance with monoenergetic photons. *Rev. Mod. Phys.*, 47:713–761, Jul 1975.

[5] S. Fukuda and Y. Torizuka. Giant multipole resonances in ^{90}Zr observed by inelastic electron scattering. *Phys. Rev. Lett.*, 29:1109–1111, Oct 1972.

[6] M.B. Lewis and F.E. Bertrand. *Nucl. Phys. A*, 196:337 – 346, 1972.

[7] J. Jänecke and F.D. Becchetti and W.S. Gray and R.S. Tickle and E. Sugarbaker. Coulomb displacement energies and decay widths of isobaric analog states from Sm(^{3}He, t) at $\theta = 0°$. *Nucl. Phys. A*, 402(2):262 – 274, 1983.

[8] D. H. Youngblood, H. L. Clark, and Y-W Lui. Incompressibility of nuclear matter from the giant monopole resonance. *Phys. Rev. Lett.*, 82:691, 1999.

[9] D. H. Youngblood, H. L. Clark, and Y-W Lui. Compressibility of nuclear matter from the giant monopole resonance. *Nucl. Phys. A*, 649:49c, 1999.

[10] A. Erell, J. Alster, J. Lichtenstadt, M. A. Moinester, J. D. Bowman, M. D. Cooper, F. Irom, H. S. Matis, E. Piasetzky, and U. Sennhauser. Measurements on isovector giant resonances in pion charge exchange. *Phys. Rev. C*, 34:1822–1844, Nov 1986.

[11] F. Irom, J.D. Bowman, G.O. Bolme, E. Piasetzsky, U. Sennhauser, J. Alster, J. Lichtenstadt, M. Moinester, J.N. Knudson, S.H. Rokni, and E.R. Siciliano. Excitation of isovector giant resonances in pion single-charge exchange at 120, 165, and 230 mev. *Phys. Rev. C*, 34:2231, 1986.

[12] N. Auerbach and A. Klein. A microscopic theory of giant electric isovector resonances. *Nucl. Phys. A*, 395:77 – 118, 1983.

[13] G. Colò and Nguyen Van Giai. Where is the non-spin-flip isovector monopole resonance in ^{208}?. *Phys. Rev. C*, 53:2201–2206, May 1996.

[14] I. Lhenry. Decay of the isovector giant resonances excited in charge exchange reactions. *Nucl. Phys. A*, 599:245 – 258, 1996. Proceedings of the Groningnen Conference on Giant Resonances.

[15] T. Ichihara, M. Ishihara, H. Ohnuma, T. Niizeki, Y. Satou, H. Okamura, S. Kubono, M. H. Tanaka, and Y. Fuchi. Isovector Quadrupole Resonance Observed in the ^{60}Ni(^{13}C,^{13}N)^{60}Co Reaction at $E/A = 100$ MeV. *Phys. Rev. Lett.*, 89:142501, Sep 2002.

[16] S. Nakayama, H. Akimune, Y. Arimoto, I. Daito, H. Fujimura, Y. Fujita, M. Fujiwara, K. Fushimi, H. Kohri, N. Koori, K. Takahisa, T. Takeuchi, A. Tamii, M. Tanaka, T. Yamagata, Y. Yamamoto, K. Yonehara, and H. Yoshida. Isovector Electric Monopole Resonance in ^{60}Ni. *Phys. Rev. Lett.*, 83:690–693, Jul 1999.

[17] A. Bohr and B.R. Mottelson. *Nuclear Structure* **II**. W.A. Benjamin, Inc., New York, 1969.

[18] H. Lenske, H. H. Wolter, and H. G. Bohlen. Reaction mechanism of heavy-ion charge-exchange scattering at intermediate energies. *Phys. Rev. Lett.*, 62:1457–1460, Mar 1989.

[19] N. Auerbach, F. Osterfeld, and T. Udagawa. The spin isovector monopole strength and the (^{3}He,t) reaction. *Phys. Lett. B*, 219:184 – 188, 1989.

[20] Y. Sasamoto. *Study of the isovector non-spin-flip monopole resonance via the superallowed Fermi type charge exchange (^{10}C,^{10}Bγ) reaction*. dissertation, University of Tokyo, 2012. PhD thesis.

[21] W. G. Love and M. A. Franey. Effective nucleon-nucleon interaction for scattering at intermediate energies. *Phys. Rev. C*, 24:1073–1094, Sep 1981.

[22] T. Suzuki, R. Fujimoto, and T. Otsuka. Cross sections for the excitation of isovector charge-exchange resonances in ^{208}Tl. *Phys. Rev. C*, 67:044302, Apr 2003.

[23] B.K. Fujikawa, S.J. Asztalos, R.M. Clark, M.-A. Deleplanque-Stephens, P. Fallon, S.J. Freedman, J.P. Greene, I.-Y. Lee, L.J. Lising, A.O. Macchiavelli, R.W. MacLeod, J.C.

Reich, M.A. Rowe, S.-Q. Shang, F.S. Stephens, and E.G. Wasserman. A new measurement of the strength of the superallowed Fermi branch in the beta decay of ^{10}C with GAMMASPHERE. *Phys. Lett. B*, 449:6 – 11, 1999.

[24] D. Bazin, J.A. Caggiano, B.M. Sherrill, J. Yurkon, and A. Zeller. The S800 spectrograph. *Nucl. Instr. Meth. B*, 204:629 – 633, 2003. 14th International Conference on Electromagnetic Isotope Separators and Techniques Related to their Applications.

[25] D. Bazin. S800 spectrometer service level description, 2007. NSCL internal document.

[26] Available Beams at the National Superconducting Cyclotron Laboratory. `http://nscl.msu.edu/users/beams.html`.

[27] O.B. Tarasov and D. Bazin. Lise++: Radioactive beam production with in-flight separators. *Nucl. Instr. Meth. B*, 266:4657 – 4664, 2008.

[28] I.Y. Lee. Gretina simulation. `https://groups.nscl.msu.edu/gretina/simulations/index.php`.

[29] G. Perdikakis, R. G. T. Zegers, Sam M. Austin, D. Bazin, C. Caesar, J. M. Deaven, A. Gade, D. Galaviz, G. F. Grinyer, C. J. Guess, C. Herlitzius, G. W. Hitt, M. E. Howard, R. Meharchand, S. Noji, H. Sakai, Y. Shimbara, E. E. Smith, and C. Tur. Gamow-Teller unit cross sections for (t,He^3) and (He^3,t) reactions. *Phys. Rev. C*, 83:054614, May 2011.

[30] A. Bohr and B.R. Mottelson. *Nuclear Structure* **I**. W.A. Benjamin, Inc., New York, 1975.

[31] J. Speth, J. Wambach, A. van der Woude, K.T. Knöpfle, G.J. Wagner, S. Raman, L.W. Fagg, R.S. Hicks, and F. Osterfeld. *Electric and Magnetic Giant Resonances in Nuclei*, volume 7. World Scientific, Singapore, 1991.

[32] D. H. Youngblood, H. L. Clark, and Y-W Lui. Compression mode giant resonances. *RIKEN Rev.*, 23:159, 1999.

[33] J.D. Bowman, E. Lipparini, and S. Stringari. Isovector monopole excitation energies. *Phys. Lett. B*, 197:497 – 499, 1987.

[34] R. Zegers. *Search for Isovector Giant Monopole Resonances.* dissertation, University of Groningen, 1999. PhD thesis.

[35] Franz Osterfeld. Nuclear spin and isospin excitations. *Rev. Mod. Phys.*, 64:491–557, Apr 1992.

[36] K Goeke and J Speth. Theory of giant resonances. *Ann. Rev. Nucl. Part. Sci.*, 32:65–115, 1982.

[37] R.G.T. Zegers. *private communication.*

[38] N. Auerbach. Excitation of giant resonances in pion charge-exchange reactions. *J. de Physique*, 45:305, Mar 1984.

[39] S. Krewald, J. Birkholz, Amand Faessler, and J. Speth. Continuum Random-Phase-Approximation Calculations of Higher Multipole Giant Resonances in ^{16}O and ^{40}Ca. *Phys. Rev. Lett.*, 33:1386–1388, Dec 1974.

[40] A. Van Der Woude. Giant resonances. *Progress in Particle and Nuclear Physics*, 18:217 – 293, 1987.

[41] H. Harada et al. Fine Structure of Giant Resonance in the ^{28}Si(γ,abs) Reaction. *Journal of Nucl. Sci. and Tech.*, 38:465, 2001.

[42] E. Litvinova, B.A. Brown, D.-L. Fang, T. Marketin, and R.G.T. Zegers. Benchmarking nuclear models for gamoow-teller response. *Phys. Lett. B*, 730:307 – 313, 2014.

[43] T. Marketin, E. Litvinova, D. Vretenar, and P. Ring. Fragmentation of spin-dipole strength in ^{90}Zr and ^{208}Pb. *Phys. Lett. B*, 706:477 – 481, 2012.

[44] J. Engel, P. Vogel, and M. R. Zirnbauer. Nuclear structure effects in double-beta decay. *Phys. Rev. C*, 37:731–746, Feb 1988.

[45] J. Suhonen. *From Nucleon to Nucleus*. Springer, Berlin, Heidelberg, New York, 2007. Theoretical Mathematical Physics.

[46] P. Ring and P. Schuck. *The Nuclear Many-Body Problem*. Springer, Berlin, Heidelberg, New York, 1980. Theoretical Mathematical Physics.

[47] S.P. Kamerdshiev, G. Ya. Tertychny, and V.I. Tselyaev. *Phys. Part. Nucl.*, 28:134, 1997.

[48] V. I. Tselyaev. Quasiparticle time blocking approximation within the framework of generalized green function formalism. *Phys. Rev. C*, 75:024306, Feb 2007.

[49] P. Ring, Zhong yu Ma, Nguyen Van Giai, D. Vretenar, A. Wandelt, and Li gang Cao. The time-dependent relativistic mean-field theory and the random phase approximation. *Nucl. Phys. A*, 694:249 – 268, 2001.

[50] G.R. Satchler. *Direct Nuclear Reactions*. Clarendon Press, 1983.

[51] D.F. Jackson. *Nuclear Reactions*. Chapman and Hall, 1975.

[52] J. Cook and J. Carr. Computer program FOLD. Florida State University (unpublished); based on F. Petrovich and D. Stanley, *Nucl. Phys. A* 275:487, 1977; modified as described in J. Cook *et al.*, *Phys. Rev. C* 30:1538, 1984; R.G.T. Zegers (2005), unpublished.

[53] W.D.M. Rae. NuShell. `http://knollhouse.org/default.aspx`.

[54] B.A. Brown and W.D.M. Rae. NuShellX. `http://nscl.msu.edu/~brown/resources/resources.html`.

[55] M.A. Hofstee, S.Y. van der Werf, A.M. van den Berg, N. Blasi, J.A. Bordewijk, W.T.A. Borghols, R. De Leo, G.T. Emery, S. Fortier, S. Galès, M.N. Harakeh, P. den Heijer, C.W. de Janger, H. Langevin-Joliot, S. Micheletti, M. Morlet, M. Pignelli, J.M. Schippers, H. de Vries, A. Willis, and A. van der Woude. Localized $1\hbar\omega$ particle-hole strength in nuclei. *Nucl. Phys. A*, 588:729, 1995.

[56] S.Y. van der Werf. Normod. unpublished.

[57] J. A. Tostevin and B. A. Brown. Diffraction dissociation contributions to two-nucleon knockout reactions and the suppression of shell-model strength. *Phys. Rev. C*, 74:064604, Dec 2006.

[58] J.A. Tostevin. unpublished. Computer codes FRONTHF and SMATPOT.

[59] B. Alex Brown. New skyrme interaction for normal and exotic nuclei. *Phys. Rev. C*, 58:220–231, Jul 1998.

[60] A. Ozawa et al. Measurements of interaction cross sections forlightneutron-rich nuclei at relativistic energies anddetermination of effective matter radii. *Nucl. Phys.*, A691:599 – 617, 2001.

[61] J. A. Tostevin. Core excitation in halo nucleus break-up. *J. Phys. G*, 25:735, 1999.

[62] J. S. Al-Khalili and J. A. Tostevin. Few-body calculations of proton-^{6,8}He scattering. *Phys. Rev. C*, 57:1846–1852, Apr 1998.

[63] L. Ray. Proton-nucleus total cross sections in the intermediate energy range. *Phys. Rev. C*, 20:1857–1872, Nov 1979.

[64] N. Anantaraman et al. (^{12}C,^{12}B) and (^{12}C,^{12}N) reactions at $E/A = 70$ MeV/u as spin probes: Calibration and application to 1^+ states in ^{56}Mn. *Phys. Rev. C*, 44:398–414, Jul 1991.

[65] M. A. Franey and W. G. Love. Nucleon-nucleon t -matrix interaction for scattering at intermediate energies. *Phys. Rev. C*, 31:488–498, Feb 1985.

[66] T. Udagawa, A. Schulte, and F. Osterfeld. Antisymmetric distorted wave impulse approximation calculations for composite particle scattering. *Nuclear Physics A*, 474:131 – 154, 1987.

[67] B.A. Brown, W.D.M. Rae, E. McDonald, and M. Horoi. *NUSHELLX@MSU*. http://www.nscl.msu.edu/~brown/resources/resources.html.

[68] W.D.M. Rae. *NUSHELLX*. http://www.garsington.eclipse.co.uk/.

[69] The k500⊗k1200, a coupled cyclotron facility at the national superconducting cyclotron laboratory, 1994. NSCL Report MSUCL-939.

[70] D.J. Morrissey, B.M. Sherrill, M. Steiner, A. Stolz, and I. Wiedenhoever. Commissioning the A1900 projectile fragment separator. *Nucl. Instr. Meth. B*, 204:90 – 96, 2003. 14th International Conference on Electromagnetic Isotope Separators and Techniques Related to their Applications.

[71] Glenn F. Knoll. *Radiation Detection and Measurement*. John Wiley & Sons, New York, 2000.

[72] J. Yurkon, D. Bazin, W. Benenson, D.J. Morrissey, B.M. Sherrill, D. Swan, and R. Swanson. Focal plane detector for the S800 high-resolution spectrometer. *Nucl. Instr. and Meth. A*, 422:291–295, 1999.

[73] S. Paschalis et al. The performance of the gamma-ray energy tracking in-beam nuclear array gretina. *NIM*, A709:44 – 55, 2013.

[74] K. Meierbachtol. *Parallel and perpendicular momentum distributions in projectile fragmentation reactions.* dissertation, Michigan State University, 2012. PhD thesis.

[75] H. Wollnik. *Optics of Charged Particles.* Academic Press, Inc., Orlando, 1987.

[76] Siegfried A. Martin, Arno Hardt, Jrgen Meissburger, Georg P.A. Berg, Ulrich Hacker, Werner Hrlimann, Josef G.M. Rmer, Thomas Sagefka, Adolf Retz, Otto W.B. Schult, Karl L. Brown, and Klaus Halbach. The *qqddq* magnet spectrometer big karl. *Nucl. Instr. Meth.*, 214:281 – 303, 1983.

[77] H Fujita, Y Fujita, G.P.A Berg, A.D Bacher, C.C Foster, K Hara, K Hatanaka, T Kawabata, T Noro, H Sakaguchi, Y Shimbara, T Shinada, E.J Stephenson, H Ueno, and M Yosoi. Realization of matching conditions for high-resolution spectrometers. *Nucl. Instr. Meth. A*, 484:17 – 26, 2002.

[78] D.L. Hendrie. *in Nuclear Spectroscopy and Reactions part A, p. 365.* Academic Press, New York, 1974.

[79] Y. Fujita, K. Hatanaka, G.P.A. Berg, K. Hosono, N. Matsuoka, S. Morinobu, T. Noro, M. Sato, K. Tamura, and H. Ueno. Matching of a beam line and a spectrometer New beam line project at RCNP. *Nucl. Instr. Meth. B*, 126:274 – 278, 1997.

[80] D. Bazin. *private communication.*

[81] G.W. Hitt. *The $^{64}Zn(t,^3He)$ charge-exchange reaction at 115 MeV per nucleon and application to ^{64}Zn stellar electron-capture.* dissertation, Michigan State University, 2009. PhD thesis.

[82] Kyoko Makino and Martin Berz. Cosy infinity version 8. *Nucl. Instr. Meth. A*, 427:338 – 343, 1999.

[83] S. Sharma. *Atomic and Nuclear Physics.* Pearson Education, India, 2008.

[84] D. Weisshaar, A. Gade, T. Glasmacher, G.F. Grinyer, D. Bazin, P. Adrich, T. Baugher, J.M. Cook, C.Aa. Diget, S. McDaniel, A. Ratkiewicz, K.P. Siwek, and K.A. Walsh. CAESAR: A high-efficiency CsI(Na) scintillator array for in-beam spectroscopy with fast rare-isotope beams. *Nucl. Instr. Meth A*, 624:615 – 623, 2010.

[85] W.F. Mueller, J.A. Church, T. Glasmacher, D. Gutknecht, G. Hackman, P.G. Hansen, Z. Hu, K.L. Miller, and P. Quirin. Thirty-two-fold segmented germanium detectors to

identify γ-rays from intermediate-energy exotic beams. *Nucl. Instr. Meth. A*, 466:492 – 498, 2001.

[86] Newspectcl, 1999. Modified version of NSCL designed SpecTcl, `http://docs.nscl.msu.edu/daq/spectcl/`, additional modifications to include GRETINA data processing, 2012.

[87] K. Wimmner and E. Lunderberg. GROOT Analysis Package for the `S800+GRETINA` Campaign at NSCL, 2012. `http://nucl.phys.s.u-tokyo.ac.jp/wimmer/software.php'`.

[88] LBNL Isotopes Project Nuclear Data Dissemination Home Page. retrieved June 10, 2012, from `http://ie.lbl.gov/toi.html`.

[89] G. W. Hitt, R. G. T. Zegers, Sam M. Austin, D. Bazin, A. Gade, D. Galaviz, C. J. Guess, M. Horoi, M. E. Howard, W. D. M. Rae, Y. Shimbara, E. E. Smith, and C. Tur. Gamow-teller transitions to ^{64}Cu measured with the ^{64}Zn(t,^{3}He) reaction. *Phys. Rev. C*, 80:014313, Jul 2009.

[90] C.J. Guess. *The $^{150}Sm(t,^3He)^{150}Pm*$ and $^{150}Nd(^3He,t)^{150}Pm*$ reactions and applications for 2ν and 0ν double beta decay.* dissertation, Michigan State University, 2010. PhD thesis.

[91] A. Prinke. *Searching for the origins of flourine: A measurement of the $^{19}F(t,^3He)$ reaction.* dissertation, Michigan State University, 2012. PhD thesis.

[92] J.L. Ullmann et al. Analog giant dipole excitation in Si(n, p) at 59.6 MeV. *Nucl. Phys.*, A386:179 – 188, 1982.

[93] S. Nakayama et al. Isovector giant resonances in light nuclei observed by (^{7}Li, ^{7}Be) reaction. *Phys. Lett. B*, 195:316 – 320, 1987.